Interventional nuclear imaging for radioembolisation guidance

Sandra van der Velden

Colophon

Interventional nuclear imaging for radieombolisation guidance
PhD thesis, Utrecht University - with a summary in Dutch

velden.sandra@gmail.com

ISBN: 978-90-393-7096-4
Cover design: Sandra van der Velden
Lay-out: Sandra van der Velden
Printing: Ridderprint

Interventional nuclear imaging for radioembolisation guidance

Interventionele nucleaire beeldvorming voor geleiding van radioembolisatie

(met een samenvatting in het Nederlands)

Proefschrift

ter verkrijging van de graad van doctor aan de Universiteit Utrecht op gezag van de rector magnificus, prof.dr. H.R.B.M. Kummeling, ingevolge het besluit van het college voor promoties in het openbaar te verdedigen op donderdag 21 maart 2019 des middags te 4.15 uur

door

Sandra van der Velden

geboren op 11 juni 1989
te Nuenen, Gerwen en Nederwetten

Promotoren: Prof. dr. ir. H.W.A.M. de Jong
Prof. dr. ir. M.A. Viergever

Publication of this thesis was financially supported by:
Sirtex Medical Europe
Angiocare
Scionix
ChipSoft
Nuclear Fields

Contents

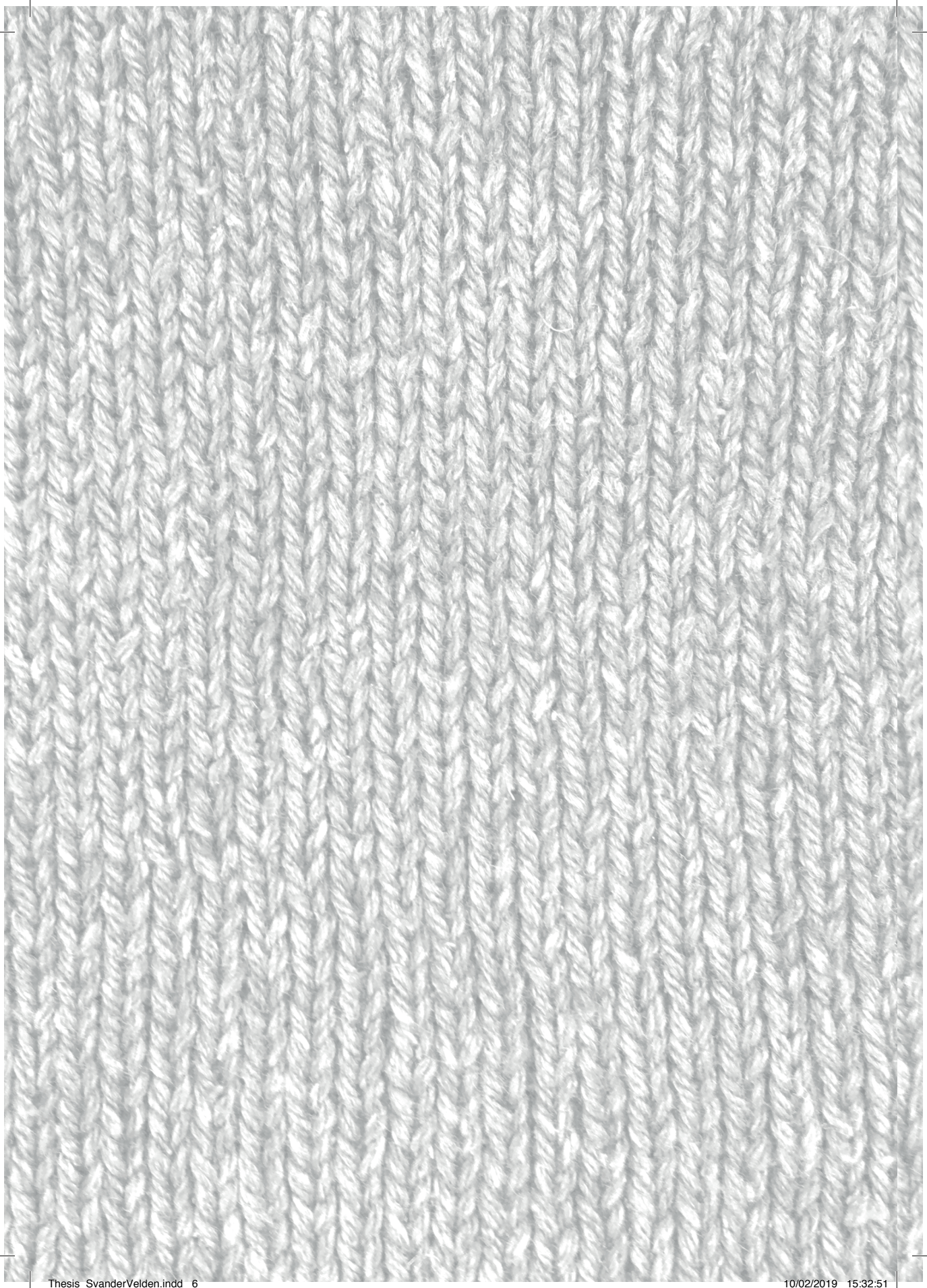

1

Introduction

Radionuclide therapy

Cancer treatment consists commonly of surgery, radiation therapy and/or chemotherapy. Alternatively, internal radiation therapy with radionuclides (radionuclide therapy) can be used. Advantages of this form of therapy include non-invasiveness, compared to surgery, and more direct targeting, compared to radiation therapy and systemically administered chemotherapy. Specific targeting can be achieved by using radiopharmaca that are being internalised by the tumour cells by binding to a cell-specific antigen or peptide, by injecting microspheres with a radionuclide into the arteries or by injecting microspheres with a radionuclide directly into the tumour (1,2). Examples of therapeutic radionuclides are iodine-131 (^{131}I) for treatment of thyroid cancer and lutetium-177 (^{177}Lu) for treatment of prostate cancer.

Radioembolisation

Radioembolisation is a treatment for patients with unresectable tumours in the liver (3–5) and is a specific example of radionuclide therapy. The treatment relies on the dual blood supply of the liver; the normal liver tissue receives most of its blood from the portal vein, whilst the tumours receive most of their blood from the liver artery. In radioembolisation, a catheter is inserted into the liver artery and microspheres loaded with radioactive yttrium-90 (^{90}Y) are released. These microspheres (~3-5 GBq) will mainly lodge in the microvasculature of the tumours, irradiating the tumour locally.

The workflow of a radioembolisation procedure consists of multiple steps (Figure 1). First, a pre-treatment procedure is performed using technetium-99m macroaggregated albumin (^{99m}Tc-MAA). The pre-treatment procedure starts at the intervention room, where the liver vasculature is assessed and the injection position is determined, guided by fluoroscopic images. A small amount of ^{99m}Tc-MAA (~150 MBq) is then injected into the liver artery, mimicking the actual treatment procedure. Subsequently, the distribution of the ^{99m}Tc-MAA particles is assessed at the nuclear medicine department. Treatment may be abandoned or altered (e.g. other injection position or less ^{90}Y activity) if a too large fraction of particles shunts to the lungs and/or when extrahepatic depositions (e.g. in the stomach or duodenum) are present. When treatment is considered safe, the radioactive microspheres are administered to the patient, again under guidance of fluoroscopic images. Finally, the actual distribution can be assessed at the nuclear medicine department. In research settings, additional nuclear imaging can take place a few months after treatment to assess treatment response.

The pre-treatment procedure is commonly performed one to two weeks before the actual treatment (3,6), since microspheres are ordered after the pre-treatment procedure. Also, performing the pre-treatment and treatment procedure in a single session is difficult to implement, due to the need of transporting the patient from the intervention room to the nuclear medicine department for imaging of the ^{99m}Tc-MAA distribution. A single-session procedure would have many advantages over the current clinical practice, including the possibility of using the exact same injection position for the pre-treatment and treatment procedure (7) and shorter overall treatment times (8,9). The majority of this thesis focusses on the development and application of a device which can acquire both fluoroscopic and nuclear images in the intervention room, which could eventually lead to single-session radioembolisation procedures.

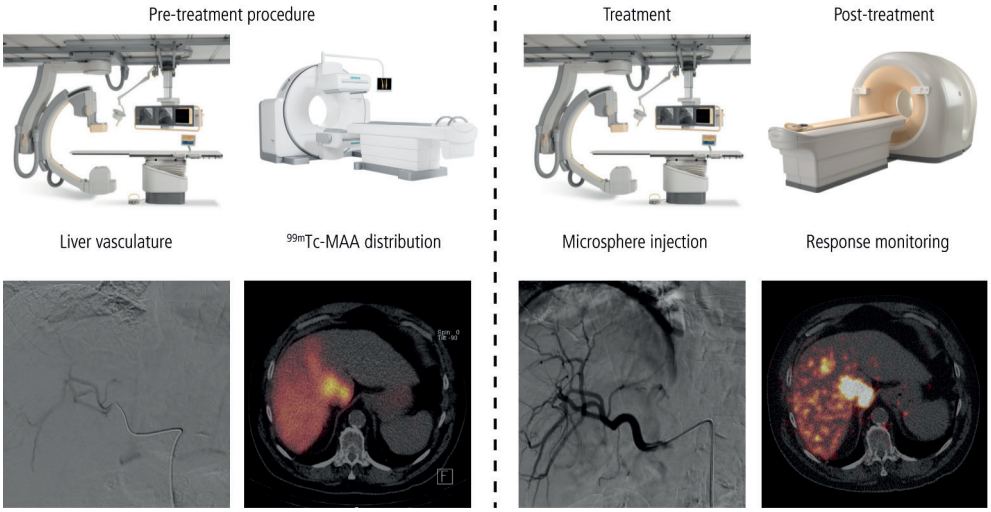

Figure 1: Workflow of a radioembolisation procedure. Top row: imaging modalities used. Bottom row: examples of the images used in planning and evaluating the treatment. The pre-treatment procedure and the treatment procedure are commonly seperated by one to two weeks.

Figure 2: Typical example of a clinical SPECT/CT scanner (courtesy Siemens Healthineers).

Medical Imaging

Imaging plays an important role in radioembolisation therapy for planning, dosimetry and response monitoring. The most important imaging modalities used in radioembolisation are discussed below.

Single photon computed tomography

Single photon emission computed tomography (SPECT) is the principal imaging modality in the nuclear medicine department and is used for a large number of applications. A SPECT system relies on photon detection in a gamma camera for the creation of projections, which are subsequently reconstructed into a three-dimensional activity distribution. An image of a typical SPECT system is shown in Figure 2.

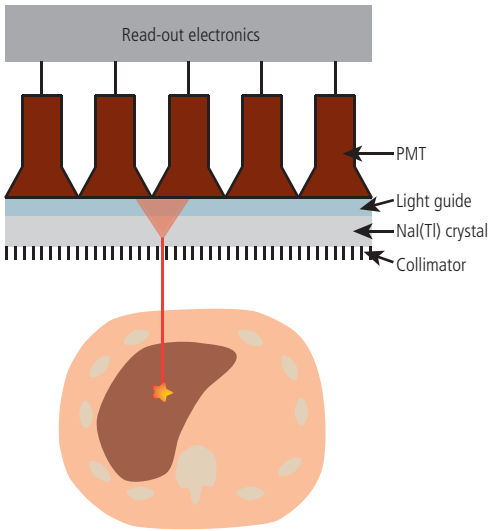

Figure 3: Schematic overview of a gamma camera and the photon detection process.

Photon detection

A SPECT scanner uses a gamma camera for photon detection. A gamma camera consists of a NaI(Tl) scintillation crystal, a light guide, photomultiplier tubes (PMTs) and read-out electronics. Figure 3 shows a schematic overview of a gamma camera and the photon detection process. When a gamma photon enters the gamma camera, its energy is absorbed in the scintillation crystal, creating a cascade of scintillation photons. The scintillation photons get dispersed in the crystal and the light guide, after which they are absorbed by a phosphorescent layer on the PMTs. This induces the creation of photoelectrons, which are amplified into a measurable electronic signal by the PMTs. Owing to the dispersion of the scintillation photons, multiple PMTs will give a signal after absorption of one gamma photon. The total electronic signal is proportional to the energy of the absorbed gamma photon. The signal distribution across the PMTs is used to determine the position of the incoming gamma photon.

Collimation

Just like a photo camera needs a lens, a gamma camera needs some form of collimation to obtain useful images. However, high energy gamma photons cannot be bent with lenses like visible light photons. Therefore, the principle of absorption collimation is applied in the generation of projections. Collimators are designed such that only gamma photons travelling in specific directions are accepted to reach the scintillation crystal. Typically, collimators are made of high stopping power material, e.g. lead or tungsten, to increase the chance of full photoelectric absorption of photons not travelling in the preferred direction.

Collimators can be divided into four different types: parallel hole collimators, converging collimators, diverging collimators and pinhole collimators (Figure 4) (10). Parallel hole collimators are most frequently used in clinical practice and consist of parallel, hexagonal "holes", separated by thin septa of lead. Only gamma photons travelling in directions parallel to the septa will pass through the collimator and will be detected by the gamma camera. The resolution and sensitivity of the collimator are a function of the hole width, hole length and septal thickness. In general, sensitivity can be increased at the cost of reducing the resolution of the collimator.

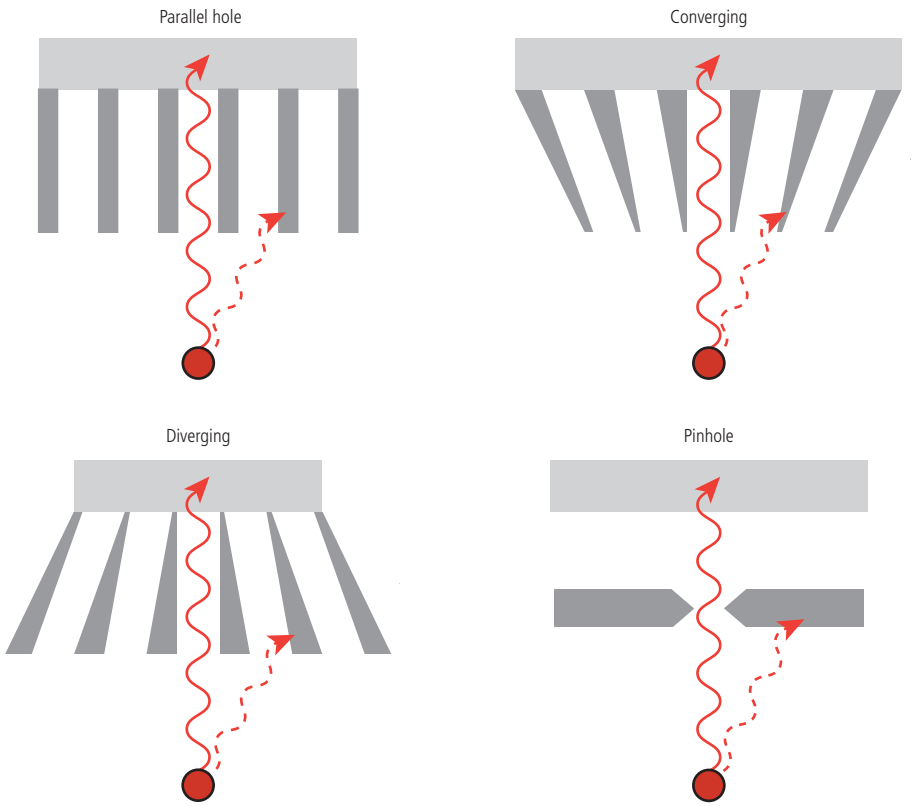

Figure 4: Schematic drawing of a parallel hole, converging, diverging and pinhole collimator.

Converging collimators and diverging collimators are similar to parallel hole collimators, except that the holes are not parallel but focussed on a specific point in space. In case of a converging collimator, this point lies in front of the collimator, resulting in an enlargement of the imaged object on the gamma camera. Although sensitivity is increased with respect to a parallel hole collimator, this comes at the price of a smaller field of view (FOV). Diverging collimators have their focal point at the backside of the collimator. This results in a large FOV and a minimisation of the imaged object, but also a lower resolution with respect to the standard parallel hole collimator.

Pinhole collimators apply the working principle of a "camera obscura", providing an inverted projection of the object on the detector. The magnification factor depends on the pinhole-detector distance and the object-pinhole distance. Pinhole collimators generally have a higher resolution than parallel hole collimators due to their magnifying capability, but are less sensitive and often have a small FOV.

Image degrading effects

Although a collimator is helpful in creating useful projection images, there remain some effects that degrade image quality. First of all, collimator holes have a finite width and therefore photons are accepted from a certain opening angle, instead of only photons travelling parallel to the septa. In addition, absorption collimation is not perfect, since photoelectric absorption is a

probabilistic effect. A small fraction of photons will penetrate the collimator septa and hit the detector. This, as well as scattered photons in the collimator hitting the detector, further degrades image resolution, increases noise and reduces contrast.

Another effect that degrades image resolution is the intrinsic resolution of the gamma camera. The intrinsic resolution is related to uncertainty in the estimation of the position of the scintillation event by the gamma camera. For a typical NaI(Tl) gamma camera, the intrinsic resolution is in the order of a few millimetres.

Other important image degrading effects are attenuation and scatter of gamma photons in the patient. As gamma photons travel through tissue, there is an increasing chance of interaction with the tissue. Therefore, only a fraction of the gamma photons leaves the body. Depending on the distance the photons have to travel and the energy of the photons, a significant part of the photons is attenuated, mainly by Compton scatter and for a small part by photoelectric absorption.

The Compton scattered photons may still be detected by the gamma camera at a more or less random position. During Compton scatter, the energy and direction of the gamma photon are changed. Therefore, a photon first travelling in a non-accepted direction might scatter into a direction that is accepted by the collimator. The original position of this scattered photon cannot be reconstructed, thus degrading image quality. Luckily, the energy of a scattered photon is also changed. This makes it possible to reject part of the scattered photons by energy selection.

Image reconstruction

When multiple two-dimensional projection images over multiple angles are acquired, a three-dimensional image of the activity distribution can be reconstructed. Traditionally, filtered backprojection was used, which is a fast and simple method of tomographic reconstruction. Nowadays, iterative reconstruction methods, such as maximum likelihood expectation-maximisation (MLEM) (11) and ordered subset expectation-maximisation (OSEM) (12), are clinically used. Iterative reconstruction methods are slower than filtered backprojection. The advantage, however, is that physical processes degrading image quality can be modelled into the reconstruction, which improves the accuracy of the reconstruction.

The finite resolution of the collimator and the intrinsic resolution of the gamma camera causes the edges of the imaged object to be blurred. By measuring or simulating the response of the collimator plus gamma camera to a point source at different distances of the gamma camera, point spread functions (PSFs) can be obtained. These PSFs can be incorporated into the reconstruction algorithm. This improves the accuracy of the reconstructed image by sharpening the edges.

Corrections for attenuation effects can be incorporated into the reconstruction algorithm by taking into account the attenuation coefficient of the tissue and the estimated path length through the tissue. The required attenuation coefficients can be obtained from a co-registered computed tomography (CT) scan, which is often acquired directly after the acquisition of the SPECT projections.

Correction for scatter of gamma photons is in clinical practice often performed using the triple energy window method (13). This involves acquiring projections in three energy windows: one around the photopeak of the imaged isotope, one above the photopeak and one below the photopeak. The amount of scatter is then estimated by averaging the amount of photons in the upper and lower energy windows for each projection. More advanced scatter correction methods

involve estimating the scatter components iteratively during the reconstruction (14) or using Monte Carlo techniques for scatter correction (15).

Role of SPECT in radioembolisation

In the radioembolisation workflow, SPECT/CT is used during the pre-treatment procedure to assess the distribution of the ^{99m}Tc-MAA particles. The gamma cameras are mounted with low-energy-high-resolution parallel hole collimators and both planar and SPECT/CT images are acquired. Lung shunt fraction is then estimated from planar images, while the presence of extrahepatic distributions is assessed on the SPECT/CT scan. Subsequently, the SPECT/CT scan is used to calculate the required amount of ^{90}Y activity to be administered during treatment (16).

Positron emission tomography

Positron emission tomography (PET) is another important nuclear imaging modality used in radioembolisation. Just like a SPECT system, PET relies on the detection of gamma photons originating from radionuclide decay after which the three-dimensional activity distribution can be reconstructed. An image of a typical PET system is shown in Figure 5.

Photon detection

PET imaging is based upon coincidence detection of two annihilation photons. When a positron is emitted upon radioactive decay, the positron will annihilate with an electron. This produces two 511 keV gamma photons travelling in opposite directions. The principle of PET relies on the detection of these two gamma photons on opposite sides of the detection ring. A "count" is acquired when two gamma photons hit the detection ring within the coincidence timing window. The annihilation event is then supposed to have occurred on a virtual straight line between the two hits: the line of response. The detection principle of the gamma photons in the detection ring is identical to the detection principle in a gamma camera (scintillation crystal with PMTs).

Figure 5: Typical example of a clinical PET/CT system (courtesy Philips Healthcare).

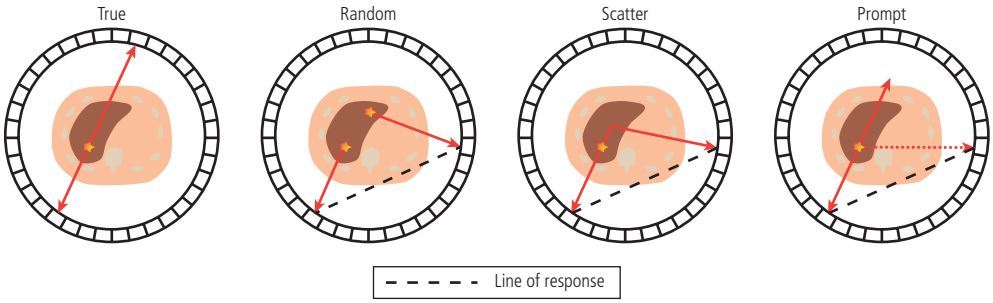

Figure 6: Schematic drawing of count detection in PET. The resulting line of response is represented by the black dashed line.

Image degrading effects

When two gamma photons are detected within the coincidence timing window, they are stored as a count. If the annihilation event lies on the line of response and the two photons originate from the same annihilation event, this is called a true count. Two photons from two different annihilation events can also be detected within the coincidence timing window. This is called a random event, which creates an erroneous line of response, degrading image quality. An erroneous line of response can also be created when two photons of the same annihilation event are detected, but one of them is scattered. Finally, an erroneous line of response can occur in the case of a "prompt". This can happen for some isotopes that decay in a cascade of events. Besides positrons, other gamma photons are also emitted in the decay cascade. The detection of such a gamma photon within the coincidence timing window results in an erroneous line of response. The different originations of lines of responses are illustrated in Figure 6.

Image reconstruction

PET images are generally reconstructed using the ordered subset expectation-maximisation (OSEM) algorithm (12). Just like in SPECT, attenuation can be corrected for by incorporating an attenuation map based on a co-registered CT scan into the reconstruction algorithm and blurring due to the intrinsic resolution of the PET detectors is corrected for by incorporating PSFs into the reconstruction algorithm.

Scatter is estimated by either modelling the photon interaction physics or by fitting the tails of the projection profiles (17). The amount of randoms is estimated by applying a delayed coincidence timing window. Both randoms and scatter can be corrected for by subtracting the estimation from the sinogram before reconstruction or by adding the estimations to the sinogram in the forward projection.

Due to the different path lengths that the two annihilation photons have to travel before reaching a detection crystal, a small time difference exists between the detection of the two photons. This time difference contains information on where the annihilation occurred along the line of response. This time of flight (TOF) information can be incorporated into the reconstruction to improve the accuracy.

Role of PET in radioembolisation

PET imaging after radioembolisation has an important role in research settings. For example, ^{90}Y PET imaging can be performed after treatment to verify the distribution. Furthermore,

Figure 7: Image of a mobile fluoroscopy system (courtesy Philips healthcare).

PET imaging with fluor-18-deoxyglucose (FDG) can be used to monitor response (17). These images can be analysed together to investigate dose-response relationships (18).

Fluoroscopy

Fluoroscopy is an x-ray imaging technique that allows real-time imaging. It is mainly used in the intervention room or operating theatre to guide angiographic and minimally invasive procedures, including radioembolisation procedures. A fluoroscopy system consists of an x-ray tube and an x-ray detector, connected by a mechanical construction in the form of a "C" to keep them opposite to each other. A fluoroscopy system is therefore also called a c-arm. Figure 7 shows an image of a fluoroscopy system.

X-ray tube

X-ray photons are generated in an x-ray tube by heating of the cathode, which frees electrons. These electrons are accelerated through an electric field towards the anode. Upon collision with the anode, x-ray photons are created as a consequence of the Bremsstrahlung effect.

X-ray detector

Traditionally, x-ray image intensifiers are used to convert the x-rays into a viewable image. First, x-ray photons are converted to optical photons due to absorption in a phosphorous layer. These optical photons are subsequently converted to photoelectrons by a photocathode. The photoelectrons are accelerated by a potential difference and focussed with electron lenses to the size of the output window. Upon impact on the phosphorous output window, the electrons are converted to optical photons, which are captured by a charge coupling device (CCD). Due to the acceleration of the photoelectrons, much more optical photons are created at the output phosphorous layer than at the input, thus leading to an intensification of the brightness.

Nowadays, digital flat panel detectors are more and more used in c-arm systems. Such flat panel detectors typically contain a layer of CsI, which converts the x-ray photons to optical photons. The optical photons are detected by photodiodes, generating an electrical signal that is proportional to the amount of light produced in front of the photodiode. Electronics are used to amplify and encode the electric signals from the photodiodes in order to produce an image (19,20).

Role of fluoroscopy in radioembolisation

Fluoroscopy is used in the pre-treatment procedure to assess the vascular anatomy and to position the catheter at the preferred injection position. During actual treatment, fluoroscopy is again

used to guide the catheter into place and to check whether the injection position equals the injection position during the pre-treatment procedure. When this is the case, treatment continues with the injection of the radioactive microspheres.

Hybrid imaging

Availability of hybrid images in the intervention room would allow single-session radioembolisation procedures. Nuclear images provide the physician with molecular information about the patient, but lack anatomical information. In a diagnostic setting, this is solved by combining the SPECT or PET scanner with a CT scanner into one hybrid imaging modality: SPECT/CT or PET/CT. In the intervention room, a fluoroscopy system provides the physician with anatomical images, but this system lacks the nuclear information. In theory, a SPECT/CT or PET/CT system could be used in the intervention room. However, anatomical and nuclear images are acquired in sequence, which is not ideal for the dynamic nature of the procedure. In addition, the closed gantry of such a system restricts the operating space available for the physician. Alternatively, gamma probes or hand-held gamma cameras can be used in the intervention room. However, information of these systems can be difficult to interpret due to the lack of co-registered anatomical information.

We aim at developping a hybrid imaging system that is able to simultaneously and in real-time acquire nuclear and anatomical images in the intervention room. A first prototype has been developed by Beijst et al. (21). This prototype consisted of a mobile c-arm with a gamma camera placed behind the x-ray tube. Four pinholes were positioned around the x-ray tube to create stereoscopic views of the field of view. A rendering of the prototype is shown in Figure 8. Although proven to be feasible, this design was not optimised and further research is needed regarding the design and application of such a hybrid imaging system.

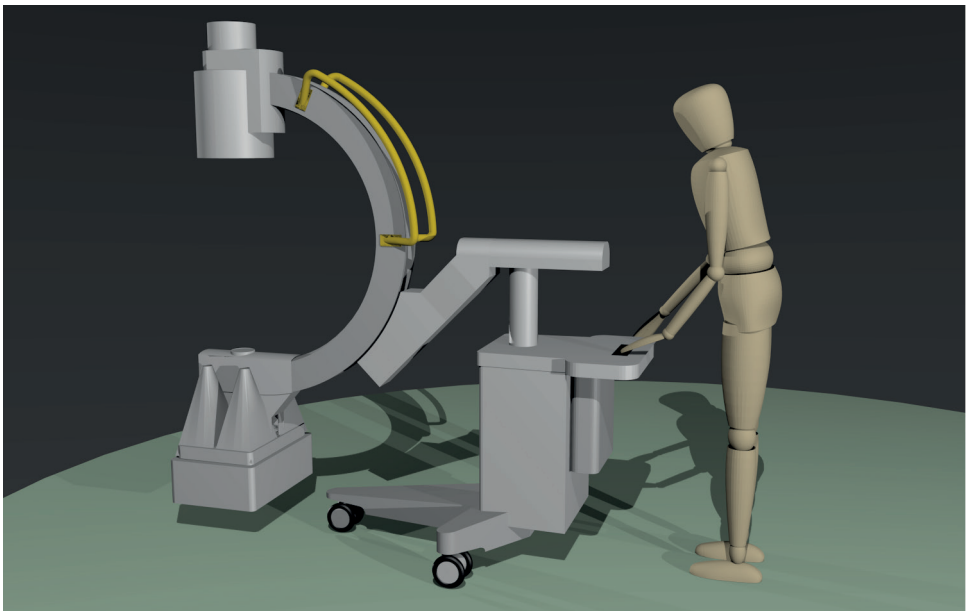

Figure 8: Rendering of hybrid nuclear and fluoroscopic image device.

Thesis outline

Part I

The aim of this thesis is to investigate the development and application of a device which can acquire both fluoroscopic and nuclear images in the intervention room for guidance of liver radioembolisation procedures. The first part of this thesis describes the development of the hardware required for such a device.

Although the first design of a hybrid imaging device by Beijst et al. (21) proved the concept to be feasible, the design was not optimised for nuclear image quality. **Chapter 2** investigates whether nuclear image quality can be improved by the use of a different kind of collimator.

There are several disadvantages of the initial design with the gamma camera at the side of the x-ray tube. First, the resolution is low, due to the large distance from the patient to the gamma camera. Second, an intermediate reconstruction step is needed to create a hybrid image. In **Chapter 3**, the technical feasibility of a new design is investigated. In this design, the gamma camera is positioned behind the x-ray flat panel. The concept relies on the fact that the x-ray flat panel is relatively transparent for the high energy gamma photons, while the lower energy x-ray photons will be stopped in the x-ray flat panel. By the use of a converging collimator, intrinsic registered hybrid images can be obtained.

Part II

The second part of this thesis focusses on the improvement of radioembolisation procedures by interventional hybrid imaging and other nuclear imaging techniques. The main point of improvement investigated is the possibility to perform the radioembolisation procedure in a single session. This has the advantage of shortening treatment times (8,9) and using the same injection position for both the scout and treatment dose (7). In addition, the potential of using a nuclear imaging technique to monitor regional liver function in radioembolisation is discussed.

Accurate and fast scout dose evaluation is crucial when radioembolisation is performed in a single session. The scout dose is primarily used to estimate the fraction of microspheres shunting to the lungs: the lung shunt fraction. If a too large portion of microspheres shunts to the lungs, the treatment dose may be lowered or treatment may be abandoned (22). **Chapter 4** evaluates whether the lung shunt fraction can be fast and accurately determined in the intervention room using our hybrid imaging device.

To better tailor treatment dose to individual patients, a SPECT/CT scan of the scout dose can be made. Clinically, such a SPECT/CT scan takes 30 minutes, which is too long for interventional purposes. The purpose of **Chapter 5** is to investigate if acquisition times can be shortened without losing accuracy on important dosimetric metrics.

Radioembolisation is increasingly used as a bridge to resection (i.e. radiation lobectomy). It combines ipsilateral tumour control with the induction of contralateral hypertrophy to facilitate lobar resection. Although considered curative, many patients are excluded from surgery because of inadequate future liver remnant volume. Liver function might provide additional information regarding the eligibility of patients and can be assessed on a regional level using hepatobiliary scintigraphy (HBS). In **Chapter 6**, the potential complementary value of regional function assessment by HBS in the management of radiation lobectomy is investigated.

Finally, this thesis is discussed and summarised in **Chapter 7**.

References

1. RC Bakker, RJJ van Es, AJWP Rosenberg, SA van Nimwegen, R Bastiaannet, HWAM de Jong, et al., Intratumoral injection of radioactive holmium-166 microspheres in recurrent head and neck squamous cell carcinoma, Nucl. Med. Commun., 2018, 39(3):213.
2. A Dash, FF Knapp, and M Pillai, Targeted Radionuclide Therapy - An Overview, Curr. Radiopharm., 2013, 6(3):152–80.
3. A Kennedy, D Coldwell, B Sangro, H Wasan, and R Salem, Radioembolization for the Treatment of Liver Tumors, Am. J. Clin. Oncol., 2012, 35(1):91–9.
4. AJAT Braat, MLJ Smits, MNGJA Braat, AF van den Hoven, JF Prince, HWAM de Jong, et al., ^{90}Y Hepatic Radioembolization: An Update on Current Practice and Recent Developments, J. Nucl. Med., 2015, 56(7):1079–87.
5. MAD Vente, M Wondergem, I van der Tweel, MAAJ van den Bosch, BA Zonnenberg, MGEH Lam, et al., Yttrium-90 microsphere radioembolization for the treatment of liver malignancies: A structured meta-analysis, Eur. Radiol., 2009, 19(4):951–9.
6. A Kennedy, S Nag, R Salem, R Murthy, AJ McEwan, C Nutting, et al., Recommendations for Radioembolization of Hepatic Malignancies Using Yttrium-90 Microsphere Brachytherapy: A Consensus Panel Report from the Radioembolization Brachytherapy Oncology Consortium, Int. J. Radiat. Oncol. Biol. Phys., 2007, 68(1):13–23.
7. E Garin, J Edeline, and Y Rolland, High Impact of Preferential Flow on ^{99m}Tc-MAA and ^{90}Y-Loaded Microsphere Uptake Correlation, J. Nucl. Med., 2016, 57(11):1829–30.
8. A Gabr, JR Kallini, VL Gates, R Hickey, L Kulik, K Desai, et al., Same-day ^{90}Y radioembolization: implementing a new treatment paradigm, Eur. J. Nucl. Med. Mol. Imaging, 2016, 43(13):2353–9.
9. VL Gates, KG Marshall, K Salzig, M Williams, RJ Lewandowski, and R Salem, Outpatient Single-Session Yttrium-90 Glass Microsphere Radioembolization, J. Vasc. Interv. Radiol., 2014, 25(2):266–70.
10. SR Cherry, JA Sorenson, and ME Phelps, Physics in Nuclear Medicine - The Gamma Camera, Fourth edi. Elsevier; 2012.
11. LA Shepp, and Y Vardi, Maximum Likelihood Reconstruction for Emission Tomography, IEEE Trans. Med. Imaging, 1982, 1(2):113–22.
12. HM Hudson, and RS Larkin, Accelerated image reconstruction using ordered subsets of projection data, IEEE Trans. Med. Imaging, 1994, 13(4):601–9.
13. K Ogawa, Y Harata, T Ichihara, A Kubo, and S Hashimoto, A practical method for position-dependent Compton-scatter correction in single photon emission CT, IEEE Trans. Med. Imaging, 1991, 10(3):408–412.
14. SR Meikle, BF Hutton, and DL Bailey, A transmission-dependent method for scatter correction in SPECT, J. Nucl. Med., 1994, 35(2):360–7.
15. FJ Beekman, HWAM De Jong, and S Van Geloven, Efficient fully 3-D iterative SPECT reconstruction with Monte Carlo-based scatter compensation, IEEE Trans. Med. Imaging, 2002, 21(8):867–77.
16. SA Gulec, G Mesoloras, and M Stabin, Dosimetric Techniques in ^{90}Y-Microsphere Therapy of Liver Cancer: The MIRD Equations for Dose Calculations, 2016, 47(7):1209–12.

17. A Sabet, H Ahmadzadehfar, J Bruhman, A Sabet, C Meyer, J-C Wasmuth, et al., Survival in patients with hepatocellular carcinoma treated with ^{90}Y-microsphere radioembolization, Nuklearmedizin, 2014, 53(2):39–45.
18. AF van den Hoven, CENM Rosenbaum, SG Elias, HWAM de Jong, M Koopman, HM Verkooijen, et al., Insights into the Dose-Response Relationship of Radioembolization with Resin ^{90}Y-Microspheres: A Prospective Cohort Study in Patients with Colorectal Cancer Liver Metastases, J. Nucl. Med., 2016, 57(7):1014–9.
19. K Kump, P Grantors, F Pla, and P Gobert, Digital X-ray detector technology, RBM-News, 1998, 20(9):221–6.
20. E Kotter, and M Langer, Digital radiography with large-area flat-panel detectors, Eur. Radiol., 2002, 12(10):2562–70.
21. C Beijst, M Elschot, MA Viergever, and HWAM de Jong, Toward Simultaneous Real-Time Fluoroscopic and Nuclear Imaging in the Intervention Room, Radiology, 2016, 278(1):232–8.
22. Sirtex Medical Limited, SIR-Spheres package insert (CR1507), North Sydney, NSW, Australia: 2012.

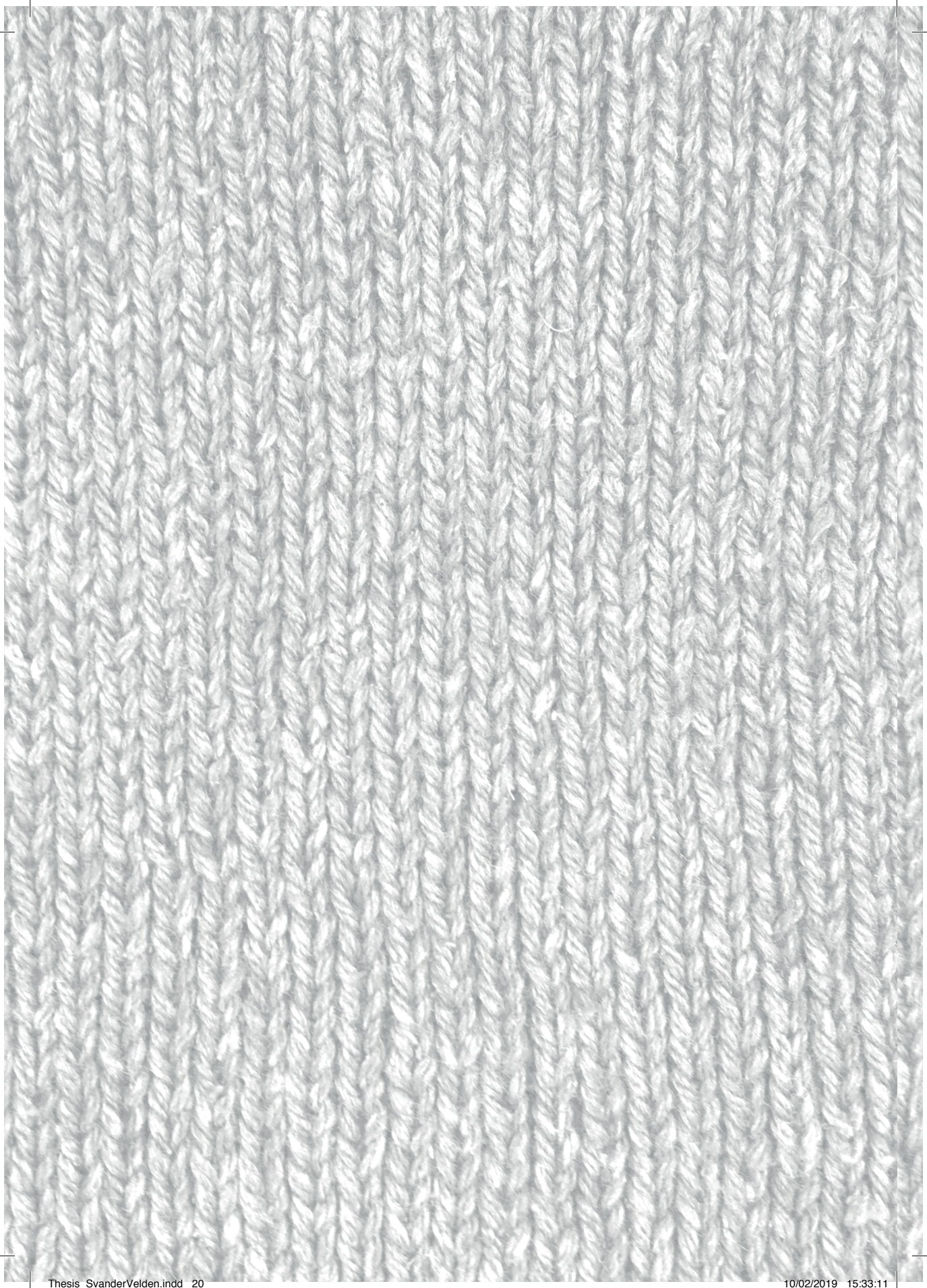

2

Simultaneous fluoroscopic and nuclear imaging - Impact of collimator choice on nuclear image quality

Based on:

S. van der Velden, C. Beijst, M.A. Viergever, H.W.A.M. de Jong, "Simultaneous fluoroscopic and nuclear imaging: Impact of collimator choice on nuclear image quality", Medical Physics, 2017, nr. 1, vol. 44, pp. 249-26

Abstract

Purpose

X-ray guided oncological interventions could benefit from the availability of simultaneously acquired nuclear images during the procedure. To this end, a real-time, hybrid fluoroscopic and nuclear imaging device, consisting of an x-ray c-arm with gamma imaging capability, is currently being developed. The set-up comprises four gamma cameras placed adjacent to the x-ray tube. The four camera views are used to reconstruct an intermediate three-dimensional image, which is subsequently converted to a virtual nuclear projection image that overlaps with the x-ray image. The purpose of this simulation study was to evaluate the impact of gamma camera collimator choice (parallel hole versus pinhole) on the quality of the virtual nuclear image.

Materials and methods

Simulations were performed with a digital image quality phantom including realistic noise and resolution effects, with a dynamic frame acquisition time of 1 s and a total activity of 150 MBq. Projections were simulated for 3, 5 and 7 mm pinholes and for three parallel hole collimators (low-energy-all-purpose (LEAP), low-energy-high-resolution (LEHR) and low-energy-ultra-high-resolution (LEUHR)). Intermediate reconstruction was performed with a maximum likelihood expectation-maximisation algorithm with point spread function modelling. In the virtual projection derived therefrom, contrast, noise level and detectability were determined and compared with the ideal projection, i.e. as if a gamma camera were located at the position of the x-ray detector. Furthermore, image deformations and spatial resolution were quantified. Additionally, simultaneous fluoroscopic and nuclear images of a sphere phantom were acquired with a physical prototype system and compared with the simulations.

Results

For small hot spots, contrast was comparable for all simulated collimators. Noise levels were, however, 3 to 8 times higher in pinhole geometries than in parallel hole geometries. This resulted in higher contrast-to-noise ratios for parallel hole geometries. Smaller spheres could thus be detected with parallel hole collimators than with pinhole collimators (17 mm vs 28 mm). Pinhole geometries showed larger image deformations than parallel hole geometries. Spatial resolution varied between 1.25 cm and 4 cm for the 3 mm pinhole and the LEAP collimator, respectively. The simulation method was successfully validated by the experiments with the physical prototype.

Conclusion

A real-time hybrid fluoroscopic and nuclear imaging device is currently being developed. Image quality of nuclear images obtained with different collimators was compared in terms of contrast, noise and detectability. Parallel hole collimators showed lower noise and better detectability than pinhole collimators.

Introduction

Hybrid imaging modalities, like single photon emission computed tomography (SPECT)/computed tomography (CT) and positron emission tomography (PET)/CT, have revolutionised oncological imaging in the past decades, combining anatomical and molecular information for improved diagnostic power (1,2). In these modalities, CT and SPECT or PET operate in sequence, after which an overlay or fusion image is created. Although PET/CTs have been used in interventional settings (3), the closed gantry and sequential imaging are suboptimal for interventional procedures. Moreover, an x-ray c-arm is often preferred over a CT scanner for guidance of interventions. Therefore, a real-time, simultaneous fluoroscopic and nuclear imaging device, consisting of a c-arm with gamma imaging capability, would be more fitting for an interventional setting. Such a system, in which fluoroscopic x-ray imaging is combined with four gamma cameras, is currently being developed by our group (4).

The objective of the hybrid imaging device is to give a quick insight into radionuclide distributions using live images rather than providing static images with the highest diagnostic image quality. Image guided procedures, such as sentinel node procedures (5) or liver radioembolisation (6), could benefit from the availability of live hybrid images during interventions by providing the physician with additional information. For example, during liver radioembolisation procedures, assessment of complete or partial liver treatment could be performed, as well as assessment of possible lung shunting or other extrahepatic depositions (7).

Simultaneous fluoroscopic and nuclear imaging of the same field of view (FOV) requires an x-ray tube, an x-ray detector and a gamma camera with collimator. Placing these components in one line results in blocking the line of sight of either one of the modalities. This problem can be overcome by acquiring projections from a number of gamma cameras symmetrically placed around the x-ray tube to create stereoscopic views of the FOV (Figure 1a). These projections can then be converted to a virtual projection that overlaps with the x-ray image. This conversion can be implemented as a two-step process. First, a three-dimensional image is reconstructed from the nuclear projections. Second, the virtual projection is calculated from the reconstruction.

Reconstruction of one concurrent nuclear image from a small number of projections with low count statistics is a challenge in our new modality. Nuclear image quality of the hybrid image is affected by resolution and count statistics of the acquired nuclear projections. To perform imaging with short frame durations, high gamma ray detection efficiency is required. However, increasing the efficiency comes at the expense of a decreased resolution (8). Both efficiency and resolution are dependent on the collimator design and the position of the gamma camera with respect to the radioactive source.

The four gamma cameras of the hybrid imaging device can be equipped with parallel hole or pinhole collimators. Pinholes may allow a compact design, whereas parallel hole collimators preserve counts at a larger distance. Earlier, we reported about a first pragmatic prototype that relied on one large gamma camera placed behind the x-ray tube, with four pinholes (5 mm diameter) placed next to the x-ray tube (4). With this prototype, we showcased the fundamental feasibility of acquiring hybrid images of the same FOV using simple phantom experiments. Now, before constructing a clinical device, the optimal collimator type and parameters need to be established. The purpose of this simulation study was to evaluate the impact of collimator choice on nuclear image quality of the virtual projection.

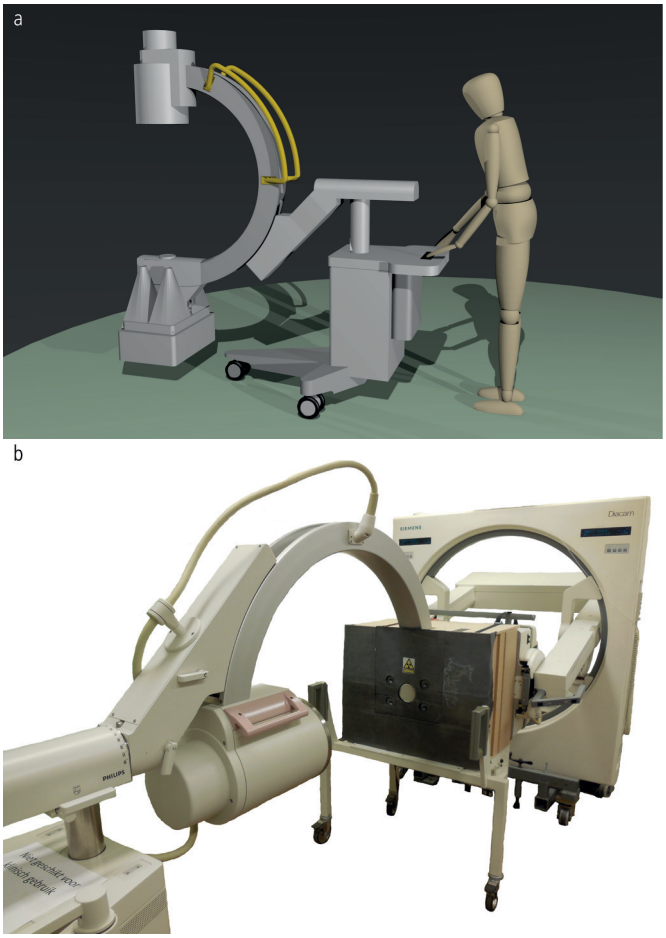

Figure 1: Rendering (a) and physical prototype (b) of the simultaneous fluoroscopic and nuclear imaging device.

Table 1: Parameters of LEAP, LEHR and LEUHR parallel hole collimator in [mm].

Collimator	Hole diameter	Septal length	Septal width
LEAP	1.45	24.05	0.20
LEHR	1.11	24.05	0.16
LEUHR	1.16	35.80	0.13

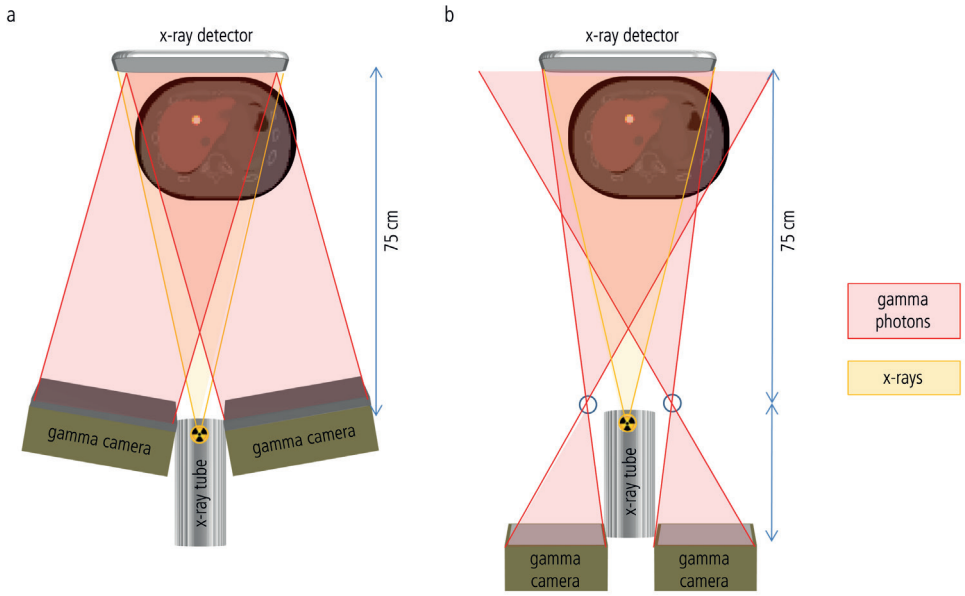

Figure 2: Schematic drawing of proposed geometries: (a) parallel hole collimator geometry and (b) pinhole collimator geometry. The pinholes and the centres of the parallel hole collimators are placed at a distance of 75 cm from the x-ray detector.

Materials and methods

Collimator geometry

In the current prototype, four 5 mm pinholes in combination with one large gamma camera are used (Figure 1b) (4). A more flexible design can be obtained by using four smaller gamma cameras instead of one large gamma camera. In addition, nuclear image quality might be improved by using gamma cameras with parallel hole collimators or pinholes with a different diameter. To investigate which collimator geometry would perform best, six options were considered: three parallel hole collimators and three pinhole collimators. Parallel hole collimators have the advantage of a high sensitivity compared with pinhole collimators, which yields higher count statistics. However, this comes at the expense of a lower resolution. On the other hand, pinhole collimators can be used with smaller gamma cameras by virtue of potential minimisation. This allows a more compact design, which is beneficial from a mechanical point of view. However, pinhole collimators may be limited in terms of sensitivity and resolution when operated in minimisation mode compared with parallel hole collimators at larger distances (8,9).

Table 1 shows the parameters of the simulated parallel hole collimators. A low-energy-all-purpose (LEAP), a low-energy-high-resolution (LEHR) and a low-energy-ultra-high-resolution (LEUHR) parallel hole collimator were simulated with four gamma cameras of 30.72 by 30.72 cm each. The gamma cameras were placed around the x-ray tube at 75 cm from the x-ray detector. The gamma camera with collimator was rotated such that the centre of the collimator was looking towards the centre of the reconstructed three-dimensional activity distribution. Figure 2a shows a schematic drawing of the parallel hole collimator geometry.

Pinholes with a diameter of 3, 5 and 7 mm were simulated with the four pinholes placed at 75 cm from the x-ray detector. The gamma cameras of 15.36 by 15.36 cm were placed at a distance of 30 cm from the pinhole. Pinholes were placed such that the centre of the FOV was projected onto the centre of the detector. Figure 2b shows a schematic drawing of the pinhole collimator geometry.

As a reference, the current physical prototype (Figure 1b) was also simulated. In the prototype, a pinhole diameter of 5 mm was used, with the pinholes placed at 77.76 cm from the x-ray detector. The gamma camera was placed at a distance of 38.90 cm from the pinholes. The pinholes were placed such that the centre of the FOV was imaged in all four projections.

Digital phantom

The digital phantom used in this study consisted of a cylinder of 20 cm diameter and 4.56 cm height with spheres of 13, 17, 22, 28 and 37 mm diameter, respectively. This phantom mimics part of the liver, and the volume of the cylinder (1432 ml) roughly corresponds to the volume of activity accumulation in liver radioembolisation. The sphere sizes correspond to the five largest spheres of the NEMA 2007/IEC 2008 Positron Emission Tomography Image Quality Phantom, which is designed for evaluation of reconstructed image quality (10). The lesion-to-background activity was set to 10:1, which is a common ratio in radioembolisation studies (11).

Virtual projection simulation

Projections of the digital image quality phantom were simulated using a rotation-based projector (12) including noise and resolution effects, with an acquisition time of 1 s and a total activity of 150 MBq technetium-99m (^{99m}Tc). The number of simulated counts was based on the analytical collimator sensitivity, assuming the phantom in the centre of the FOV and taking the yield of ^{99m}Tc into account (8). The calculated sensitivities were validated by comparison with the sensitivities reported in system specifications (13). This could represent typical values for live guidance of a radioembolisation procedure. During the pre-treatement procedure, 150 MBq of ^{99m}Tc-labelled macroaggregated albumin is used. All activity is expected to lodge in the liver (predominantly in the tumours) in a volume of typically 1000 – 1500 ml (6).

To create a perfectly overlapping hybrid image, the four nuclear projections were combined into one concurrent projection (Figure 3). The four projections were first reconstructed into a three-dimensional activity distribution using a maximum likelihood expectation-maximisation (MLEM) algorithm (14). Collimator blurring effects were modelled in the forward and backward projector as a distance-dependent two-dimensional convolution with an analytically determined Gaussian point spread function (PSF) (15). For parallel hole collimators, the full width at half maximum (FWHM) of the distance-dependent PSF was modelled as:

$$FWHM = \frac{d \cdot (l_{eff} + b)}{l_{eff}},$$

with d the hole diameter, $l_{eff} = l - 2/\mu$ the effective length of the collimator holes, l the collimator hole length, μ the attenuation coefficient of lead at 140 keV and b the distance from the radiation source to the gamma camera (8). For pinhole collimators, the FWHM of the distance dependent PSF was modelled as:

$$FWHM = \frac{d_{eff} \cdot (l + b)}{l},$$

where

$$d_{eff} = d + \frac{\ln(2)}{\mu}\tan\left(\frac{\alpha}{2}\right),$$

with d_{eff} the effective pinhole diameter, d the pinhole diameter, l the distance from the pinhole to the gamma camera, μ the attenuation coefficient of lead at 140 keV and α the opening angle of the pinhole (90 degrees) (8). Intrinsic resolution of the gamma camera was simulated as a two-dimensional convolution with a 3.8 mm FWHM Gaussian. Scatter and attenuation effects were not incorporated into the forward and backward projectors. Apart from noise, the forward projector was identical for simulation of projections and reconstruction of the activity distribution.

The three-dimensional activity distribution was subsequently projected onto the x-ray detector using a cone beam projection. No collimator blurring, attenuation or scatter effects were modelled in this cone beam projector. This resulted in a projection, called the virtual projection, which is geometrically equal to the x-ray projection. Image quality was evaluated on the virtual projection, since this will be displayed during interventions.

The digital phantom was sampled on a grid of 256 x 256 x 256 voxels with 1.2 x 1.2 x 1.2 mm^3 voxel size. Projections were simulated on a grid of 128 x 128 pixels with 2.4 x 2.4 mm^2 pixel size and reconstructed to a volume of 64 x 64 x 64 voxels with 4.8 x 4.8 x 4.8 mm^3 voxel size to reduce computation time. The virtual projection was calculated on a grid of 64 x 64 pixels with 4.8 x 4.8 mm^2 pixel size.

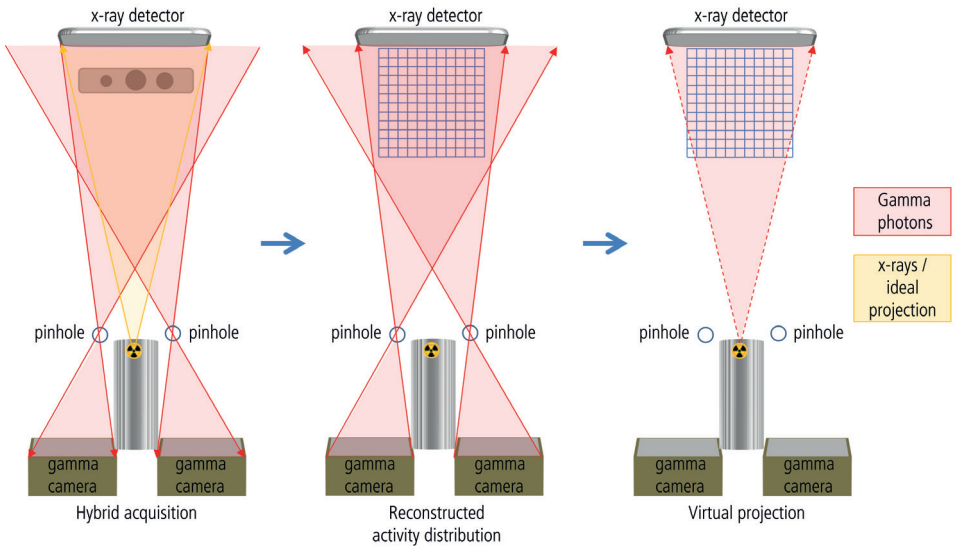

Figure 3: Formation of the concurrent virtual projection from four nuclear projections (geometry of prototype system).

Image quality is dependent on the number of iterations used during reconstruction (16). MLEM is known to increase the noise level when more iterations are used, while contrast becomes better with more iterations (17). The optimal number of iterations per collimator geometry was defined as the number of iterations needed to reach convergence of the 37 mm sphere contrast. That is, contrast of the 37 mm sphere in the virtual projection increased less than 0.1% by doing an extra iteration. The number of iterations needed to reach convergence was not only dependent on the collimator geometry, but also on the noise realisation of the simulated projections. Therefore, we choose to determine the optimal number of iterations in a simulation without noise.

Evaluation of nuclear image quality

As a measure of image quality, image contrast, noise and detectability were calculated. In addition, spatial resolution and image distortions were quantified. The presence and severity of artefact levels were reported.

Image reconstruction from four projections can lead to image distortions. These distortions were quantified by estimating the error in locating the five spheres of the phantom in the virtual projection. The centre of mass of each sphere in the virtual projection was determined for all collimator geometries. The error in locating each sphere was then calculated as the absolute distance between the centre of mass in the virtual projection and the expected position obtained from a direct, noise-free cone beam projection.

For each sphere in the virtual projection, contrast (C) was calculated as:

$$\mathrm{C} = \frac{C_S - C_B}{C_B},$$

where C_S denotes the mean pixel value in the sphere region of interest (ROI) and C_B denotes the mean pixel value in the background ROI. Two-dimensional sphere ROI masks were created by thresholding the cone beam projection of the phantom. The background ROI was defined as the entire projection of the phantom minus the sphere ROIs. To avoid influence of partial volume effects, the background ROI was binary eroded to create a 2 cm margin around the spheres and the phantom edge.

As a measure of image noise, the coefficient of variation (CV) was calculated as:

$$\mathrm{CV} = \frac{\sigma_B}{C_B},$$

with σ_B the standard deviation in the background ROI.

In real-time guidance of oncological procedures, the detectability of small accumulations of activity in a region with background activity is important when tumours cannot be identified on the x-ray image. Accurate identification of a hot spot can only be achieved when the hot spot can be reliably distinguished from the background. Visibility of the spheres in the phantom was assessed by calculating the contrast-to-noise ratio (CNR) as:

$$\mathrm{CNR} = \frac{C_S - C_B}{\sigma_B}.$$

The minimally detectable sphere size was determined according to the Rose criterion (18), which states that the CNR of a lesion has to be larger than five to be detectable.

For comparison purposes, the ideal projection was also constructed and compared with the simulations. The ideal projection was defined as the projection obtained as if there were a gamma camera with a cone beam collimator focussing on the x-ray focal spot at the same position as the x-ray detector, hence capable of directly acquiring gamma images using the x-ray geometry. A low-energy cone beam collimator was simulated with a hole diameter of 1.53 mm, septal length of 35 mm and a septal thickness of 0.16 mm. Count statistics of a single detector are lower than of four detectors combined. Therefore, the ideal projection was post-filtered with a 5 mm FWHM Gaussian to account for differences in noise levels owing to lower count statistics. Contrast, noise level and detectability of the ideal and virtual projections were determined in ten simulations of 1 s acquisition time.

Spatial resolution

A set of digital phantoms consisting of two point sources of 0.5 cm diameter placed 1 to 6 cm apart, with steps of 0.25 cm, was defined to quantify spatial resolution. The two point sources were positioned in the centre of the FOV. This resulted in a set of 21 spatial resolution phantoms. For each collimator geometry, virtual projections of all spatial resolution phantoms were simulated with 3600 s acquisition time and a total activity of 100 MBq ^{99m}Tc. We defined spatial resolution as the minimum distance required between two point sources to be imaged as separate points. To quantify spatial resolution, a profile plot of the centre pixel row through the two point sources was made. Two point sources were considered to be separable if the minimum number of counts between the two peaks was less than half the average peak value.

Comparison of simulated and acquired images

To illustrate the applicability and realism of the simulations, acquisitions of a sphere of 40 mm diameter with 10.7 MBq of ^{99m}Tc against a background of 0.03 MBq/ml were performed with the prototype (Figure 4). Ten acquisitions of 1 s were performed. Virtual projections were created with 10 MLEM iterations to avoid noise amplification in the background. Fluoroscopic images were acquired with a 43 kV tube voltage and a 0.16 mA tube current. For visual purposes, a hybrid image was created by overlaying the virtual projection with the acquired x-ray image.

In addition to the physically measured acquisitions, simulations of the acquired projections were obtained by digitising the phantom on a grid of 256 x 256 x 256 voxels with 1.2 x 1.2 x 1.2 mm^3 voxel size. Ten acquisitions of 1 s were simulated and reconstructed with 10 iterations into a virtual projection. Hybrid images from simulations and measurements were compared visually, as well as in terms of contrast and noise levels.

Simulations of the parallel hole geometry projections were validated with Monte Carlo simulated projections (Utrecht Monte Carlo System (UMCS) and MCNPX) (15,19,20). Nuclear projections of the digital image quality phantom were Monte Carlo simulated for the LEUHR collimator geometry, including all physics in the phantom and detector. The energy window was set to 140 keV ± 15%. Ten acquisitions of 1 s were simulated and reconstructed with identical number of iterations and projectors as in our simulations. Virtual projections from Monte Carlo simulated projections and from our model were compared visually as well as in terms of contrast in the largest sphere and noise levels.

Qualitative assessment of simultaneous fluoroscopic and nuclear images

In addition to static acquisitions, simultaneous fluoroscopic and nuclear images of a dynamic scene were acquired. During acquisition, a syringe was filled with 41 MBq of ^{99m}Tc with activity flowing through a small tube from outside the FOV. Nuclear images were acquired with a frame rate of 2 frames per second and reconstructed with 10 MLEM iterations. Fluoroscopic images were acquired during the entire acquisition time with a 43 kV tube voltage and a 0.16 mA tube current. Hybrid images were created at 5 frames per second. For visual purposes, the nuclear images were super-sampled to match the fluoroscopic images in the temporal domain (4,21).

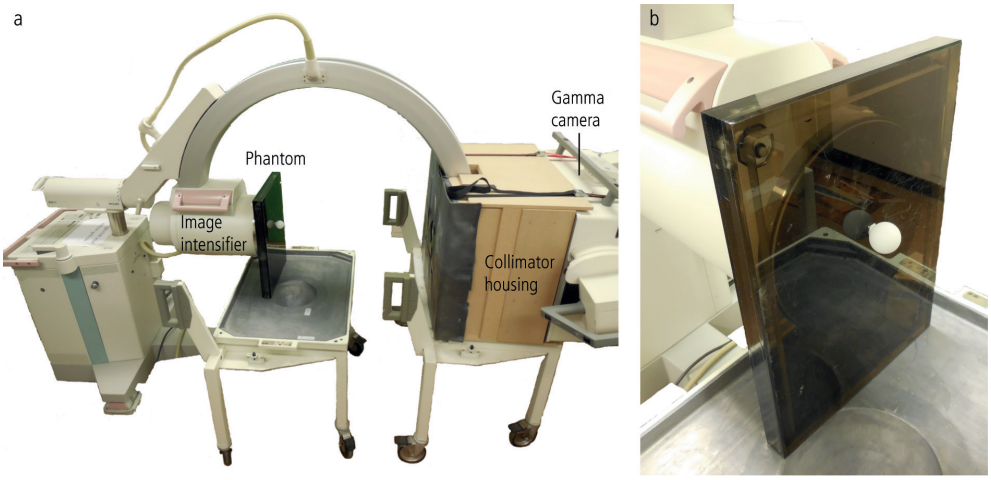

Figure 4: Measurement of a spherical phantom with the physical prototype: (a) overview of set-up and (b) phantom consisting of a 40 mm diameter sphere with 10.7 MBq ^{99m}Tc against a background of 0.03 MBq/ml.

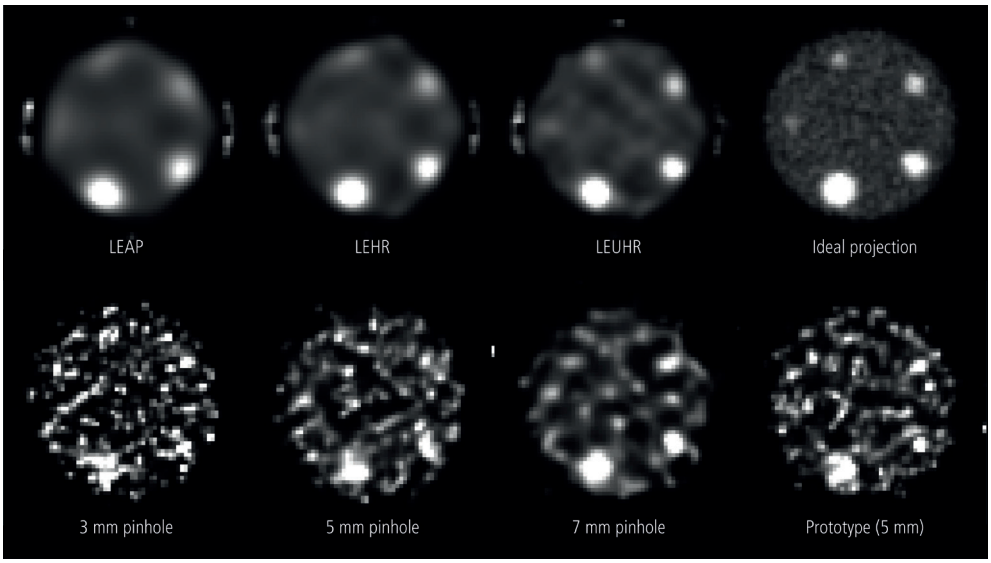

Figure 5: Virtual projections of simulated collimator geometries and for the ideal projection. All images are linearly window-levelled from 0 to 5 times the mean intensity in the background ROI.

Results

Optimal number of iterations

Convergence of contrast in the largest sphere in noise-free simulations was achieved in 87 iterations for the LEAP collimator, in 49 iterations for the LEHR collimator and in 33 iterations for the LEUHR collimator. For the 3, 5 and 7 mm pinhole collimators, 20, 33 and 41 iterations were needed, respectively. Projections of the prototype geometry were reconstructed with 27 iterations. Mean computation time of a single virtual projection was approximately 3 seconds.

Image deformation and artefacts

Figure 5 shows the virtual projections for all simulated collimator geometries and for the ideal projection. In parallel hole geometries, reconstruction artefacts at the sides of the phantom can be observed. Furthermore, slight deformation of the background cylinder was observed, causing the spheres to appear more towards the edges of the cylinder. The differences between the theoretical position and the reconstructed centre of gravity for all sphere sizes and collimator geometries are shown in Figure 6. Differences of locations were larger for pinhole collimator geometries than for parallel hole geometries. In general, the error in locating a sphere became larger with increasing sphere size. Projections of parallel hole geometries appeared more homogeneous than projections of pinhole geometries. Visually, the LEUHR geometry compared best against the ideal projection.

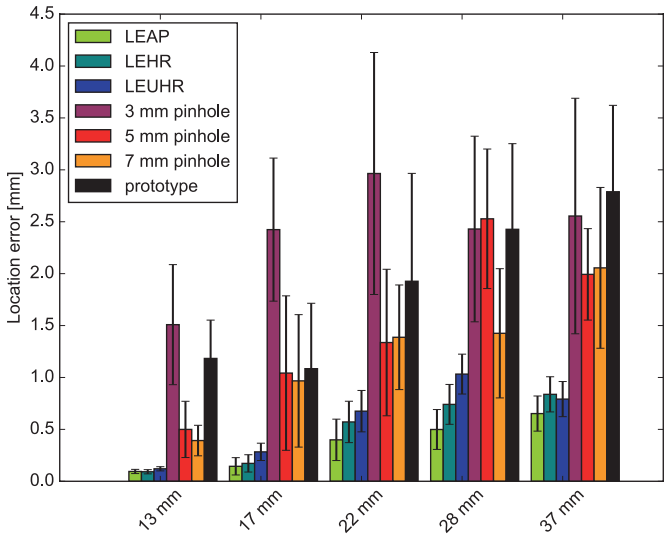

Figure 6: Errors in estimating the location of each sphere in the virtual projection for all simulated collimator geometries. Mean deviation of centre of mass over ten simulations is shown, error bars indicate standard deviation.

Image contrast and noise

Figure 7 shows that contrast increased with sphere size for all simulated geometries. In general, contrast was slightly higher with pinhole geometries than with parallel hole geometries. Contrast was only in the 13 mm sphere higher in the ideal projection than in the simulated geometries. For the 22, 28 and 37 mm spheres, highest contrast was achieved with the 7 mm pinhole. In the 37 mm sphere, contrast was up to 20% lower with 3 mm pinholes than with parallel hole collimators or pinholes of 5 and 7 mm.

Image noise was 3 to 8 times higher in pinhole geometries than in parallel hole geometries (Figure 8a). The noise level in the virtual projections of the parallel hole collimator geometries was comparable with the noise level in the filtered ideal projection. For a fair comparison of image contrast, virtual projections of pinhole geometries were filtered with a 30 mm FWHM post-reconstruction filter to approximately the noise level of the parallel hole collimators (CV ≈ 0.17, Figure 8b). At equal noise level, contrast was substantially lower with pinhole collimators than with parallel hole collimator geometries.

Detectability

Spheres were considered detectable when their CNR was larger than five (18). From Figure 9 it is apparent that the 37 mm sphere could be reliably distinguished from the background in all simulated collimator geometries except for the 3 mm pinhole. Spheres from 17 mm and larger could be detected with all parallel hole collimators. In the ideal projection, also the 13 mm sphere was detectable. For the 3 mm pinhole collimator, none of the spheres could be reliably distinguished from the background noise.

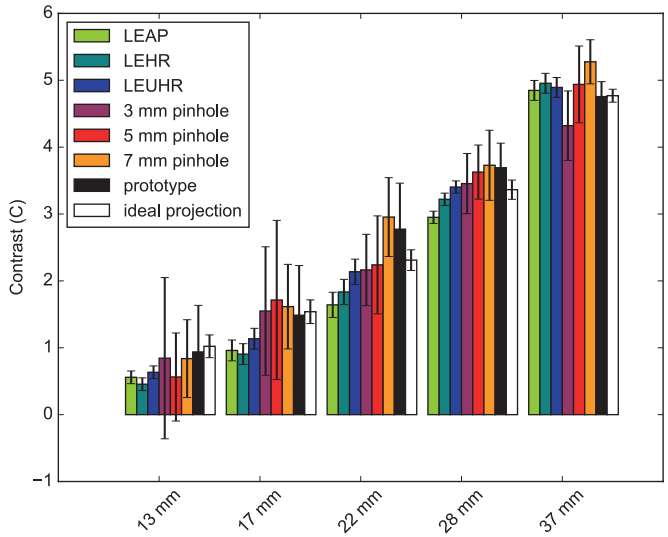

Figure 7: Contrast of spheres in virtual projections for all simulated collimator geometries. Mean contrast over ten simulations is shown, error bars indicate standard deviation.

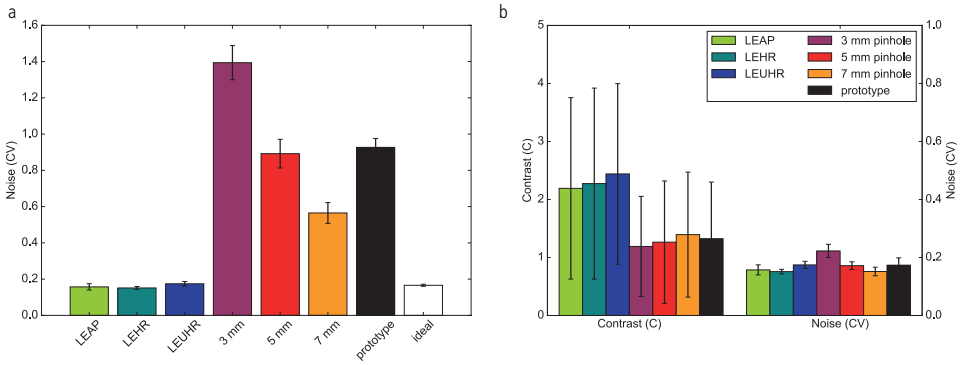

Figure 8: (a) Image noise in the virtual projections for all simulated collimator geometries before filtering. (b) Contrast and noise after filtering of the pinhole projections to approximate the noise level of parallel hole collimators. All results are shown for the 37 mm sphere. Mean contrast and noise over ten simulations is shown, error bars indicate standard deviation.

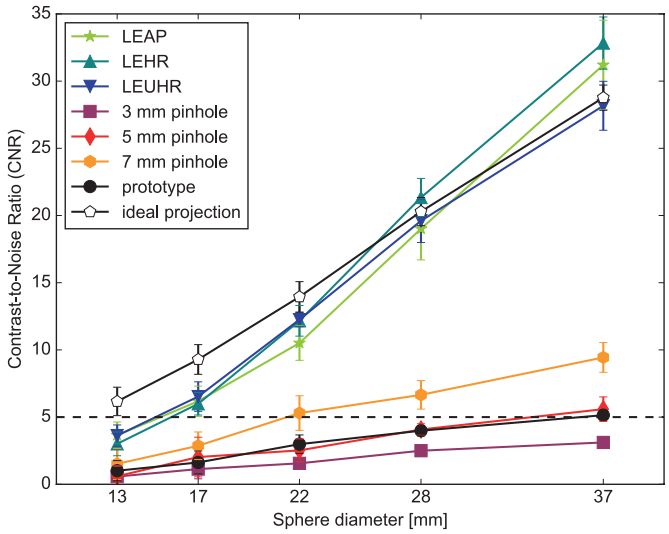

Figure 9: Mean CNR over ten simulations as a function of sphere diameter for all simulated collimator geometries. Error bars indicate standard deviation.

Spatial resolution

Two point sources could be imaged separable if they were placed 4 cm apart for the LEAP collimator, 3.25 cm apart for the LEHR collimator and 2.75 cm apart for the LEUHR collimator. For the 3, 5 and 7 mm pinholes, point sources must be placed 1.25, 1.75, and 2.25 cm apart, respectively. The prototype had a spatial resolution of 1.50 cm. Figure 10 shows the virtual projection and profile plot of the 2.75 cm spatial resolution phantom obtained with the LEUHR collimator in which the two point sources can just be separated.

Comparison of simulated and acquired images

Measured and simulated simultaneous fluoroscopic and nuclear images of the 40 mm sphere phantom are shown in Figure 11. Visual agreement between measured and simulated hybrid images was high. Contrast was slightly higher in the simulated virtual projection (17.58 ± 4.19) than in the virtual projection constructed from the measured projections (15.89 ± 4.43). Noise levels were comparable between the simulations and the measurements (2.32 and 2.08, respectively).

Virtual projections of the digital image quality phantom obtained with Monte Carlo and with our simulations are shown in Figure 12. The contrast in the largest sphere was 4.07 ± 0.19 in the virtual projection originating from Monte Carlo, slightly lower than the contrast of 4.78 ± 0.17 in our simulations. Noise levels were slightly higher in the Monte Carlo projections (0.40 ± 0.09) than in our simulations (0.32 ± 0.08).

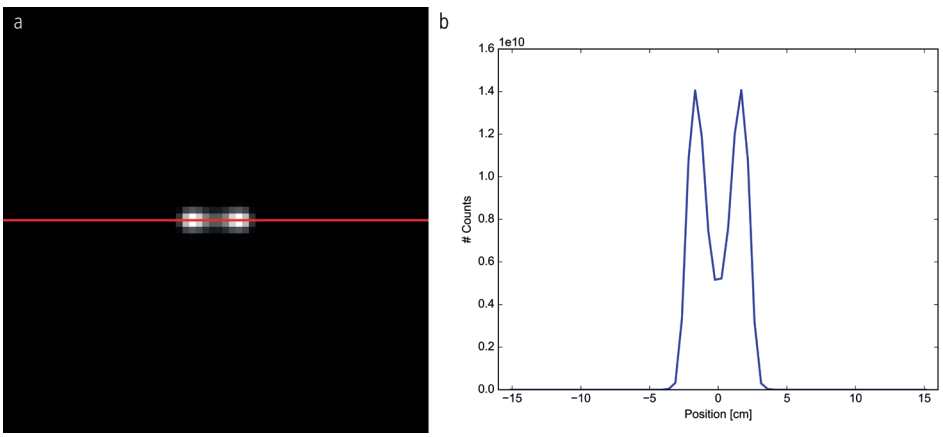

Figure 10: (a) Virtual projection and (b) profile plot of the phantom configuration with 2.75 cm distance between the point sources, obtained with the LEUHR collimator. The red line in (a) indicates the position of the profile plot in (b). These two point sources were considered just to be separable since the minimum number of counts between the two peaks is less than half the average peak value.

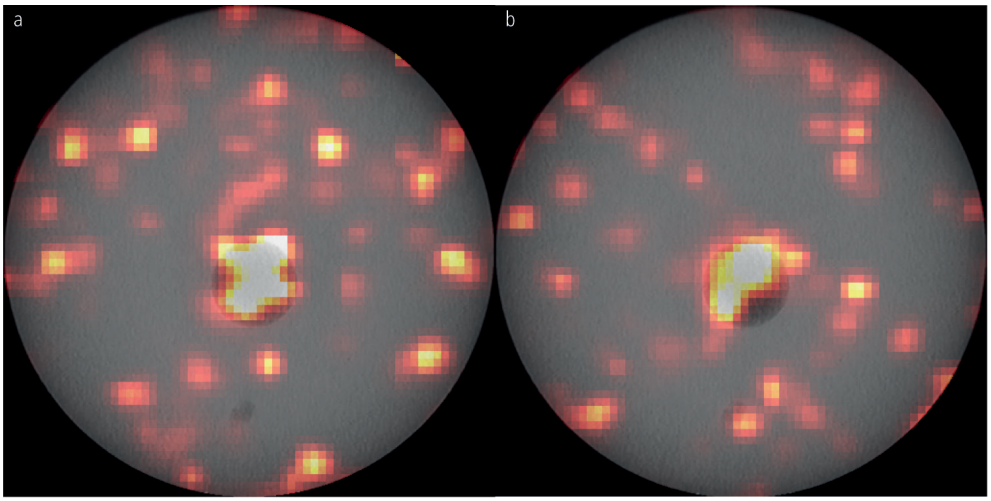

Figure 11: Measured and simulated simultaneous fluoroscopic and nuclear image of the 40 mm sphere phantom with 1 s acquisition time: (a) hybrid image from measured projections and (b) hybrid image from simulated projections.

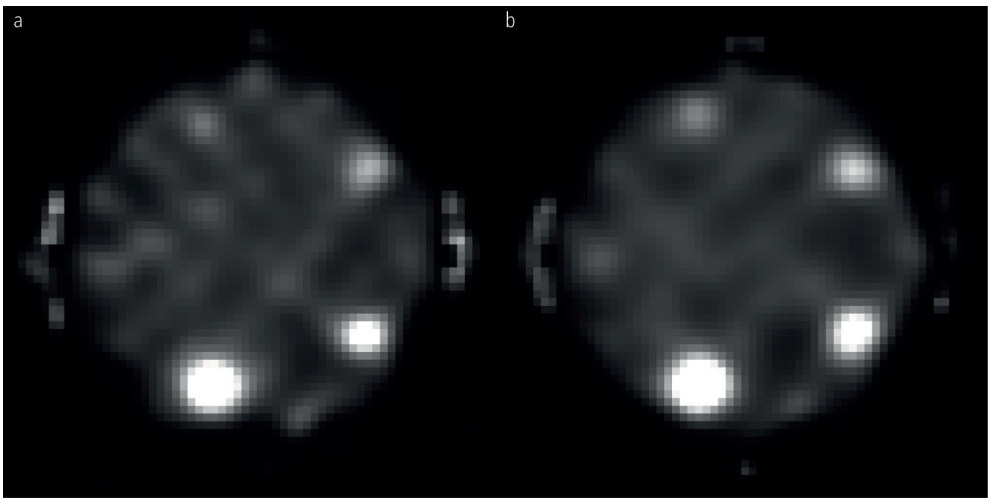

Figure 12: Virtual projection of the digital image quality phantom with the LEUHR collimator: (a) virtual projection obtained from Monte Carlo and (b) virtual projection obtained from our simulations.

Qualitative assessment of simultaneous fluoroscopic and nuclear images

Figure 13 shows the simultaneously acquired dynamic fluoroscopic and nuclear images of a syringe filled with 41 MBq of ^{99m}Tc. Fluoroscopic images were shown in grayscale and nuclear images in colour overlay. Visual inspection of the images showed a good spatial and temporal overlay.

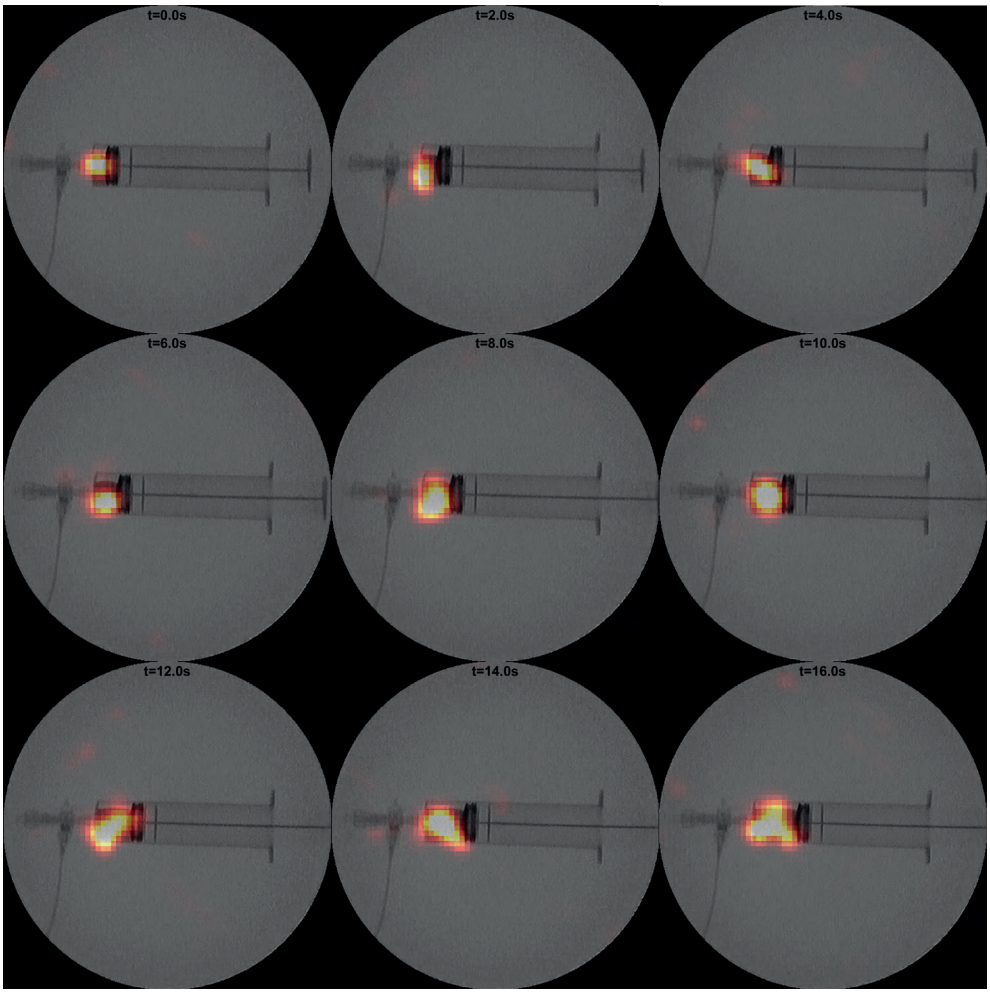

Figure 13: Montage of frames from simultaneously acquired fluoroscopic and nuclear images of a syringe filled with 41 MBq of ^{99m}Tc. Fluoroscopic images are shown in grayscale, nuclear images are shown in colour overlay.

Discussion

In hybrid fluoroscopic and nuclear imaging, collimator choice influences nuclear image quality in terms of resolution and sensitivity. Virtual projections obtained with six different collimators were simulated and compared in terms of contrast, noise and detectability. Parallel hole collimators showed higher contrast, lower noise levels and better detectability than pinhole collimators. In addition, simulations were verified with phantom measurements on the prototype system (4).

Virtual projections of a digital image quality phantom were simulated for six collimator geometries and compared with the ideal projection. For spheres smaller than 17 mm, none of the simulated collimator geometries could meet the contrast and CNR levels of the ideal projection. The ideal projection illustrates the achievable image quality without an x-ray detector obstructing the line of sight. However, the purpose of the hybrid imaging device is guiding interventional procedures rather than providing images with the highest diagnostic image quality. Slightly compromised contrast and CNR levels, as observed in the present study with parallel hole collimator geometries, may be acceptable for the aimed application.

By using parallel hole collimators, sensitivity can be improved by a factor of 7 to 22 with respect to the 5 mm pinholes of the prototype. On the other hand, collimator resolution was up to four times higher with pinholes. It is apparent from the simulations that, in terms of noise and detectability, the better counting statistics of the parallel hole collimators outweigh the superior resolution of the pinhole collimators.

The number of iterations was determined by the convergence rate of the contrast of the largest sphere. We have also investigated the noise-contrast trade-off for the different collimator geometries. This revealed that selecting the number of iterations based on noise-contrast trade-off did not lead to different results.

Besides parallel hole or pinhole collimators, usage of diverging or converging collimators might be considered. Diverging collimators share the advantage of minification with pinhole collimators, but exhibit an even lower resolution than parallel hole collimators. Converging collimators have a high sensitivity, but require an impractically large detector area to fully cover the FOV. Therefore, these collimator types are not expected to improve nuclear image quality compared with the current prototype. However, the usage of slant hole collimators with non-rotated gamma cameras might be an alternative for parallel hole collimators with rotated gamma cameras. Image quality will be comparable with parallel hole collimators, while non-rotated gamma cameras might be easier to mount on a c-arm.

Ideally, freedom of operation of the c-arm should not be hampered by the addition of gamma cameras to the system. Therefore, the gamma cameras were placed at a relatively large distance from the patient, leading to projections with low counting statistics. Count statistics could be improved by placing the gamma cameras closer to the patient or by using more gamma cameras. However, both options could obstruct the working area of the interventional radiologist and limit the mobility of the system.

Count statistics, as well as nuclear image quality, were improved by using parallel hole collimators instead of pinhole collimators. However, this would result in a less compact design, since larger gamma cameras are needed. The extra weight of the larger gamma cameras could be compensated for by a counterweight, while mobility can be guaranteed by adding a driving motor to the c-arm.

Nuclear image quality is affected by the reconstruction of the intermediate three-dimensional activity distribution. Due to the iterative nature of MLEM reconstruction, the algorithm is inherently slow. Faster construction of the virtual projection could be obtained by direct combination of the four projections in Fourier space without estimating the three-dimensional activity distribution or by performing traditional filtered backprojection (22). Results of experiments not presented in this paper indicated that both the number of projections and the angular coverage were insufficient for this type of reconstruction.

Reconstruction of the intermediate three-dimensional activity distribution from a limited number of projections and a limited angular coverage is a challenging task. Iterative algorithms based on total variation minimisation have been fairly successful for few-view CT image reconstruction (23,24) as well as for SPECT imaging (25,26). Total variation minimisation encourages piecewise constant objects, whilst preserving edges (27). Simulations, not presented in this paper, showed that total variation minimisation did not improve nuclear image quality, since noise amplitude was larger than edge contrast.

Limitations of the simulations include that no scatter and attenuation effects were modelled in the forward projector used to simulate initial projections. This has no effect on the simulations with our digital image quality phantom, since this phantom was assumed to have equal attenuation coefficients in the hot spots and in the background. However, scatter and attenuation did affect image contrast in the projections of the sphere phantom obtained with the prototype. In liver radioembolisation, gamma rays will be attenuated through a tissue layer of approximately 5 cm, reducing the number of counts by a factor of 2. This results in a higher noise level and lower contrast. Application of triple energy window scatter correction will compensate for the loss in contrast, but at the same time increases noise levels (28). Nuclear image quality as presented here for 1 s acquisition time might in clinical practice be comparable to acquisition times of 2-3 s. On the other hand, our phantom was placed at the most extreme distance from the gamma cameras, yielding a worst case scenario in terms of resolution and counts. In future research regarding simulations of clinical relevant situations, scatter and attenuation effects will be incorporated into the forward projector.

Because of the limited number of projections and the limited angular coverage, artefacts and image distortions were observed in the virtual projections. Image distortions caused the spheres to appear more to the edge of the phantom and are expected to appear in reconstructions of limited angular coverage when the iteration number is low (29). In general, increasing the number of iterations is impractical in view of increasing noise levels. The observed artefacts at the sides of the phantom in the virtual projections of parallel hole geometries are likely caused by propagation of small interpolation errors introduced during rotation of the three-dimensional activity distribution in the forward and backward projectors. Artefacts were mainly observed outside the phantom, which implies they do not influence contrast and noise levels.

In the current prototype, software and hardware were not optimised for speed. Mean reconstruction time of a single virtual projection was approximately 3 seconds. This only allows retrospective construction of the virtual projection. Parallel processing on graphical processing units can substantially accelerate reconstruction times (30). Therefore, real-time processing appears feasible when software and hardware are optimised for speed.

In the present simulation study, matched projectors were used for the generation of projections and reconstruction of the three-dimensional activity distribution. This represents the ideal situation, in which the true system matrix is known. In practice, the true system matrix is unknown, which might lead to nuclear images of lower quality than presented here. However, noise was added to the projections, thus avoiding a truly matched system. Although the projectors were still matched, noise is dominant in the simulations due to the short acquisition times. Therefore, we believe that the noisy projections differ enough from the original projection to allow the use of matched projectors. In addition, the effect of (un)matched projectors was investigated by simulations with Monte Carlo generated projections. These Monte Carlo simulations differed significantly from the basic projector in the reconstruction by including more detailed collimator modelling and attenuation and scatter effects. Still, this resulted in comparable values for contrast and noise as compared with simulations using the basic projector. We expect that potential differences may be minimised by calibrating the system (31). Moreover, these errors will likely affect parallel hole and pinhole collimators similarly, so that the conclusions of this study remain valid.

Conclusion

In hybrid fluoroscopic and nuclear imaging, collimator choice influences nuclear image quality in terms of resolution and sensitivity. Image quality of nuclear images obtained with six different collimators were compared with the current prototype and the ideal projection by means of simulations. Parallel hole collimators showed lower noise and better detectability than pinhole collimators. Of the parallel hole collimators, the LEUHR collimator showed the best spatial resolution, with comparable values for contrast, noise and detectability. Simulations were verified in terms of contrast and noise level by hybrid imaging of a phantom.

References

1. A Bockisch, LS Freudenberg, D Schmidt, and T Kuwert, Hybrid Imaging by SPECT/CT and PET/CT: Proven Outcomes in Cancer Imaging, Semin. Nucl. Med., 2009, 39(4):276–89.
2. JA Patton, DW Townsend, and BF Hutton, Hybrid Imaging Technology: From Dreams and Vision to Clinical Devices, Semin. Nucl. Med., 2009, 39(4):247–63.
3. PB Shyn, Interventional positron emission tomography/computed tomography: State-of-the-art, Tech. Vasc. Interv. Radiol., 2013, 16(3):182–90.
4. C Beijst, M Elschot, MA Viergever, and HWAM de Jong, Toward Simultaneous Real-Time Fluoroscopic and Nuclear Imaging in the Intervention Room, Radiology, 2016, 278(1):232–8.
5. S Vidal-Sicart, ME Rioja, P Paredes, MR Keshtgar, and RA Valdés Olmos, Contribution of perioperative imaging to radioguided surgery, Q. J. Nucl. Med. Mol. imaging, 2014, 58(2):140–60.
6. AJAT Braat, MLJ Smits, MNGJA Braat, AF van den Hoven, JF Prince, HWAM de Jong, et al., ^{90}Y Hepatic Radioembolization: An Update on Current Practice and Recent Developments, J. Nucl. Med., 2015, 56(7):1079–87.
7. WY Lau, TWT Leung, S Ho, M Chan, NWY Leung, J Lin, et al., Diagnostic pharmaco-scintigraphy with hepatic intra arterial technetium-99m macroaggregated albumin in the determination of tumour to non-tumour uptake ratio in hepatocellular carcinoma, Br. J. Radiol., 1994, 67(794):136–9.
8. SR Cherry, JA Sorenson, and ME Phelps, Physics in Nuclear Medicine - The Gamma Camera, Fourth edi. Elsevier; 2012.
9. Y Mao, Z Yu, and GL Zeng, Segmented slant hole collimator for stationary cardiac SPECT: Monte Carlo simulations, Med. Phys., 2015, 42(9):5426–34.
10. A Perkins, C Stearns, J Chapman, J Kolthammer, JJ Williams, and M Casey, NEMA Standards Publication NU 2-2007: Performance measurements of positron emission tomographs, Rosslyn USA Natl. Electr. Manuf. Assoc., 2007.
11. KP Willowson, M Tapner, and DL Bailey, A multicentre comparison of quantitative ^{90}Y PET/CT for dosimetric purposes after radioembolization with resin microspheres, Eur. J. Nucl. Med. Mol. Imaging, 2015, 42(8):1202–22.
12. EVR Di Bella, AB Barclay, RL Eisner, and RW Schafer, A comparison of rotation-based methods for iterative reconstruction algorithms, IEEE Trans. Nucl. Sci., 1996, 43(6):3370–6.
13. Siemens Healthineers, Symbia S and T System Specifications, 2010.
14. LA Shepp, and Y Vardi, Maximum Likelihood Reconstruction for Emission Tomography, IEEE Trans. Med. Imaging, 1982, 1(2):113–22.
15. HWAM de Jong, ETP Slijpen, and FJ Beekman, Acceleration of Monte Carlo SPECT simulation using convolution-based forced detection, IEEE Trans. Nucl. Sci., 2001, 48(1):58–64.
16. K Barrett, H Brooks, S Boitano, and S Barman, Ganong's review of medical physiology, 2010.
17. TR Miller, and JW Wallis, Clinically important characteristics of maximum-likelihood reconstruction, J. Nucl. Med., 1992, 33(9):1678–84.

18. A Rose, The Sensitivity Performance of the Human Eye on an Absolute Scale, J. Opt. Soc. Am., 1948, 38(2):196.
19. FJ Beekman, HWAM De Jong, and S Van Geloven, Efficient fully 3-D iterative SPECT reconstruction with Monte Carlo-based scatter compensation, IEEE Trans. Med. Imaging, 2002, 21(8):867–77.
20. J Xiao, TC de Wit, SG Staelens, and FJ Beekman, Evaluation of 3D Monte Carlo-based scatter correction for ^{99m}Tc cardiac perfusion SPECT, J. Nucl. Med., 2006, 47(10):1662–9.
21. RG Gould, A video frame-averaging digital fluoroscopic system, Appl. Radiol., 1982, 11(6):83–4.
22. PE Carlsson, 3D Fourier synthesis of a new X-ray picture identical in projection to a previous picture, 1993.
23. EY Sidky, C-M Kao, and X Pan, Accurate image reconstruction from few-views and limited-angle data in divergent-beam CT, J. Xray. Sci. Technol., 2009, 14(2):119–39.
24. J Velikina, S Leng, and G-H Chen, Limited view angle tomographic image reconstruction via total variation minimization, J. Chem. Inf. Model., 2007, 53(9):651020.
25. VY Panin, GL Zeng, and GT Gullberg, Total variation regulated EM algorithm, IEEE Trans. Nucl. Sci., 1999, 46(6):2202–10.
26. M Persson, D Bone, and H Elmqvist, Three-dimensional total variation norm for SPECT reconstruction, Nucl. Instruments Methods Phys. Res., 2001, 471(1–2):98–102.
27. GL Zeng, On few-view tomography and staircase artifacts, IEEE Trans. Nucl. Sci., 2015, 62(3):851–8.
28. K Perisinakis, N Karkavitsas, J Damilakis, and N Gourtsoyiannis, Effect of dual and triple energy window scatter correction methods on image quality in liver scintigraphy, Nuklearmedizin, 1998, 37(7):239–44.
29. GL Zeng, Comparison of FBP and iterative algorithms with non-uniform angular sampling, IEEE Nucl. Sci. Symp. Med. Imaging Conf., 2014, 100(2):1–13.
30. A Eklund, P Dufort, D Forsberg, and SM LaConte, Medical image processing on the GPU – Past, present and future, Med. Image Anal., 2013, 17(8):1073–94.
31. C Beijst, M Elschot, S van der Velden, and HWAM de Jong, Multimodality calibration for simultaneous fluoroscopic and nuclear imaging, EJNMMI Phys., 2016, 3(1):20.

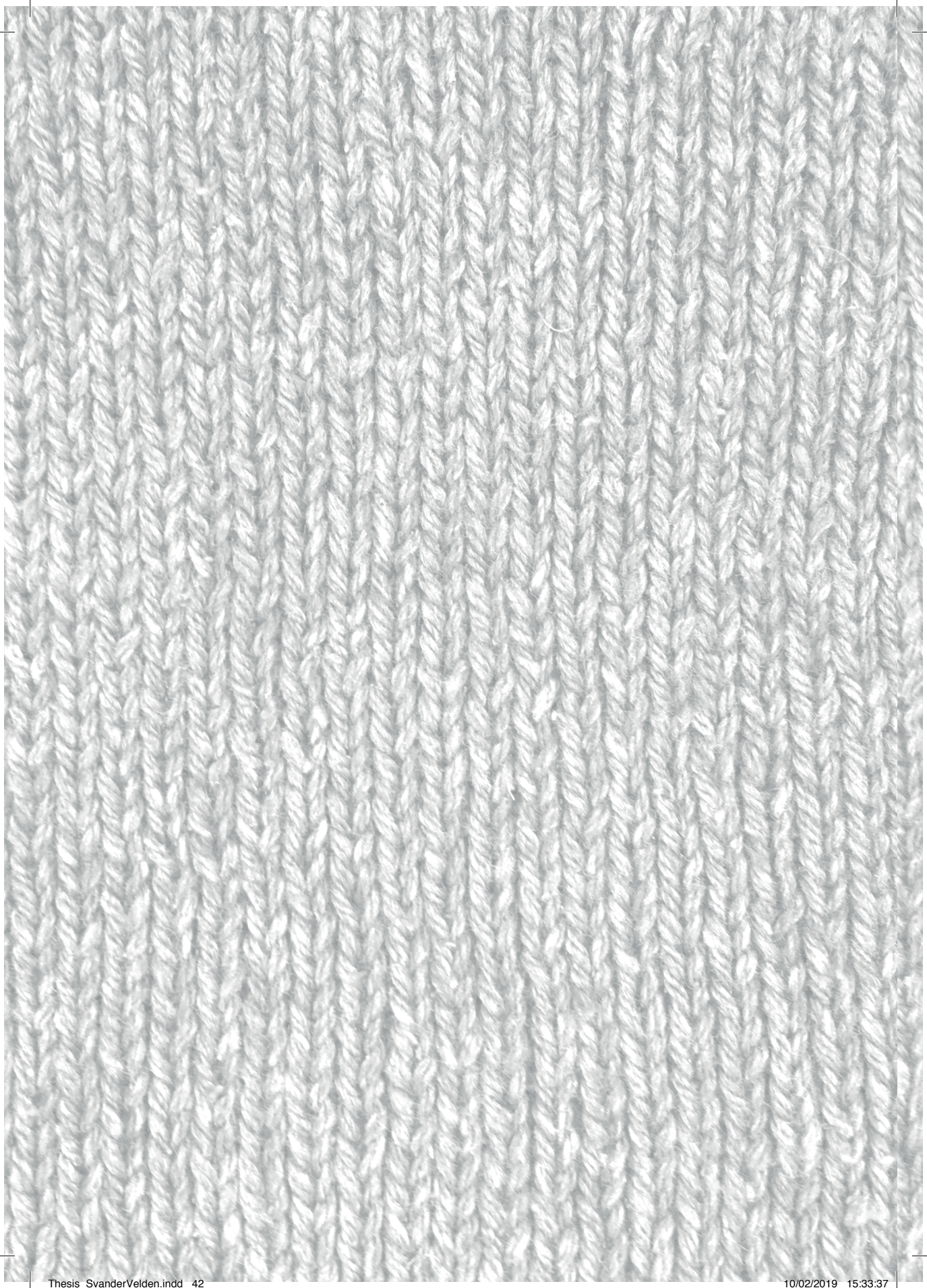

3

A dual layer detector for simultaneous fluoroscopic and nuclear imaging

Based on:

S. van der Velden*, B. Kunnen*, W.J.C. Koppert, J.H.L Steenbergen, M.M.A. Dietze, C. Beijst, M.A. Viergever, M.G.E.H. Lam, H.W.A.M. de Jong, "A dual-layer detector for simultaneous fluoroscopic and nuclear imaging", Radiology, 2019

***Authors contributed equally**

Abstract

Purpose

To develop and evaluate a dual layer detector capable of acquiring intrinsically registered fluoroscopic and nuclear images in the intervention room.

Materials and methods

The dual layer detector consists of an x-ray flat panel detector placed in front of a gamma camera with cone beam collimator focussed at the x-ray focal spot. This design relies on the x-ray detector absorbing the majority of the x-rays, while being more transparent to the higher energy gamma photons. A prototype was built and dynamic phantom images were acquired. In addition, spatial resolution and system sensitivity (evaluated as counts detected within the energy window per second per MBq) were measured with the prototype. Monte Carlo simulations for an improved system with varying flat panel compositions were performed to assess potential spatial resolution and system sensitivity.

Results

Experiments with the dual layer detector prototype showed that spatial resolution of the nuclear images was unaffected by the addition of the flat panel (full width at half maximum: 13.6 mm at 15 cm from the collimator surface). However, addition of the flat panel lowered system sensitivity by 45% to 60%, owing to the non-optimised transmission of the flat panel. Simulations showed that an attenuation of 27% to 35% of the gamma rays in the flat panel could be achieved by decreasing the crystal thickness and housing attenuation of the flat panel.

Conclusion

The proposed dual layer detector was found capable of acquiring real-time intrinsically registered hybrid images, which could aid interventional procedures involving radionuclides.

Introduction

Hybrid imaging modalities are of great importance for oncological imaging because they combine anatomical and nuclear information. However, the use of hybrid imaging modalities (e.g. single photon emission computed tomography/computed tomography (SPECT/CT)) in the intervention room is limited due to the bulky design of these modalities (1). In addition, sequential hybrid imaging is suboptimal owing to the dynamic nature of interventions. Interventional nuclear imaging is performed with gamma probes or hand-held gamma cameras, providing real-time feedback about the activity distribution, but interpretation of this information can be difficult for lack of co-registered anatomical information. Therefore, we aim at developing a real-time, simultaneous fluoroscopic and nuclear imaging device, consisting of a c-arm with nuclear imaging capabilities.

In our previous design (2,3), four gamma cameras with pinhole collimators were positioned at the side of the x-ray tube. Although the prototype showed that interventional hybrid imaging was feasible, this design requires an intermediate reconstruction step and additional weight added to the already heavy x-ray tube. Also, it has a lower spatial resolution of the nuclear image close to the x-ray detector. Instead, we propose a dual layer detector that does not require an intermediate reconstruction step, has better nuclear image resolution and has a better weight balance between x-ray source and detector.

The goal of this study was to develop and evaluate a dual layer detector capable of acquiring intrinsically registered fluoroscopic and nuclear images in the intervention room in real-time, which may guide interventional procedures involving radionuclides such as radioembolisation.

Materials and methods

Geometry

The dual layer detector consists of a gamma camera with cone beam collimator placed behind a dynamic x-ray flat panel (Figure 1a). The cone beam collimator focusses on the focal spot of the x-ray tube, resulting in intrinsically registered x-ray and nuclear images (Figure 1b). The x-ray flat panel absorbs the majority of the x-rays (30-120 keV), but is more transparent to the higher energy (140 keV) gamma rays, which allows simultaneous detection.

An experimental prototype of the dual layer detector was built (Figure 2). The gamma imaging part of the prototype consisted of a Diacam gamma camera (Siemens Healthcare, Erlangen, Germany) mounted with a low-energy cone beam collimator (septal thickness: 0.25 mm; hole diameter: 1.90 mm; hole length: 40 mm; focal distance: 98 cm) (Nuclear Fields, Vortum-Mullem, the Netherlands) (4). The gamma camera had a 9.5 mm NaI(Tl) scintillation crystal and a field of view (FOV) of 53.3 x 38.7 cm. The intrinsic resolution of the gamma camera was 10 mm full width at half maximum (FWHM) as measured with a collimated point source without collimator.

The x-ray imaging part consisted of an x-ray tube of a Veradius c-arm (Philips Healthcare, Best, the Netherlands) and a commercially available Pixium® 3040 flat panel (Trixell, Moirans, France) (5). The x-ray flat panel had a 750 µm CsI(Tl) detection layer, 154 µm pixel pitch, a FOV of 29.6 x 38.2 cm and a total thickness of 7.5 cm. The flat panel was first modified by Philips

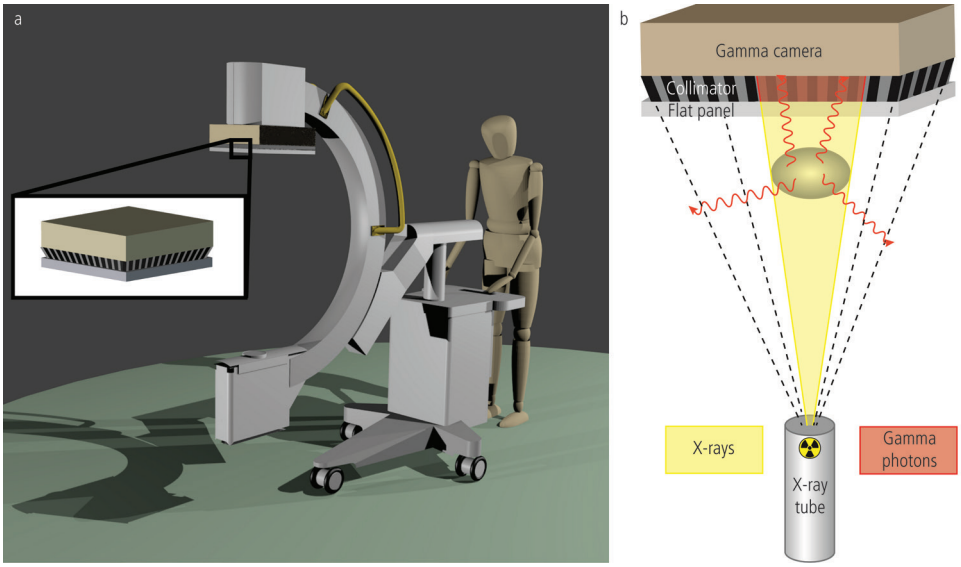

Figure 1: (a) Rendering of a mobile c-arm with the proposed dual layer detector, consisting of a gamma camera, cone beam collimator and x-ray flat panel. (b) Schematic overview of the principle of simultaneous detection of nuclear and x-ray images.

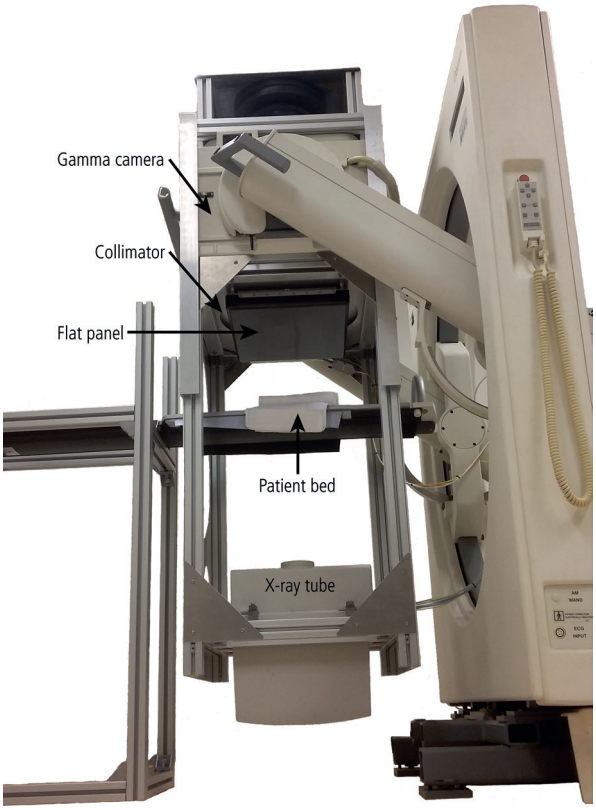

Figure 2: Prototype setup, consisting of a gamma camera with cone beam collimator (focus at 98 cm), modified flat panel and x-ray tube.

Healthcare to improve the transmission of gamma rays over the original detector by removing the lead shielding and some excess aluminium at the backside of the assembly.

Phantom experiments

To illustrate potential applications of the dual layer detector, two phantom experiments were performed where dynamic nuclear and fluoroscopic images were acquired simultaneously. In the first experiment, a cobalt-57 (^{57}Co) pen marker of 8.4 MBq was moved within the thorax of the RS-800 phantom (Radiological Support Devices, Long Beach, USA). The thorax was filled with air and the heart, liver and lungs were removed while all bone structures of the thorax were present.

In the second experiment, a liver-shaped phantom containing a 40 mm diameter sphere representing a liver tumour was positioned on a translating stage to simulate breathing motion (amplitude: 2 cm, period: 5 s). The sphere was filled with 16 MBq of technetium-99m (^{99m}Tc) and the background compartment was filled with 83 MBq of ^{99m}Tc, resulting in a 10:1 concentration ratio, representing a ^{99m}Tc-labelled macroaggregated albumin (^{99m}Tc-MAA) procedure preceding yttrium-90 radioembolisation (10).

For both phantom experiments, dynamic nuclear data was acquired in list-mode with a 15% wide energy window centred at the photopeak. Every 250 ms, list-mode data of the prior 500 ms was binned into image frames visualised at a frame rate of 4 Hz. List-mode data acquired during and shortly after the x-ray pulses was left out (21 ms per x-ray pulse) (Figure 3). Nuclear images (2 x 2 mm pixel size) were corrected for non-uniformities with a flood map and were post-filtered with a 24 mm FWHM Gaussian filter. Fluoroscopic images were acquired at 51 kVp and 0.515 mA (first phantom experiment) and at 52 kVp and 0.555 mA (second phantom experiment) with automatic exposure control, both at a frame rate of 4 Hz, in alignment with the 4 Hz nuclear images. Registration of the fluoroscopic image with the nuclear image was achieved by applying a rigid transformation (rotation, translation, magnification) calculated from three ^{57}Co pen marker measurements.

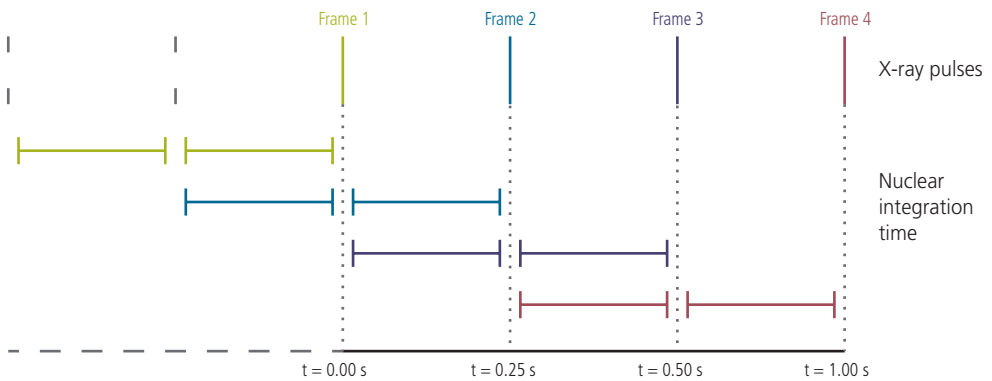

Figure 3: Schematic overview of hybrid data acquisition scheme. Every 250 ms, list-mode data of the prior 500 ms was binned into image frames which were visualised at a frame rate of 4 Hz. List-mode data acquired during and shortly after the x-ray pulses was left out (21 ms per x-ray pulse).

Nuclear image quality

To assess nuclear image quality, static measurements were performed using a ^{99m}Tc point source of 4 MBq positioned at varying distances (range 11.5 – 37.5 cm) from the collimator surface with 60 s acquisition time with and without flat panel in place, to study the influence of the flat panel on nuclear image quality and system sensitivity. Counts were acquired in a 15% energy window centred at 140 keV. Pixel size was 2 x 2 mm. Spatial resolution was defined as the FWHM of the point spread function. System sensitivity was expressed in counts per second (CPS)/MBq being detected within the energy window. In addition, system sensitivity was measured using a 200 MBq ^{99m}Tc flood source of 53 x 40 cm.

Simulations

First, the prototype system was simulated using MCNP6 1.0 (7). Since the exact composition of the flat panel was confidential and therefore not disclosed by the manufacturer, the flat panel was modelled as 750 µm CsI, 700 µm Si (read-out layer) and 26 mm Al to match the system sensitivity of the prototype system. The total thickness of the modelled flat panel was identical to the prototype flat panel (75 mm, with the remaining 47.5 mm modelled as air).

Based on this model, improved systems were simulated by (a) reducing the amount of Al to 7 mm, (b) reducing the flat panel thickness to 10 mm (thin flat panel), (c) varying the CsI thickness (range 0.3 – 0.75 mm) and (d) simulating an intrinsic spatial resolution of the gamma camera of 3 mm FWHM.

For all combinations of source-collimator distance and flat panel compositions, a seperate simulation was run with 100 million photons, representing a point source of 1.7 MBq ^{99m}Tc with an acquisition time of 60 seconds. The point source was positioned at varying distances from the collimator surface (range 5 - 31 cm). The energy resolution was simulated as 10%. The intrinsic resolution of the setup with thin flat panels was simulated as 3 mm FWHM and the intrinsic resolution of the prototype setup (thick flat panel) was simulated as 10 mm FWHM. Pixel size was 2 x 2 mm.

Results

Phantom experiments

Figure 4 and 5 show single frame images of the real-time, simultaneously acquired hybrid video of both phantoms, with the x-ray image in grayscale and the nuclear image in colour overlay. Visual inspection of the images showed that good spatial overlap was obtained and no artefacts were visible in either the x-ray or nuclear images. This shows that the presence of the radioactive tracer had no influence on the quality of the x-ray image. In addition, nuclear images could be acquired with short frame durations, despite the attenuation and scatter of gamma rays by the flat panel.

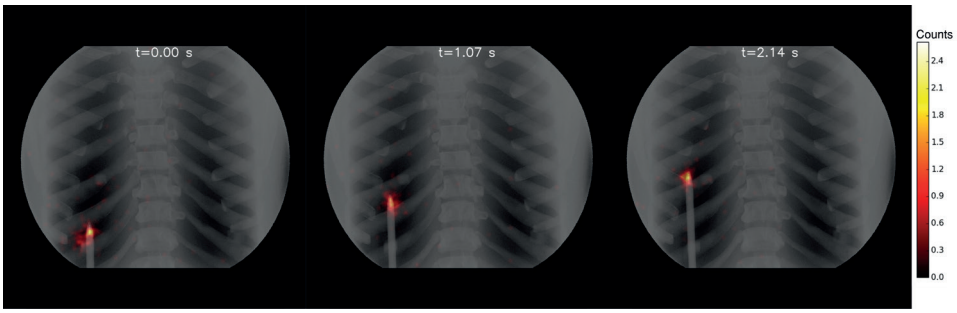

Figure 4: Single frame images (Δt = 1.07 s) of the video of a cobalt-57 pen marker moving inside the thorax of the RS-800 phantom. X-ray images are shown in grayscale, nuclear images are shown in colour overlay, scaled between zero and the maximum number of counts.

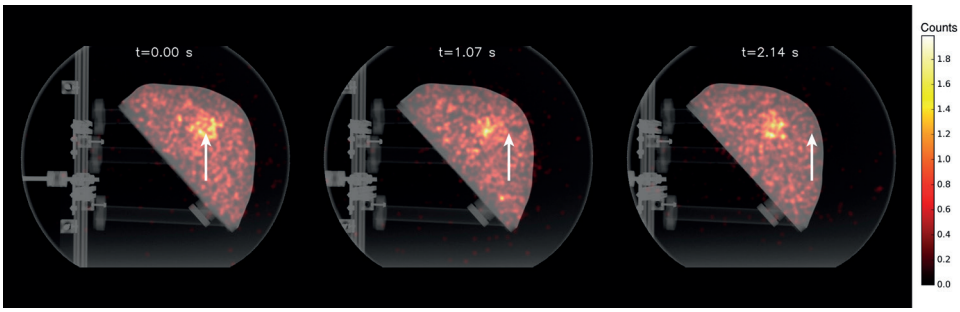

Figure 5: Single frame images (Δt = 1.07 s) of the video of the moving liver-shaped phantom acquired with the prototype setup. X-ray images are shown in grayscale, nuclear images are shown in colour overlay, scaled between zero and the maximum number of counts. The white arrow indicates the position of the hot sphere in the first frame (t = 0.00 s).

Image quality

Figure 6ab shows the measured system sensitivity and spatial resolution of the prototype, with and without flat panel, and the simulations of the prototype system with flat panel. The simulations were in agreement with the measurements of the prototype (difference in system sensitivity and spatial resolution less than 14% and 9%, respectively). For the point source, measured at the centre of the camera, incorporating the flat panel into the setup reduced the system sensitivity by 60%. Reduction was 45% when measured with the flood source. The difference in measured system sensitivity represents the inhomogeneity of the flat panel. Spatial resolution was unaffected by addition of the flat panel (difference less than 7%).

Figure 6cd shows the simulated system sensitivity and spatial resolution of the improved systems. Incorporating a thin flat panel into the setup reduced the system sensitivity by 27% - 35%, depending on the CsI crystal thickness. Improving the intrinsic resolution of the gamma camera did not influence the system sensitivity. Spatial resolution was unaffected (difference less than 2%) by reducing the thickness of the flat panel or varying CsI thickness. However, a thinner flat panel allowed smaller source-collimator distances, which improved the spatial resolution. Improving the intrinsic resolution of the gamma camera also improved the spatial resolution of the system.

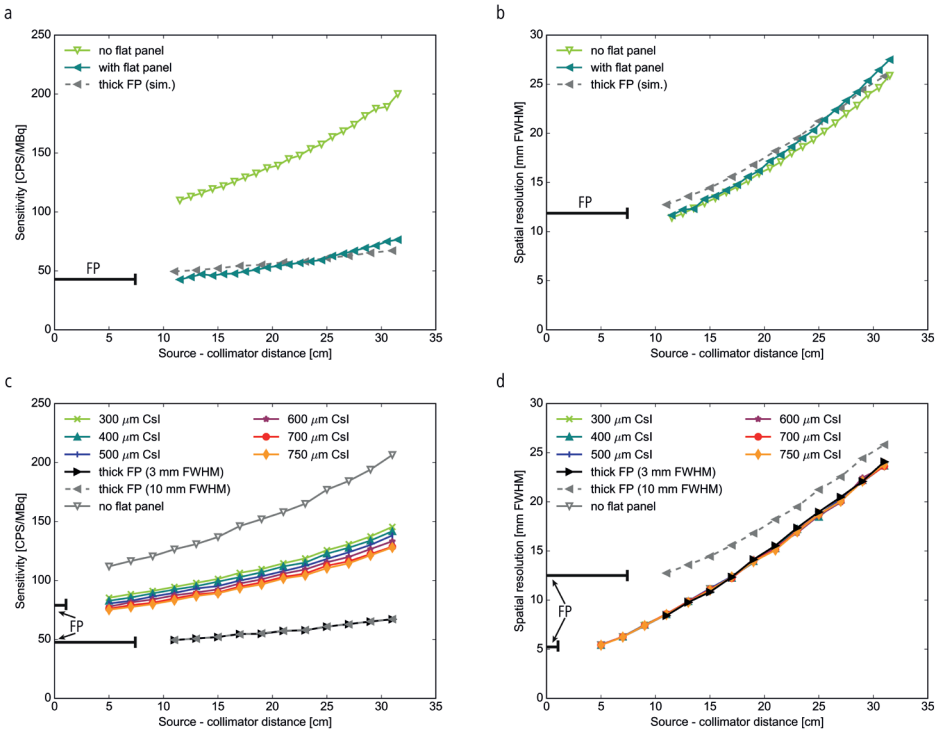

Figure 6: (a) Measured and simulated system sensitivity and (b) spatial resolution of the prototype system. The simulated thick flat panel was modelled to match these measurements. (c) Simulated system sensitivity and (d) simulated spatial resolution for the current thick flat panel and the modelled thin flat panels. In all figures, the thickness of the flat panel is indicated by the horizontal black line. (sim.: simulated, CPS: counts per second, CsI: cesium iodide, FP: flat panel, FWHM: full width at half maximum)

Discussion

Interventional procedures could potentially benefit from real-time intrinsically registered hybrid images for improved localisation and treatment guidance. Simulations and measurements with the prototype system demonstrated that a dual layer detector, consisting of a gamma camera with cone beam collimator and x-ray flat panel, was capable of acquiring such hybrid images. Addition of the flat panel did not affect spatial resolution of the nuclear image, system sensitivity decreased by 45% to 60%.

Availability of hybrid images would potentially benefit multiple procedures, such as sentinel node procedures, biopsies and radioembolisation procedures. For radioembolisation procedures, the main advantage is that patients will not have to be transferred to the nuclear medicine department for assessment of the pre-treatment procedure with ^{99m}Tc-MAA. This would make the procedure more time efficient and would allow for single-session radioembolisation procedures (8,9). In a single-session procedure, the vascular sheath is not removed, in contrast to the standard procedure, ensuring equal injection position for ^{99m}Tc-MAA and microspheres. When nuclear images can be acquired in the intervention room, movement of the vascular sheath is limited

because the patient does not have to change beds for assessment of the ^{99m}Tc-MAA distribution. This improves the prognostic power of the pre-treatment procedure (10). However, in principle, any procedure using radionuclides and x-ray imaging could benefit from our dual layer detector.

Transmission of gamma rays through the flat panel can be substantially improved by reducing the amount of aluminium surrounding the flat panel. In addition, repositioning the read-out electronics would improve homogeneity of the gamma ray transmission. The position of some large electronic components explains the difference in system sensitivity when measured with a point source compared to a flood source (60% and 45% reduced system sensitivity, respectively).

Modifications to our prototype flat panel only affected the housing and therefore did not influence its imaging properties, so from the x-ray point of view every fluoroscopic setting can be used. However, from a nuclear point of view, the current prototype allows the use of 40-80 kVp tube voltages, depending on the tube current. For our phantom experiments, x-ray images were acquired at ~50 kVp, since the phantoms were small and did not require high tube voltages. In clinical practice, higher tube voltages are used. Although higher tube voltages cause more photons to penetrate the x-ray detector and create interactions in the gamma camera, we believe that this effect can be mitigated by modification of the PMT circuitry, and/or the addition of a high pass filter, and/or by performing interleaved measurements (required when tube voltage approaches photopeak energy) (11). Such interleaved measurements were used for the acquisition of the phantom images and assumed in our simulations, obviating the need for simulation of the x-ray pulses.

A limitation of our proposed detector is the reduced system sensitivity of the gamma camera due to the attenuation in the flat panel and the short frame duration required for real-time imaging. Although these factors will negatively influence nuclear image quality in terms of contrast and noise, the aim of our system is not to provide the physician with images of the highest diagnostic quality. In interventional procedures, the diminished nuclear image quality may be compensated by providing additional information that is otherwise not available. Also, image quality may be improved by image processing, exploiting the dynamic nature of the image data by frame averaging, as is commonly done in fluoroscopy.

In a more mature setup, we plan to redesign the aluminium housing of the flat panel and reposition the read-out electronics. This will result in the transmission of more gamma photons through the flat panel. The final design of our setup will be a trade-off between nuclear and fluoroscopic image quality. With regard to flat panel composition, a thicker CsI layer would lead to both better fluoroscopic dose efficiency and a lower sensitivity for gamma photons. The required CsI thickness will be further investigated in future research.

Conclusion

We have demonstrated the feasibility of acquiring real-time and intrinsically registered fluoroscopic and nuclear images of the same FOV, by means of a dual layer detector. Such hybrid images may be used advantageously in interventional procedures involving radionuclides, such as radioembolisation.

References

1. PB Shyn, Interventional positron emission tomography/computed tomography: State-of-the-art, Tech. Vasc. Interv. Radiol., 2013, 16(3):182–90.
2. C Beijst, M Elschot, MA Viergever, and HWAM de Jong, Toward Simultaneous Real-Time Fluoroscopic and Nuclear Imaging in the Intervention Room, Radiology, 2016, 278(1):232–8.
3. S van der Velden, C Beijst, MA Viergever, and HWAM de Jong, Simultaneous fluoroscopic and nuclear imaging: impact of collimator choice on nuclear image quality, Med. Phys., 2017, 44(1):249–61.
4. RJ Jaszczak, KL Greer, and RE Coleman, SPECT using a specially designed cone beam collimator, J. Nucl. Med., 1988, 29(8):1398–405.
5. T Ducourant, T Wirth, G Bacher, B Bosset, J-M Vignolle, D Blanchon, et al., Latest advancements in state-of-the-art aSi-based x-ray flat panel detectors, Medical Imaging 2018: Physics of Medical Imaging. SPIE; 2018, page 217.
6. F Giammarile, L Bodei, C Chiesa, G Flux, F Forrer, F Kraeber-Bodere, et al., EANM procedure guideline for the treatment of liver cancer and liver metastases with intra-arterial radioactive compounds, Eur. J. Nucl. Med. Mol. Imaging, 2011, 38(7):1393–406.
7. T Goorley, M James, T Booth, F Brown, J Bull, LJ Cox, et al., Initial MCNP6 release overview, Nucl. Techn., 2012, 180(3):298–315.
8. A Gabr, JR Kallini, VL Gates, R Hickey, L Kulik, K Desai, et al., Same-day ^{90}Y radioembolization: implementing a new treatment paradigm, Eur. J. Nucl. Med. Mol. Imaging, 2016, 43(13):2353–9.
9. VL Gates, KG Marshall, K Salzig, M Williams, RJ Lewandowski, and R Salem, Outpatient Single-Session Yttrium-90 Glass Microsphere Radioembolization, J. Vasc. Interv. Radiol., 2014, 25(2):266–70.
10. E Garin, J Edeline, and Y Rolland, High Impact of Preferential Flow on ^{99m}Tc-MAA and ^{90}Y-Loaded Microsphere Uptake Correlation, J. Nucl. Med., 2016, 57(11):1829–30.
11. WJC Koppert, S van der Velden, JHL Steenbergen, and HWAM de Jong, Impact of intense x-ray pulses on a NaI(Tl)-based gamma camera, Phys. Med. Biol., 2018, 63(6):065006.

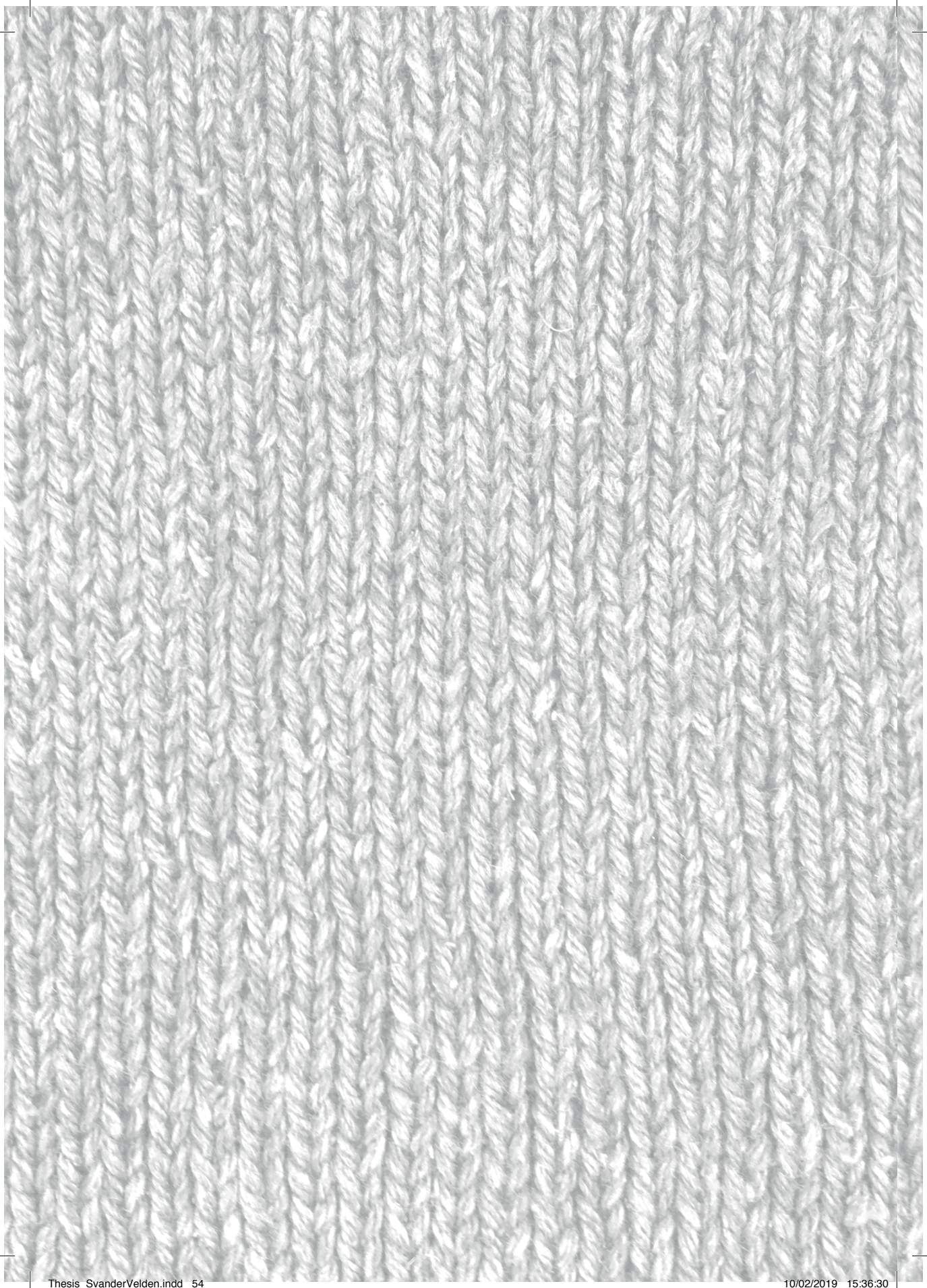

4

Estimation of lung shunt fraction from simultaneous fluoroscopic and nuclear images

Based on:

S. van der Velden, R. Bastiaannet, A.J.A.T. Braat, M.G.E.H. Lam, M.A. Viergever, H.W.A.M. de Jong, "Estimation of lung shunt fraction from simultaneous fluoroscopic and nuclear images", Physics in Medicine & Biology, 2017, nr. 21, vol. 62, pp. 8210-8225

Abstract

Purpose

Radioembolisation with yttrium-90 (^{90}Y) is increasingly used as a treatment of unresectable liver malignancies. For safety, a scout dose of technetium-99m macroaggregated albumin (^{99m}Tc-MAA) is used prior to the delivery of the therapeutic activity to mimic the deposition of ^{90}Y. Single-session procedures are currently limited by the lack of nuclear images in the intervention room. To cope with this limitation, an interventional simultaneous fluoroscopic and nuclear imaging device is currently being developed. The purpose of this simulation study was to evaluate the accuracy of estimating the lung shunt fraction (LSF) of the scout dose in the intervention room with this device and compare it against current clinical methods.

Materials and methods

A male and female XCAT phantom, both with two respiratory profiles, were used to simulate various LSFs resulting from a scout dose of 150 MBq ^{99m}Tc-MAA. Hybrid images were Monte Carlo simulated for breath-hold (5 s) and dynamic breathing (10 frames of 0.5 s) acquisitions. Nuclear images were corrected for attenuation with the fluoroscopic image and for organ overlap effects using a pre-treatment CT scan. For comparison purposes, planar scintigraphy and mobile gamma camera images (both 300 s acquisition time) were simulated. Estimated LSFs were evaluated for all methods and compared to the phantom ground truth.

Results

In the clinically relevant range of 10-20% LSF, hybrid imaging overestimated LSF with approximately 2 percentage points (pp) and 3 pp for the normal and irregular breathing phantoms, respectively. After organ overlap correction, LSF was estimated with a more constant error. Errors in planar scintigraphy and mobile gamma camera imaging were more dependent on LSF, body shape and breathing profile.

Conclusion

LSF can be estimated with a constant minor error with our hybrid imaging device. Estimated LSF was highly dependent on true LSF, body shape and breathing pattern when estimated with current clinical methods. The hybrid imaging device was capable of accurately estimating LSF within a few seconds in an interventional setting.

Introduction

Radioembolisation with yttrium-90 (^{90}Y) microspheres is increasingly used as a treatment of unresectable liver malignancies (1–3). Microspheres loaded with ^{90}Y are injected into the hepatic artery. After injection, the microspheres lodge in the microvasculature of the tumour, delivering locally high absorbed doses of radiation whilst sparing the healthy liver parenchyma (2).

Before the therapeutic microspheres are administered to the patient, treatment is simulated with a scout dose of technetium-99m macroaggregated albumin (^{99m}Tc-MAA (LyoMAA, Mallinckrodt Pharmaceuticals)) to ensure a safe procedure. ^{99m}Tc-MAA particles are supposed to mimic the distribution of ^{90}Y microspheres (2,4). With planar scintigraphy or single photon emission computed tomography (SPECT), the portions of microspheres shunting to the lungs and the gastrointestinal tract, both of which can cause serious complications, can be assessed (5–7). The administered activity is lowered at a lung shunt fraction (LSF) between 10% and 20% when using ^{90}Y resin microspheres, and treatment is abandoned at an LSF of 20% or more (8). For ^{90}Y glass and holmium-166 (^{166}Ho) microspheres, administered activity is limited to an estimated lung dose of less than 30 Gy based on the LSF estimation of the scout dose on planar imaging. This makes accurate estimation of the LSF of paramount importance. However, the accuracy of estimating lung shunt fraction with planar scintigraphy is suggested to be deteriorated by breathing, attenuation and organ overlap effects (9,10).

In clinical practice, potential shunting to the lungs is the primary reason for ^{99m}Tc-MAA scintigraphy, generally performed one to two weeks prior to actual treatment (2,11). It has been suggested, however, to switch to a single-session procedure, in which the scout dose procedure and the treatment procedure are sequentially performed (12,13). This requires the patient to be transferred from the intervention room to the nuclear medicine department in between, which lengthens the overall time of the procedure. Total procedure times would shorten considerably when the distribution of the scout dose could be assessed in the intervention room directly after administration.

To this end, a real-time, simultaneous fluoroscopic and nuclear imaging device is currently being developed by our group, consisting of a c-arm combined with four gamma cameras (Figure 1) (14,15). This set-up enables simultaneous acquisition of fluoroscopic and nuclear images of the same field of view (FOV), thereby creating overlapping hybrid images in both the spatial and the temporal domain. The hybrid images provide a quick insight into the radionuclide distribution during the procedure, which might obviate imaging at the nuclear medicine department. In addition, estimating LSF with this hybrid imaging device may overcome the drawbacks related to planar scintigraphy, since the fluoroscopic image provides extra information regarding attenuation and patient position. The possibility of using the same catheter position during scout and treatment dose administration also strengthens the reliability of the LSF estimation (16). The purpose of this simulation study was to evaluate the accuracy of LSF estimations with our hybrid imaging device in the intervention room. In addition, a comparison was made with the current clinical standard to investigate the potential of safely replacing planar scintigraphy with hybrid imaging in the intervention room.

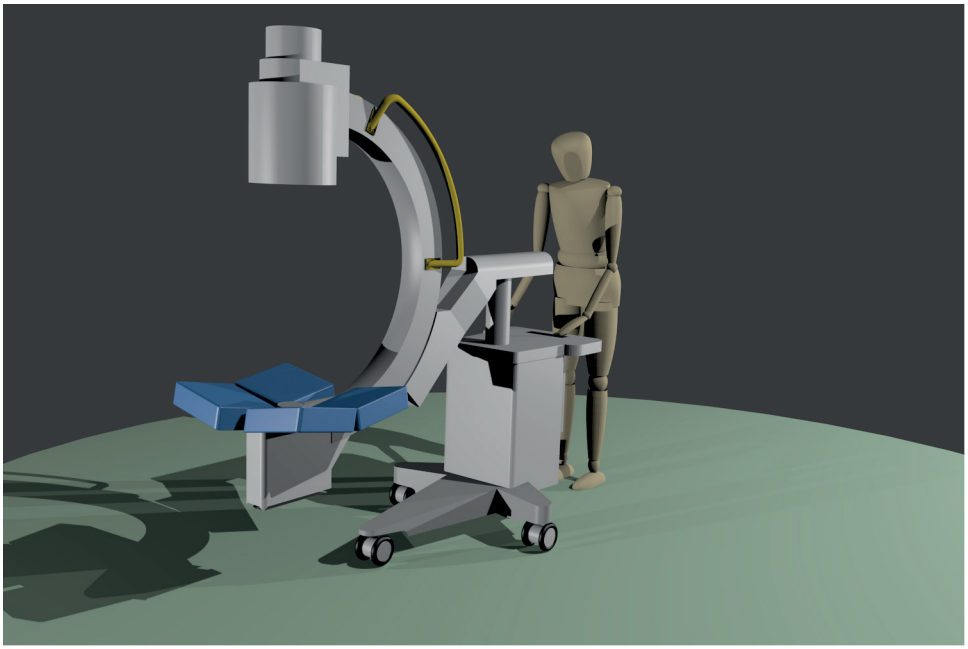

Figure 1: Rendering of the simultaneous fluoroscopic and nuclear imaging device. Four gamma cameras with parallel hole collimators, indicated in blue, are positioned around the x-ray tube. Projections of these gamma cameras are converted into a projection matching the projection geometry of the fluoroscopic image at the position of the image intensifier.

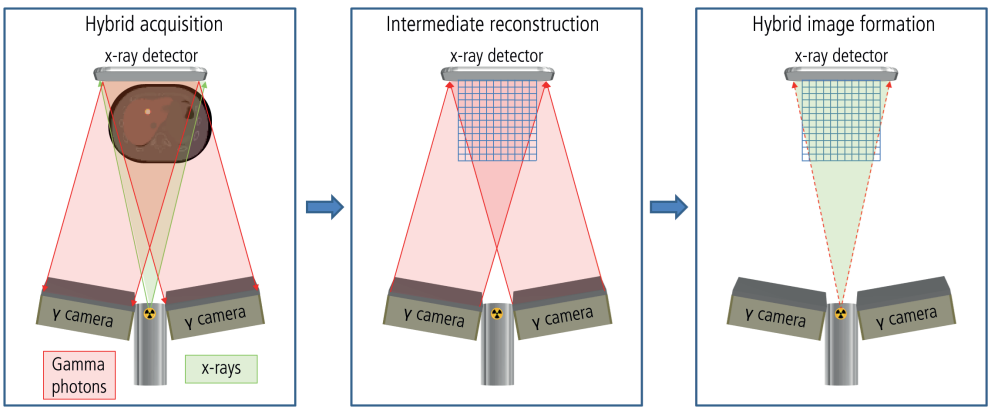

Figure 2: Flow chart showing hybrid image formation from four emission projections and one fluoroscopic projection.

Materials and methods

Device design

Our hybrid imaging device is extensively described and evaluated for physical performance earlier (14,15), including the hardware and algorithms that are applied to generate a real-time, simultaneous hybrid planar image. In short, four gamma cameras are symmetrically placed around the x-ray tube, hence creating stereoscopic views of the FOV without blocking the line of sight of the x-ray modality (Figure 1) (14). The four projections are converted into a projection that overlaps with the x-ray image using two steps (Figure 2). In the first step, an intermediate three-dimensional image is reconstructed from the four projections. Secondly, the activity distribution is projected onto the x-ray detector according to the projection geometry of the x-rays emission. Hybrid images are then created by showing the x-ray image in grayscale and the virtual nuclear projection in colour overlay.

Simulation of projections

The four-dimensional extended cardiac-torso (XCAT) phantom (17) was used to provide a realistic model of an average male (BMI: 25.8 kg/m^2) and an average female (BMI: 24.3 kg/m^2). Two respiratory motion profiles were simulated for both phantoms: normal tidal breathing (period: 3 s inhale, 2 s exhale, anterior-posterior motion: 1.2 cm, diaphragm motion: 2.0 cm (17)) and extreme irregular breathing (period: 1 s inhale, 1 s breath-hold, 2 s exhale, 1 s breath-hold, anterior-posterior motion: 2.0 cm, diaphragm motion: 5.0 cm (18)). A homogeneous distribution of 150 MBq of ^{99m}Tc-MAA in liver and lungs was assumed, corresponding to a clinical scout dose for radioembolisation (1). LSFs of 0, 1, 2, 5, 10, 15, 20, 25, 30 and 35% were simulated.

Two hybrid imaging protocols were simulated: breath-hold (5 s acquisition time, ~30 kcounts) and dynamic breathing (10 frames of 0.5 s, one breathing cycle, ~30 kcounts). For comparison purposes, planar scintigraphy geometric mean (GM) images were also simulated (300 s acquisition time, ~2.5 Mcounts). In addition, interventional nuclear imaging using a single-head mobile gamma camera was simulated (300 s acquisition time, ~1.25 Mcounts). To investigate the standard deviation on the estimated LSF due to statistical fluctuations, 10 simulations of each acquisition protocol were simulated by adding Poisson noise of equal level but different random seeds to noise-free projection images.

Hybrid imaging

Realistic sets of emission projections acquired with low-energy-ultra-high-resolution (LEUHR) parallel hole collimators (19) of the static and dynamic imaging protocols were simulated with the Utrecht Monte Carlo System (UMCS), including scatter and attenuation effects (20,21). An intrinsic resolution of 3.8 mm full width at half maximum (FWHM) and an energy resolution of 10% FWHM at 140 keV were assumed. The energy window was set to 140 keV ± 7.5% and projections were simulated on a matrix of 128 x 128 pixels with 2.4 x 2.4 mm^2 pixel size.

To create an emission projection matching the projection geometry of the fluoroscopic image, the four simulated projections were reconstructed into a volume of 64 x 64 x 64 voxels with 4.8 x 4.8 x 4.8 mm^3 voxel size using a maximum likelihood expectation-maximisation (MLEM) algorithm incorporating point spread function modelling (22). No scatter and attenuation effects were modelled during reconstruction. Finally, the emission projection (64 x 64 pixels,

4.8 x 4.8 mm^2 pixel size) that perfectly overlapped the x-ray projection was created by projecting the reconstructed activity distribution along the projection geometry of the x-rays emission. We will refer to this overlapping projection as the virtual nuclear projection.

The number of counts in the lung and liver region in the virtual nuclear projection is dependent on the number of iterations used during reconstruction (23). The optimal number of iterations for breath-hold and dynamic hybrid imaging was defined as the number of iterations needed to reach convergence of estimated LSF (LSF change < 0.05%) for all simulated fractions and was determined in the normal breathing male phantom. This resulted in 13 iterations for breath-hold hybrid imaging and 12 iterations for dynamic hybrid imaging.

Noise-free x-ray images were generated from eight attenuation maps, ranging from 5 to 75 keV. For each attenuation map, a transmission image was simulated by calculating the transmission along the projection geometry of the x-rays emissions from the focal spot to the x-ray detector (24). Subsequently, the eight transmission images were combined according to their relative contribution to an 80 kVp spectrum with 2 mm aluminium filtration (25,26). X-ray images were simulated on a matrix of 256 x 256 pixels with 1.2 x 1.2 mm^2 pixel size.

Hybrid images were created from the simulated x-ray images and the virtual nuclear projections. Since the detector size was not sufficiently large to image complete lungs and liver at the same time, projections of two FOVs, one covering the liver and one covering the lungs, were simulated and analysed as one set.

Planar scintigraphy

To simulate current clinical practice, anterior and posterior projections of the planar scintigraphy phantom were simulated with UMCS (20,21). Both scatter and attenuation were incorporated in the forward projector and a low-energy-high-resolution (LEHR) collimator was used (19). Projections were simulated on a matrix of 256 x 256 pixels with 2.4 x 2.4 mm^2 pixel size, which is sufficient to image liver and lungs in one view. In clinical practice, however, liver and lungs are imaged separately. Like in clinical practice, LSF estimation was performed on the geometrical mean image calculated from the anterior and posterior projection images. In addition, usage of a single-head mobile gamma camera was simulated by estimating LSF on the anterior projection only.

Calculation of lung shunt fraction

LSF was estimated on all simulated images and compared with the ground truth. Lung shunt fraction was calculated as:

$$\mathrm{LSF} = \frac{N_{lung}}{N_{liver} + N_{lung}} \cdot 100\%,$$

with N_{lung} and N_{liver} the number of total counts in the lungs and liver, respectively (8).

Region of interest delineation

To determine the number of counts in lungs and liver, two-dimensional regions of interest (ROIs) were created in a similar manner as in clinical practice (10). For breath-hold hybrid imaging, lung ROIs were manually delineated on the fluoroscopic image. Liver ROIs were delineated on the virtual nuclear image using a threshold. For high LSFs, the automatically generated ROI extended into the lung area. When that was the case, the lung ROI was used to manually adjust the

boundary of the liver ROI. To compensate for spill-over and collimator resolution effects, a 1 cm margin was added to both the liver and lung ROI. Due to geometrical overlap of liver and lungs, part of the lung ROI overlapped with the liver ROI. This overlapping part was removed from the lung ROI, preventing counts originating in the liver to appear in the lung ROI. Figure 3a and Figure 3b show the liver and lung delineations for the normal breathing male phantom in the case of 20% lung shunt fraction.

A static ROI is non-ideal for dynamic hybrid imaging. However, manual delineation of ROIs in all frames separately is a time-consuming task. Therefore, generation of lung and liver ROIs was partly automated in dynamic hybrid imaging by transforming the manually delineated ROIs of the first frame. Transformation parameters were obtained from registering the first x-ray frame to all other x-ray frames using Elastix (27). Registration success was qualitatively assessed by visual assessment of the resulting ROI transformation. To assess the influence of registration errors on LSF estimations, LSF estimations were compared with estimations obtained with manually delineated ROIs in all frames for the irregular breathing male phantom.

ROIs for planar imaging were created in the same manner as in clinical practice. Liver ROIs were manually delineated on the nuclear images. For the delineation of the lung ROIs, a cobalt-57 (^{57}Co) transmission image was created with UMCS with the same settings as used in creating the planar projection images. To this end, a 500 MBq ^{57}Co flood source of 4.8 mm thick was positioned at the posterior side of the phantom and an anterior projection of 30 s acquisition time was simulated. Lung ROIs were manually delineated on this anterior projection. To compensate for collimator resolution and breathing effects, a 1 cm margin was added to the liver and lung ROI. The lung ROI consisted of all voxels of the left and right lung ROI, excluding the voxels that overlapped with the liver ROI. Figure 3c shows liver and lung ROIs for the normal breathing male phantom in the case of 20% lung shunting. ROIs for single-head mobile gamma camera imaging were created identically.

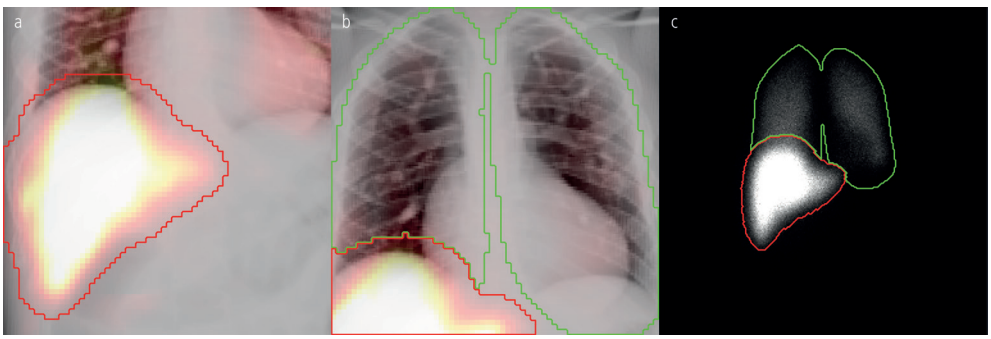

Figure 3: ROI delineation on simulated projections of the normal breathing male phantom with 20% LSF. (a) Breath-hold hybrid image of liver FOV, (b) breath-hold hybrid image of lung FOV, (c) planar GM projection. Liver ROIs are indicated in red, lung ROIs are indicated in green. Images are linearly window-levelled between 0 and 1.5 times the mean number of counts in the liver ROI.

Attenuation correction

Hybrid imaging

Ideally, a correction for attenuation would be made during the three-dimensional image reconstruction, requiring a three-dimensional attenuation map. However, the hybrid imaging system generates a two-dimensional x-ray image, rather than a three-dimensional attenuation map. Therefore, we use the x-ray image to roughly correct the virtual nuclear projection for attenuation effects. Central to this approach is the approximation that activity is homogenously distributed in uniform tissue. In that case, attenuation correction is independent of the direction of the projections and allows the use of the x-ray image. Notice that this will not be a perfect attenuation correction, it roughly corrects for attenuation differences between lung and liver tissue, which is suggested to cause LSF overestimation (9).

The proposed attenuation correction method consists of three steps. First, the local thickness of the patient in the lung and liver ROI is pixel-wise estimated from the transmission of x-ray photons in the fluoroscopic image. Transmission of photons through tissue is given by:

$$T = \int I_0(E) e^{-(\mu_1(E)d_1 + \mu_2(E)d_2 + \cdots + \mu_n(E)d_n} dE,$$

with I_0 the incoming beam intensity, $\mu_i(E)$ the linear attenuation coefficient of tissue i for a photon of energy E, d_i the thickness of tissue i and where the integration runs over the entire energy spectrum of the incident intensity I_0. To reduce the complexity of estimating local thickness for the attenuation correction, it was assumed that (a) fluoroscopic images originated from a mono-energetic x-ray beam at 40 keV, which is approximately the mean energy of the true poly-energetic x-ray spectrum, (b) x-ray photons in the liver ROI had only travelled through soft (liver) tissue and (c) x-ray photons in the lung ROI had only travelled through the lungs (1/3 soft tissue, 2/3 air (28)). This simplifies the equation to:

$$T_{liver} = I_0 e^{-\mu_{liver} d_{liver}},$$

and

$$T_{lung} = I_0 e^{-\mu_{lung} d_{lung}},$$

with μ_{liver} equal to 0.2849 cm^{-1} and μ_{lung} equal to 0.09467 cm^{-1} at 40 keV (29). In our simulations, I_0 was equal to 1. In clinical practice, I_0 can be approximated by the intensity of an uattenuated pixel at the side of the body. Tissue thickness was then calculated per pixel in the liver and lung ROI.

Next, mean attenuation of gamma photons in the liver and lung ROI is pixel-wise calculated based on the estimated local tissue thickness d_{liver} and d_{lung} as follows:

$$Att_{liver} = \frac{\int_0^{d_{liver}} e^{-\mu_{liver} x} dx}{d_{liver}},$$

and

$$Att_{lung} = \frac{\int_0^{d_{lung}} e^{-\mu_{lung} x} dx}{d_{lung}},$$

with μ_{liver} equal to 0.1624 cm^{-1} and μ_{lung} equal to 0.05392 cm^{-1} at 140 keV (29). Here, we assumed that activity was homogenous distributed through the tissue. Finally, the number of counts in the liver and lung ROIs in the virtual nuclear projection are corrected for attenuation

effects by pixel-wise division through the calculated attenuation factor Att_{liver} and Att_{lung}, respectively.

Planar scintigraphy

In planar scintigraphy, no fluoroscopic image is available for pixel-wise attenuation correction. However, if uniform thickness is assumed, geometric mean images can be compensated for differences in attenuation between different tissues. Therefore, the number of counts in the liver ROI was corrected with $e^{-\mu_{abdomen}d_{abdomen}}$ and the number of counts in the lung ROI was corrected with $e^{-\mu_{thorax}d_{thorax}}$, with $\mu_{abdomen}$ (0.116 cm^{-1}) and μ_{thorax} (0.096 cm^{-1}) nominal values for attenuation in the thorax and abdomen (30) and $d_{abdomen}$ and d_{thorax} the mean thickness of the abdomen and thorax, respectively. In our simulations, we approximated $d_{abdomen}$ and d_{thorax} as the mean thickness of the XCAT phantom in the liver and lung ROI, respectively. In clinical practice, $d_{abdomen}$ and d_{thorax} could be measured physically or via lateral views. For the single-head mobile gamma camera, no straightforward attenuation correction approach is available. Therefore, no attenuation correction is applied.

Organ overlap correction in hybrid imaging

Organ overlap of lungs and liver on the hybrid image may cause counts originating from the lungs ending up in the liver ROI. A pre-treatment computed tomography (CT) scan, with lungs and liver delineated and registered to the fluoroscopy image (31,32), can be used to correct for this overlap.

In our simulations, the XCAT attenuation maps were used as surrogates for a pre-treatment CT scan and the XCAT activity maps as lung and liver delineations. To mimic a more realistic situation, small registration errors were introduced with Elastix by translating and rotating the attenuation maps randomly between -5 and +5 mm and -5 to +5 degrees, respectively, for all simulated LSFs (27,33). For each noise realisation, a different registration error was applied.

To determine the region on the hybrid image where lungs and liver are geometrically overlapping, the three-dimensional XCAT lung and liver activity maps were projected separately according to the fluoroscopy geometry. By combining these projections, the region in which lungs and liver are overlapping on the projections was delineated. Next, the fraction of lung counts in the overlapping region was determined by dividing the number of counts in the overlapping region by the total number of counts in the lung region. Note that the overlapping region used to determine this fraction originated from the registered CT scan and not from the manually delineated ROIs used to calculate the LSF. The fraction of lung counts in the overlapping region was then used to correct the number of liver and lung counts in the manually delineated ROIs as follows:

$$N^*_{lung} = N_{lung} \cdot \frac{1}{1 - f_{lung}},$$

$$N^*_{liver} = N_{liver} - f_{lung} \cdot N^*_{lung},$$

with N^*_{lung} and N^*_{liver} the corrected number of counts in the lung and liver ROI, N_{lung} and N_{liver} the measured number of counts in the lung and liver ROI, and f_{lung} the fraction of lung counts in the overlap region.

Results

Automated ROI delineation in dynamic imaging

Figure 4 shows the automatically transformed liver and lung ROIs of the normal breathing male phantom used in the calculation of LSF in dynamic hybrid imaging. Visually, the liver ROIs match the activity in the liver well. In the lungs, ROIs also match well with the x-ray image. For the female phantom, similar results were obtained. Automatically generated ROIs resulted in an absolute difference of at most 3.5 percentage points (pp) in LSF estimation compared with manual delineation of ROIs in all frames for the irregular breathing male phantom.

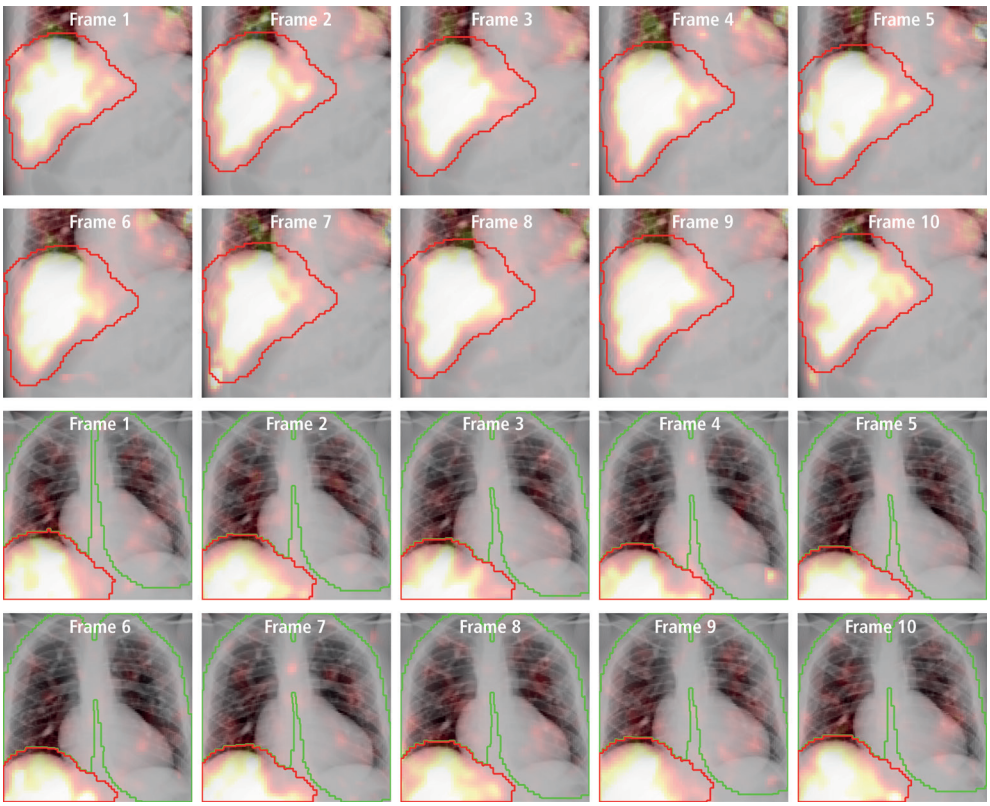

Figure 4: Transformed liver and lung ROIs for one set of dynamic hybrid images with 20% LSF (normal breathing male phantom). ROIs were manually delineated in the first frame. After registering the x-ray image of the first frame to all other frames, the ROIs were transformed according to the x-ray transformation parameters. Liver ROIs are indicated in red, lung ROIs are indicated in green. Images are linearly window-levelled between 0 and 1.5 times the mean number of counts in the liver ROI.

Lung shunt fraction estimation

Figure 5 shows the absolute error in estimated lung shunt fraction after attenuation correction. For hybrid imaging, LSF in the clinical relevant range of 10-20% was overestimated by 0 to 2.5 pp, independent of body shape and breathing pattern. In this LSF range with planar scintigraphy, the error in estimated LSF ranged between an underestimation of 3 pp and an overestimation of 1 pp, with an error more strongly depending on body shape and breathing pattern. Similarly, the single-head mobile gamma camera resulted in an error between an underestimation of 2 pp and an overestimation of approximately 4 pp, strongly depending on body shape and breathing pattern. In general, larger errors were found for the irregular breathing phantom, although the hybrid imaging device was less sensitive to this.

In case organ overlap was corrected in hybrid imaging, the range of LSF overestimation was lowered from 3 pp to 1 pp in the clinical relevant range of 10-20% LSF in all phantoms (Figure 6), again fairly independent on body shape and breathing pattern. Due to the motion capture in hybrid imaging, breathing had no significant effect on the accuracy.

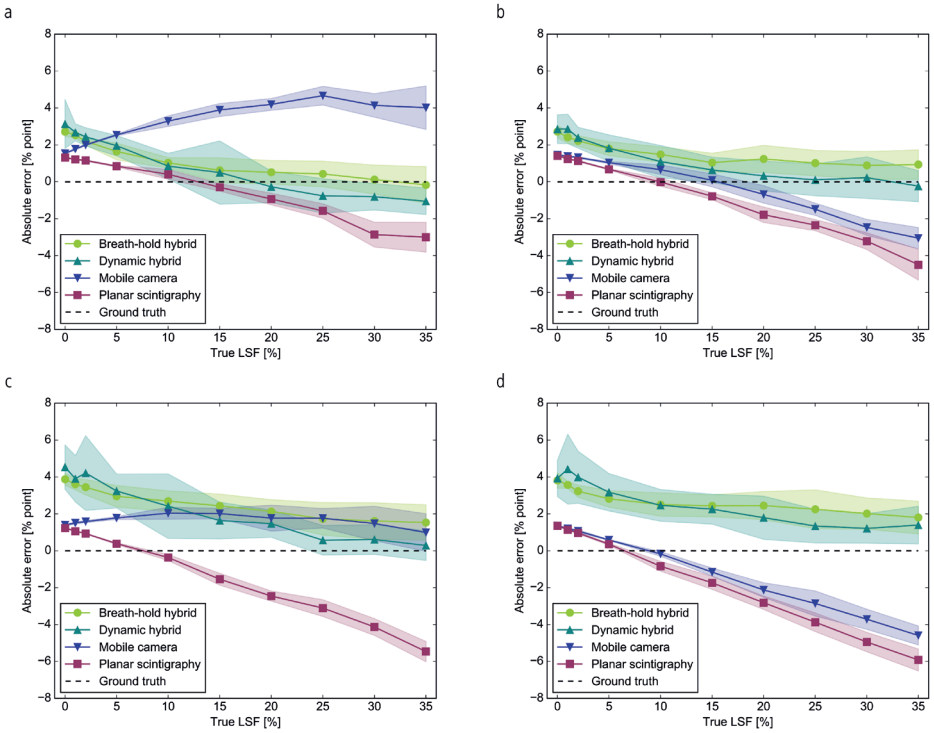

Figure 5: Absolute error of the estimated LSF for (a, c) the male phantom and (b, d) the female phantom. Top row: normal breathing; bottom row: irregular breathing. The shaded area denotes the range between the mean plus two standard deviations and the mean minus two standard deviations.

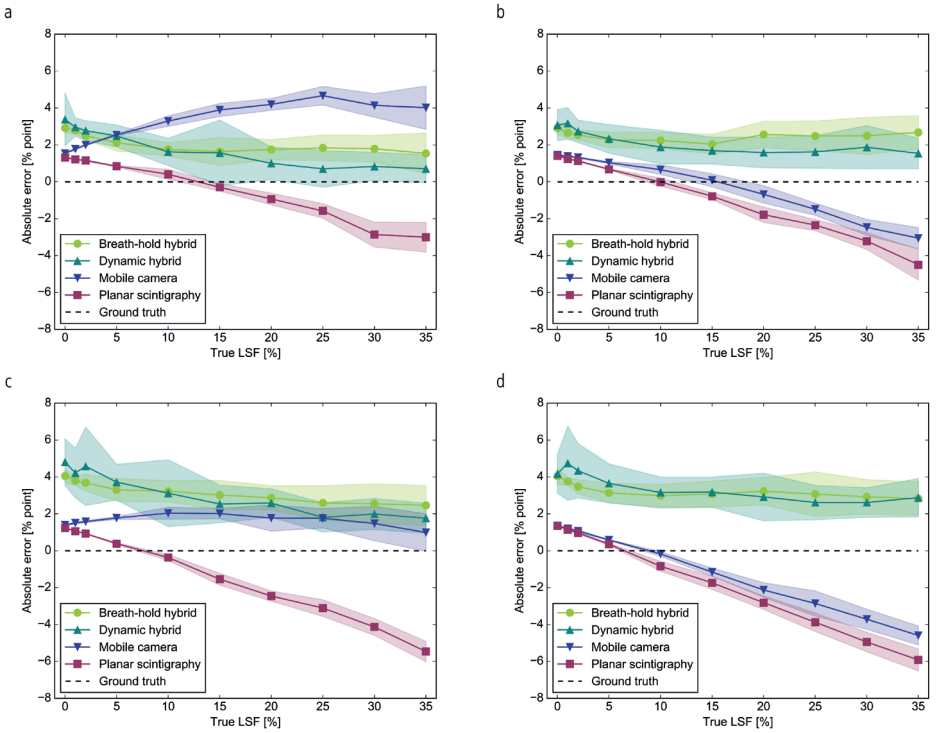

Figure 6: Absolute error of the estimated LSF after overlap correction in hybrid imaging for (a, c) the male phantom and (b, d) the female phantom. Top row: normal breathing; bottom row: irregular breathing. The shaded area denotes the range between the mean plus two standard deviations and the mean minus two standard deviations.

Discussion

The accuracy of hybrid fluoroscopic and nuclear images to estimate the LSF during ^{90}Y radioembolisation procedures of liver tumours was investigated. Hybrid images of a male and a female phantom with radioactivity shunting from the liver to the lungs were simulated for two hybrid imaging protocols. Planar scintigraphy images were simulated as the current clinical practice imaging protocol. In addition, images of a single-head mobile gamma camera were simulated as the simplest method of interventional imaging. LSFs were estimated on the simulated images and compared with the ground truth. Hybrid imaging resulted in an overestimation of LSF, which was constant over the simulated LSF range and for all phantoms (male/female body shape and normal/irregular breathing). In contrast, errors in LSF estimation for planar scintigraphy and the single-head mobile gamma camera were highly dependent on LSF, body shape and breathing profile.

In general, irregular breathing led to slightly larger errors than normal breathing. In planar scintigraphy and single-head mobile gamma camera imaging, irregular breathing led to a larger underestimation of LSF. Due to the larger motion of the liver in the irregular breathing phantom, the liver ROI contained more lung counts than in the normal breathing phantom.

For LSFs larger than 10%, dynamic hybrid imaging resulted in more accurate LSF estimation than breath-hold hybrid imaging. The reason for this is two-fold. First of all, estimated LSF varies with phase in the respiratory cycle. Static hybrid imaging was simulated at full inhalation, while in dynamic hybrid imaging an average over one breathing cycle was used. In the XCAT phantom, lung density varies with phase in the respiratory breathing cycle. This resulted in the largest overestimation at full inhalation, while full exhalation resulted in the lowest overestimation. Secondly, a negative bias is introduced when projections with low count statistics are reconstructed (~6500 counts in a static projection versus ~650 counts in a dynamic projection), which results from a bias towards zero when adding Poisson noise to low-count projections.

The presented attenuation correction method for hybrid imaging is unlikely to correct nuclear projections perfectly. This is due to both scatter and to coarse assumptions. The dilated liver ROI partly incorporates lung tissue, which violates the assumption that only soft (liver) tissue is present in the liver ROI. This causes a large underestimation of tissue thickness, resulting in an underestimation of the attenuation correction factor. With regard to scatter, more scattered photons originating from the liver end up in the lung ROI than vice versa. In addition, the relative number of scattered photons in the lung ROI is larger for low lung shunt fractions. Together, these effects result in a less accurate attenuation correction. The method could potentially be improved by including window-based scatter correction.

For the female phantom, the assumption that only lung tissue is present in the lung ROI does not hold (i.e. breast tissue). This results in an overestimation of the thickness of the patient, leading to an overestimation of the attenuation correction factor. Consequently, the number of counts in the lung ROI is underestimated. This was reflected in a smaller correction of the LSF for the female phantom as compared with the male phantom.

In this study, pre-treatment images were used to correct for organ overlap. Commonly, interventions are preceded by extensive image acquisitions, including CT or MRI, to study vessel and organ anatomy. Registration of the fluoroscopy image to the pre-treatment CT scan is expected to take a few minutes on a standard workstation (32). In a realistic clinical setting,

liver and lungs have to be delineated in a pre-treatment CT scan in order to determine the overlapping region on the projections. Delineation of liver and lungs in a three-dimensional volume can be a time-consuming task, although the time needed can be significantly reduced by using a semi-automatic segmentation method, e.g. (34,35). Furthermore, the delineation can be performed beforehand, thus not increasing treatment time. To investigate the influence of the introduced registration errors on LSF estimations, we also corrected LSF estimations with the original attenuation maps, simulating perfect registrations. This showed that registration had only a minor influence on the corrected LSF values (absolute difference at most 0.5 pp). Small errors in the three-dimensional liver and lung delineations are expected to have a comparable influence on LSF estimations as registration errors.

Estimating LSF with a single-head mobile gamma camera resulted in an overestimation for the male phantom, while an underestimation was found in the female phantom. Overestimation is suggested to be caused by the relative difference in attenuation between liver and lungs, with activity in the lungs being much less attenuated than activity in the liver (9,36,37). However, breast tissue of the female phantom causes more attenuation of the activity in the lungs, resulting in an underestimation. Since no straightforward attenuation correction is available when using a single-head mobile gamma camera, the degree of over- or underestimation will be largely dependent on body type. Like in planar scintigraphy, a flood image could be used to estimate attenuation in the liver and lung regions. Resulting LSF estimations are likely to be of comparable accuracy to estimations of planar scintigraphy.

Attenuation correction in planar scintigraphy requires an estimation of the thickness of the patient. In this study, we used the average thickness of the XCAT phantom. In clinical practice, however, this estimation will be less accurate. The presented errors in LSF estimations with planar scintigraphy are therefore likely to be slightly larger in clinical practice.

The accuracy of estimating LSF with our hybrid imaging device has been assessed with a male and female XCAT phantom, since clinical data is not yet available. A large variety of body shapes and breathing profiles will be seen in clinical practice, which will affect lung shunt estimations. Although the absolute error in estimating LSF will vary per individual, this phantom study has shown that estimating LSF with our hybrid imaging device results in a constant error, regardless of body shape and breathing profile. In addition, the possibility of dynamic hybrid imaging shows that free breathing does not result in loss of accuracy, which is a great asset in an interventional setting. In contrast, estimating LSF with planar scintigraphy or a single-head mobile gamma camera results in errors which are highly dependent on body shape and breathing profile.

While the hybrid imaging device is equipped with LEUHR collimators instead of the LEHR collimators used in planar scintigraphy, this does not lead to a higher imaging resolution due to the relatively large collimator-patient distance. This is not a handicap per se, since the hybrid imaging system is not aimed at providing the physician with images of the highest spatial resolution, but it is aimed at providing quick insight into the radionuclide distribution.

The availability of nuclear medicine images in the intervention room directly after administration of the scout dose would shorten treatment times considerably. Gates et al. (13) reported a mean total single-session procedure time of 2.70 hours, of which 0.45 hours accounted for nuclear imaging. Planar scintigraphy was performed within 2 hours after administration of ^{99m}Tc-MAA, but transfer times were not included in the reported procedure times. With our hybrid imaging device, nuclear imaging can be started immediately after administration of ^{99m}Tc-MAA.

This will result in images of higher quality due to less ^{99m}Tc-MAA degrading to free pertechnetate. In addition, we estimate that this would shorten procedure times by 0.5 to 1 hours. Time needed for nuclear imaging, LSF estimations and dose calculations will be comparable to the 0.45 hours reported by Gates et al. (13). Furthermore, the catheter can be kept in place, which would enable for administration of the scout dose and the therapeutic dose at the exact same position. This may greatly enhance the prognostic power of the pre-treatement procedure (16).

Recently, it has been proposed to estimate LSF with SPECT/CT rather than with planar scintigraphy, resulting in a more accurate LSF estimation due to attenuation and scatter correction (10,35,36). Since SPECT/CT is not yet clinically used to estimate LSF, we did not compare the accuracy of our hybrid imaging device with SPECT/CT. However, our hybrid imaging device has the potential of three-dimensional imaging, by rotating the device around the patient (cone beam CT principle). This allows attenuation and scatter correction in a similar manner as in SPECT/CT, potentially giving a more accurate LSF estimation than presented in this study.

It has been suggested that LSF estimations with ^{99m}Tc-MAA may not predict the distribution of ^{90}Y microspheres. In a study by Elschot et al. (10), it was shown that LSF was overestimated by ^{99m}Tc-MAA compared with estimations from ^{166}Ho microspheres. This was suggested to be caused by the relative large fraction of small ^{99m}Tc-MAA particles (<20 μm), which are more prone to shunt to the lungs than the larger and more stable ^{166}Ho microspheres. This difference in LSF estimation is also likely to be present when using ^{90}Y microspheres, since glass and resin ^{90}Y microspheres are similar in size and stability to ^{166}Ho microspheres. However, our hybrid imaging device has the potential to image ^{90}Y and ^{166}Ho, thus allowing estimation of LSF directly from a scout dose of microspheres.

The addition of the gamma cameras will be feasible with both a circular image intensifier and a rectangular flat panel, since it is not crucial to match the FOVs of both modalities exactly, although hybrid images can only be created for the part of the patient that is seen by both modalities. The addition of nuclear image capability to the fluoroscopic c-arm will not influence its routine use, since no modifications will be made to the fluoroscopic system. The added weight at the side of the x-ray tube can be compensated for by a counterweight and mobility can be guaranteed by a driving motor. Therefore, all orientations of the c-arm will still be possible. For radioembolisation procedures, access to the patient is not altered, since the interventional radiologist is operating at the groin level, while the hybrid imaging system is positioned at the abdominal or thoracic level. In addition, the x-ray tube and the gamma cameras are usually positioned under the table, thus not interfering with the normal workflow. Other procedures, such as sentinel node procedures (38) and biopsies (39), can potentially also benefit from the availability of live hybrid images.

Uniformity and sensitivity may vary between the four gamma cameras due to minor deviations in gamma camera position and non-uniformity of the gamma camera itself. Variability in the position and rotation of the gamma cameras can be compensated for by calibration of the system parameters used during reconstruction (40). Variability in uniformity and sensitivity of the gamma cameras itself can be compensated for by calibration protocols, such as non-uniformity correction using flood sources. Therefore, variability in uniformity and sensitivity is expected to have a negligible influence on LSF estimation in a decent calibrated system.

Overestimation of LSF can be detrimental for patients with large lung shunt fractions, potentially excluding them from receiving radioembolisation therapy because of increased risk of

radiation pneumonitis. We have shown that errors in LSF estimation are constant over different body shapes and breathing patterns. Furthermore, the set-up with four gamma cameras allows shorter acquisition times compared with planar imaging.

Conclusion

Availability of real-time hybrid images during ^{90}Y radioembolisation of liver tumours may provide the interventional radiologist with useful additional information regarding distribution of radioactivity. With our hybrid imaging device, lung shunt fraction can be robustly estimated with a constant error over the simulated LSF range for all body shapes and breathing patterns. In contrast, estimated LSF is highly varying when estimated with planar scintigraphy or a single-head mobile gamma camera. The hybrid imaging device is capable of estimating LSF within a few seconds in an interventional setting.

References

1. AJAT Braat, MLJ Smits, MNGJA Braat, AF van den Hoven, JF Prince, HWAM de Jong, et al., ^{90}Y Hepatic Radioembolization: An Update on Current Practice and Recent Developments, J. Nucl. Med., 2015, 56(7):1079–87.
2. A Kennedy, D Coldwell, B Sangro, H Wasan, and R Salem, Radioembolization for the Treatment of Liver Tumors, Am. J. Clin. Oncol., 2012, 35(1):91–9.
3. MLJ Smits, M Elschot, DY Sze, YH Kao, JFW Nijsen, AH Iagaru, et al., Radioembolization Dosimetry: The Road Ahead, Cardiovasc. Intervent. Radiol., 2015, 38(2):261–9.
4. S Gnesin, L Canetti, S Adib, N Cherbuin, M Silva-Monteiro, P Bize, et al., Partition model based ^{99m}Tc-MAA SPECT/CT predictive dosimetry compared to ^{90}Y TOF PET/CT post-treatment dosimetry in radioembolisation of hepatocellular carcinoma: A quantitative agreement comparison, J. Nucl. Med., 2016, 57(11):1672–8.
5. C Carretero, M Munoz-Navas, M Betes, R Angos, JC Subtil, I Fernandez-Urien, et al., Gastroduodenal injury after radioembolization of hepatic tumors, Am. J. Gastroenterol., 2007, 102(6):1216–20.
6. S Ho, WY Lau, TWT Leung, M Chan, PJ Johnson, and AKC Li, Clinical evaluation of the partition model for estimating radiation doses from yttrium-90 microspheres in the treatment of hepatic cancer, Eur. J. Nucl. Med., 1997, 24(3):293–8.
7. A Riaz, RJ Lewandowski, LM Kulik, MF Mulcahy, KT Sato, RK Ryu, et al., Complications Following Radioembolization with Yttrium-90 Microspheres: A Comprehensive Literature Review, J. Vasc. Interv. Radiol., 2009, 20(9):1121–30.
8. Sirtex Medical Limited, SIR-Spheres package insert (CR1507), North Sydney, NSW, Australia: 2012.
9. R Bastiaannet, MA Viergever, and HWAM de Jong, Impact of respiratory motion and acquisition settings on SPECT liver dosimetry for radioembolization, Med. Phys., 2017, 44(10):5270–9.
10. M Elschot, JFW Nijsen, MGEH Lam, MLJ Smits, JF Prince, MA Viergever, et al., ^{99m}Tc-MAA overestimates the absorbed dose to the lungs in radioembolization: a quantitative evaluation in patients treated with ^{166}Ho-microspheres, Eur. J. Nucl. Med. Mol. Imaging, 2014, 41(10):1965–75.
11. A Kennedy, S Nag, R Salem, R Murthy, AJ McEwan, C Nutting, et al., Recommendations for Radioembolization of Hepatic Malignancies Using Yttrium-90 Microsphere Brachytherapy: A Consensus Panel Report from the Radioembolization Brachytherapy Oncology Consortium, Int. J. Radiat. Oncol. Biol. Phys., 2007, 68(1):13–23.
12. A Gabr, JR Kallini, VL Gates, R Hickey, L Kulik, K Desai, et al., Same-day ^{90}Y radioembolization: implementing a new treatment paradigm, Eur. J. Nucl. Med. Mol. Imaging, 2016, 43(13):2353–9.
13. VL Gates, KG Marshall, K Salzig, M Williams, RJ Lewandowski, and R Salem, Outpatient Single-Session Yttrium-90 Glass Microsphere Radioembolization, J. Vasc. Interv. Radiol., 2014, 25(2):266–70.
14. C Beijst, M Elschot, MA Viergever, and HWAM de Jong, Toward Simultaneous Real-Time Fluoroscopic and Nuclear Imaging in the Intervention Room, Radiology, 2016, 278(1):232–8.

15. S van der Velden, C Beijst, MA Viergever, and HWAM de Jong, Simultaneous fluoroscopic and nuclear imaging: impact of collimator choice on nuclear image quality, Med. Phys., 2017, 44(1):249–61.
16. E Garin, J Edeline, and Y Rolland, High Impact of Preferential Flow on ^{99m}Tc-MAA and ^{90}Y-Loaded Microsphere Uptake Correlation, J. Nucl. Med., 2016, 57(11):1829–30.
17. WP Segars, G Sturgeon, S Mendonca, J Grimes, and BMW Tsui, 4D XCAT phantom for multimodality imaging research, Med. Phys., 2010, 37(9):4902–15.
18. SS Vedam, VR Kini, PJ Keall, V Ramakrishnan, H Mostafavi, and R Mohan, Quantifying the predictability of diaphragm motion during respiration with a noninvasive external marker, Med. Phys., 2003, 30(4):505–13.
19. Siemens Healthineers, Symbia S and T System Specifications, 2010.
20. FJ Beekman, HWAM De Jong, and S Van Geloven, Efficient fully 3-D iterative SPECT reconstruction with Monte Carlo-based scatter compensation, IEEE Trans. Med. Imaging, 2002, 21(8):867–77.
21. HWAM de Jong, ETP Slijpen, and FJ Beekman, Acceleration of Monte Carlo SPECT simulation using convolution-based forced detection, IEEE Trans. Nucl. Sci., 2001, 48(1):58–64.
22. EVR Di Bella, AB Barclay, RL Eisner, and RW Schafer, A comparison of rotation-based methods for iterative reconstruction algorithms, IEEE Trans. Nucl. Sci., 1996, 43(6):3370–6.
23. HH Barrett, DW Wilson, and BMW Tsui, Noise properties of the EM algorithm. I. Theory, Phys. Med. Biol., 1994, 39(5):833–46.
24. RL Siddon, Fast calculation of the exact radiological path for a three-dimensional CT array, Med. Phys., 1984, 12(2):252–5.
25. JM Boone, TR Fewell, and RJ Jennings, Molybdenum, rhodium, and tungsten anode spectral models using interpolating polynomials with application to mammography, Med. Phys., 1997, 24(12):1863–74.
26. JM Boone, and JA Seibert, An accurate method for computer-generating tungsten anode x-ray spectra from 30 to 140 kV, Med. Phys., 1997, 24(11):1661–70.
27. S Klein, M Staring, K Murphy, MA Viergever, and JPW Pluim, Elastix: A Toolbox for Intensity-Based Medical Image Registration, IEEE Trans. Med. Imaging, 2010, 29(1):196–205.
28. B Holman, V Cuplov, L Millner, BF Hutton, TM Maher, AM Groves, et al., Improved correction for the tissue fraction effect in lung PET/CT imaging, Phys. Med. Biol., 2015, 60(18):7387–402.
29. JH Hubbell, and SM Seltzer, Tables of X-ray mass attenuation coefficients and mass energy-absorption coefficients 1 keV to 20 MeV for elements Z = 1 to 92 and 48 additional substances of dosimetric interest, National Inst. of Standards and Technology-PL, Gaithersburg, MD (United States), Ionizing Radiation Div., 1995.
30. NP Rowell, J Glaholm, MA Flower, B Cronin, and VR McCready, Anatomically derived attenuation coefficients for use in quantitative single photon emission tomography studies of the thorax, Eur. J. Nucl. Med., 1992, 19(1):36–40.
31. P Markelj, D Tomaževic, B Likar, and F Pernuš, A review of 3D/2D registration methods for image-guided interventions, Med. Image Anal., 2012, 16(3):642–61.

32. IMJ van der Bom, S Klein, M Staring, R Homan, LW Bartels, and JPW Pluim, Evaluation of optimization methods for intensity-based 2D-3D registration in x-ray guided interventions, Proc. SPIE, 2011, 7962(1):796223.
33. G Li, TJ Yang, H Furtado, W Birkfellner, A Ballangrud, SN Powell, et al., Clinical Assessment of 2D/3D registration accuracy in 4 major anatomic sites using on-board 2D kilovoltage images for 6D patient setup, Technol. Cancer Res. Treat., 2015, 14(3):305–14.
34. S Hu, EA Hoffman, and JM Reinhardt, Automatic lung segmentation for accurate quantitation of volumetric X-ray CT images, IEEE Trans. Med. Imaging, 2001, 20(6):490–8.
35. SJ Lim, YY Jeong, and YS Ho, Automatic liver segmentation for volume measurement in CT images, J. Vis. Commun. Image Represent., 2006, 17(4):860–75.
36. YH Kao, BM Magsombol, Y Toh, KH Tay, PK Chow, AS Goh, et al., Personalized predictive lung dosimetry by technetium-99m macroaggregated albumin SPECT/CT for yttrium-90 radioembolization, EJNMMI Res., 2014, 4(1):33.
37. N Yu, SM Srinivas, FP Difilippo, S Shrikanthan, A Levitin, G McLennan, et al., Lung dose calculation with SPECT/CT for 90Yittrium radioembolization of liver cancer, Int. J. Radiat. Oncol. Biol. Phys., 2013, 85(3):834–9.
38. S Vidal-Sicart, ME Rioja, P Paredes, MR Keshtgar, and RA Valdés Olmos, Contribution of perioperative imaging to radioguided surgery, Q. J. Nucl. Med. Mol. imaging, 2014, 58(2):140–60.
39. K Kobayashi, P Bhargava, S Raja, F Nasseri, HA Al-Balas, DD Smith, et al., Image-guided biopsy: what the interventional radiologist needs to know about PET/CT, Radiographics, 2012, 32(5):1483–501.
40. C Beijst, M Elschot, S van der Velden, and HWAM de Jong, Multimodality calibration for simultaneous fluoroscopic and nuclear imaging, EJNMMI Phys., 2016, 3(1):20.

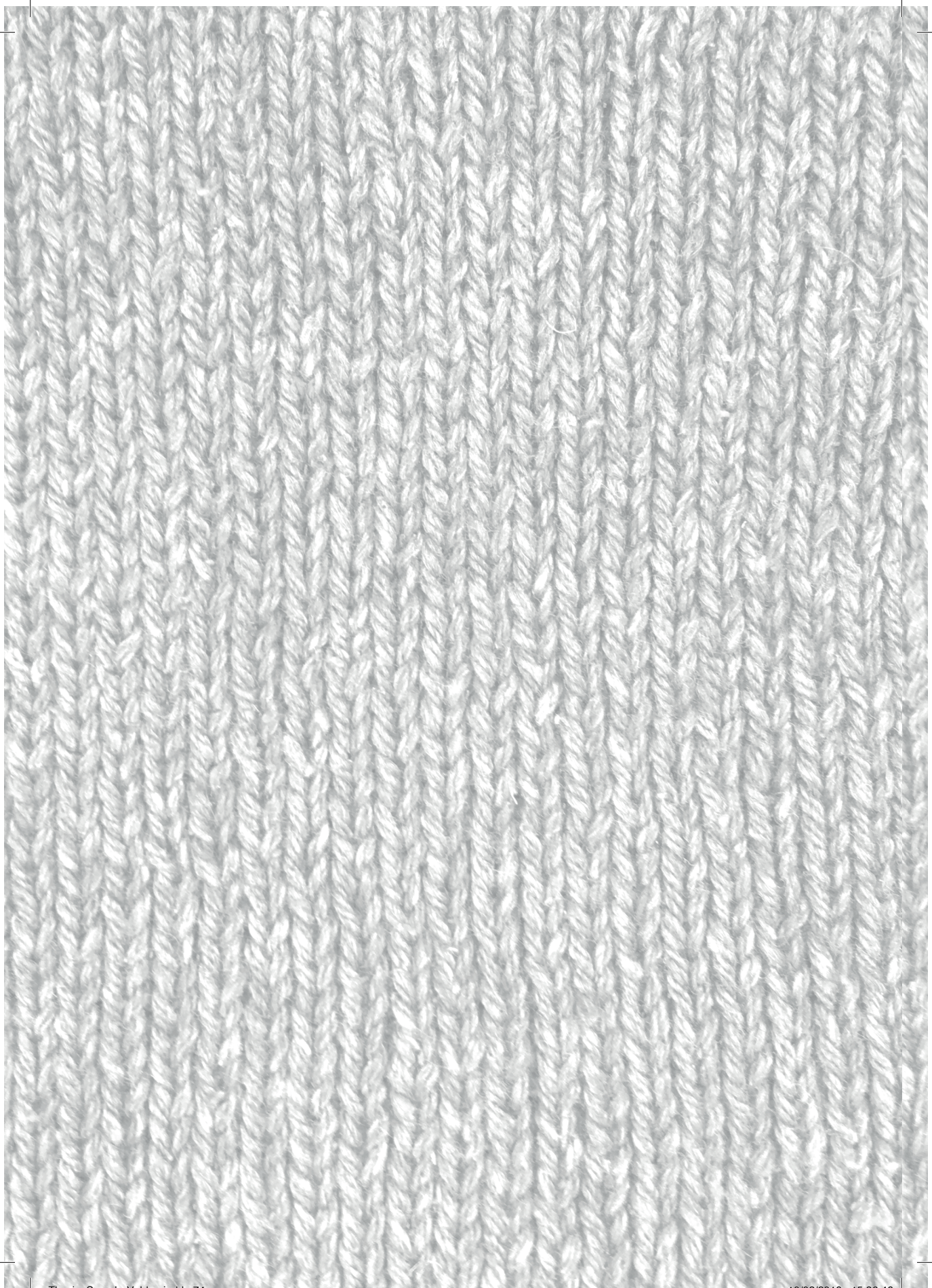

5

Fast technetium-99m liver SPECT for evaluation of the pre-treatment procedure for radioembolisation dosimetry

Based on:

S. van der Velden, M.M.A. Dietze, M.A. Viergever, H.W.A.M. de Jong, "Fast technetium-99m liver SPECT for evaluation of the pretreatment procedure for radioembolization dosimetry", Medical Physics, 2019, nr. 1, vol. 46, pp. 345-355

Abstract

Purpose

The efficiency of radioembolisation procedures could be greatly enhanced if results of the pre-treatment procedure were immediately available in the interventional suite, enabling single-session procedures as a result of direct estimation of the hepatic radiation dose and lung shunt fraction. This would, however, require a relatively fast, but still quantitative, SPECT procedure, which might be achieved with acquisition protocols using non-uniform durations of the projection images.

Materials and methods

SPECT liver images of the 150-MBq ^{99m}Tc-MAA pre-treatment procedure were simulated for eight different lesion locations and two different lesion sizes using the digital XCAT phantom for both single- and dual-head scanning geometries with respective total acquisition times of 1, 2, 5, 10, and 30 minutes. Three non-uniform projection-time acquisition protocols ("half-circle SPECT (HCS)", "non-uniform SPECT (NUS) I" and "NUS II") for fast quantitative SPECT of the liver were designed and compared with the standard uniform projection-time protocol. Images were evaluated in terms of contrast-to-noise ratio (CNR), activity recovery coefficient (ARC), tumour/non-tumour (T/N) ratio and lung shunt fraction (LSF) estimation. In addition, image quality was verified with a physical phantom experiment, reconstructed with both clinical and Monte Carlo-based reconstruction software.

Results

Simulations showed no substantial change in image quality and dosimetry by usage of a non-uniform projection-time acquisition protocol. Upon shortening acquisition times, CNR dropped, but ARC, T/N ratio and LSF estimates were stable across all simulated acquisition times. Results of the physical phantom were in agreement with those of the simulations.

Conclusion

Both uniform and non-uniform projection-time acquisition liver SPECT protocols yield accurate dosimetric metrics for radioembolisation treatment planning in the interventional suite within 10 minutes, without compromising image quality. Consequently, fast quantitative SPECT of the liver in the interventional suite is feasible.

Introduction

Yttrium-90 (^{90}Y) radioembolisation is a treatment for unresectable liver malignancies, in which radioactive microspheres are injected into the hepatic artery (1–3). Prior to the treatment, 150 Mbq technetium-99m macroaggregated albumin (^{99m}Tc-MAA) is given as a simulation of the deposition of the microspheres (2). The distribution of the administered activity is assessed on planar scintigraphy and/or on a single photon emission computed tomography (SPECT)/computed tomography (CT) scan and is used to evaluate the lung shunt fraction (LSF) and the presence of extrahepatic depositions, and to calculate the optimal ^{90}Y dosage based on the partition model (3,4).

Currently, the ^{99m}Tc-MAA activity is given during a procedure preceding the actual treatment, sometimes separated by two or three weeks (2), due to the need to image the patient at the nuclear medicine department for assessment of the ^{99m}Tc-MAA distribution. Having nuclear imaging directly available in the interventional suite would therefore have several advantages. Most importantly, this would simplify implementing radioembolisation as a single-session procedure (5,6), shortening procedure times significantly and potentially making such a fast procedure widely available. In addition, the prognostic power of the pre-treatment procedure may be greatly enhanced by having the catheter in the exact same position as for the treatment (7). Furthermore, the physician will be provided with direct dose feedback, allowing for real-time adjustments if necessary.

Availability of nuclear images in the interventional suite can be achieved by installation of a SPECT/CT scanner in the interventional suite. As an alternative, one could use a mobile or hand-held gamma camera (8,9). Also worth mentioning in this context is a mobile hybrid imaging device, combining a conventional c-arm with gamma cameras, which is currently being developed by our group (10,11). It has been shown that this hybrid imaging device could safely replace current planar imaging in the nuclear medicine department for the estimation of LSF (12), giving acceptable estimates within 10 seconds. However, assessment of LSF on SPECT/CT images is more accurate than estimations based on planar scintigraphy images (13). In addition, SPECT/CT images are needed for treatment planning using the partition model (3,4).

To make a single-session procedure attractive for usage in routine clinical practice, acquisition of a SPECT/CT scan should ideally not take more than 10 minutes (current clinical practice: 30 minutes), which is comparable with the scan and preparation time needed for a cone beam CT. In addition, reducing the acquisition time to 10 minutes would help avoiding clot forming in the catheter and maintaining sterility. However, reducing acquisition times will reduce image quality owing to increased noise and might compromise quantitative accuracy, which is important for radioembolisation dosimetry and treatment planning.

SPECT image quality may be improved by using non-uniform projection-time acquisition protocols, in which more time is spent at angles where the count rate is high (14–17). Usage of non-uniform acquisition time protocols might therefore counteract the loss of image quality due to reduced total acquisition times. One of the simplest non-uniform projection-time acquisition protocols is a half-circle SPECT protocol as is clinically used in cardiac scanning. The rationale of this approach is that the heart is located in the left anterior aspect of the thorax. Consequently, photons coming from the left anterior aspect of the thorax are significantly attenuated when imaged from the back of the patient and might not contribute to image quality. Similar reasoning

can be applied to liver SPECT. The liver is located at the right side of the body. Therefore, radiation emitted from the left side of the body is markedly attenuated, contributing less to image quality. For equal total acquisition times, more counts are obtained for a right anterior 180° orbit than for a 360° orbit. For the appropriate activity distributions, such half-circle SPECT acquisitions can generally yield reasonable reconstructed images. More complex acquisition time protocols than half-circle SPECT that are tailored to the expected activity distribution (14–17) might counteract the loss of image quality by the reduced acquisition times to an even larger extent.

The goal of this study was to investigate the feasibility of acquiring fast liver SPECT scans without compromising the evaluation of the pre-treatment procedure for radioembolisation dosimetry and treatment planning. In addition, the potential benefit of three non-uniform projection-time acquisition protocols was evaluated.

Materials and methods

Acquisition protocols

Impact of shortening acquisition time on image quality was evaluated by simulating 150-MBq technetium-99m (^{99m}Tc) SPECT images acquired with a total acquisition time of 1, 2, 5 and 10 minutes, respectively, for a single-head system and for a dual-head system with the cameras in a 90° configuration, respectively. These images were compared with reference images obtained by simulating the current clinical protocol of a dual-head system with a total scan time of 30 minutes.

Spending more time at angles where the count rate is high improved image quality in (14–17). Therefore, three non-uniform projection-time protocols, half-circle SPECT (HCS), non-uniform SPECT (NUS) I and NUS II, were designed and compared with the standard uniform projection-time protocol in which all projections are acquired with equal acquisition times (Figure 1, first column). In the non-uniform projection-time protocols, the total acquisition time was kept equal to the uniform projection-time protocol, only the distribution of the total time over the views was changed.

The HCS protocol was based on clinically used dedicated cardiac scanners, in which a 180° rotation is standard. In this protocol, the 180° arc closest to the volume of interest (VOI) is scanned (Figure 1, second column).

In the NUS I protocol (Figure 1, third column), a 360° arc is scanned, but with a non-uniform view time distribution. The 360° arc is divided in two parts, where 3/4th of the total acquisition time is spent at the 180° arc scanned with the HCS protocol and 1/4th of the total acquisition time at the other 180° arc.

A single-head system is more flexible than a dual-head system with respect to acquisition time distributions. Therefore, a second NUS protocol was designed (NUS II), which can only be executed with a single-head SPECT system (Figure 1, fourth column). In this protocol, the 360° arc is divided into four parts of 90° each. Half of the total acquisition time is spent at the 90° arc closest to the VOI, 7/32th of the total time is spent at each of the two adjacent 90° arcs and 1/16th of the time is spent at the opposite 90° arc.

For all acquisition protocols and total acquisition times, the view times per angle are indicated in Table 1.

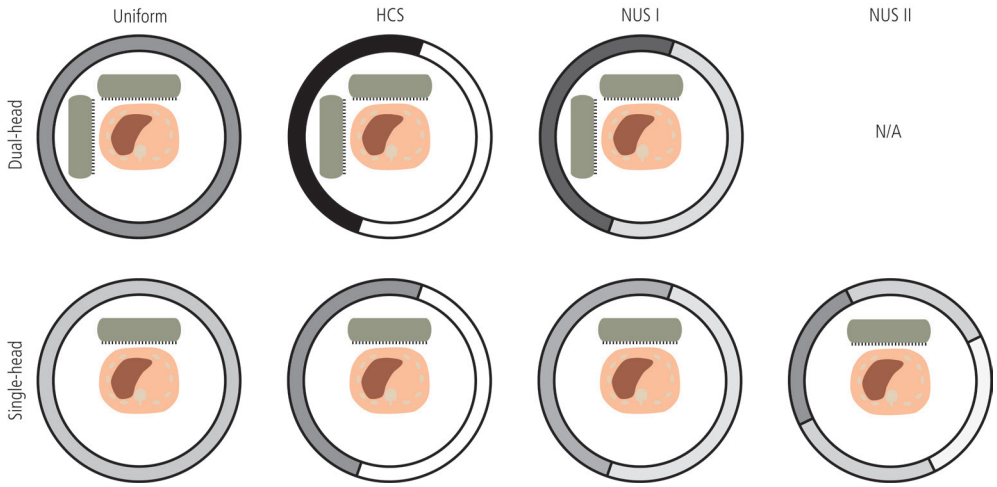

Figure 1: Schematic overview of evaluated acquisition protocols for fast liver SPECT. The grayscale ring indicates the acquisition time distribution: a darker colour means more time is spent at that angle (exact times can be found in Table 1). Upper row: dual-head system, lower row: single-head system. Column 1: uniform projection-time distribution; column 2: half-circle SPECT (HCS); column 3: non-uniform SPECT I (NUS I); column 4: non-uniform SPECT II (NUS II).

Table 1: View time per angle [s/view] for the different time windows (indicated in gray in Figure 1) for all acquisition protocols and total acquisition times, given a 360° acquisition and 120 projections. For example, 2 – 0 with the dual-head HCS protocol and 1 min total acquisition time means 2 seconds is spent at each view in the first 180° arc and 0 seconds is spent at each view in the second 180° arc.

Total acquisition time	**Dual-head**			**Single-head**			
	Uniform	**HCS**	**NUS I**	**Uniform**	**HCS**	**NUS I**	**NUS II**
1 min	1	2 – 0	1.5 – 0.5	0.5	1 – 0	0.75 – 0.25	1 – 0.44 – 0.13
2 min	2	4 – 0	3 – 1	1	4 – 0	1.5 – 0.5	2 – 0.88 – 0.25
5 min	5	10 – 0	7.5 – 2.5	2.5	5 – 0	3.25 – 1.25	5 – 2.19 – 0.63
10 min	10	20 – 0	15 – 5	5	10 – 0	7.5 – 2.5	10 – 4.38 – 1.25
30 min	30	60 – 0	45 – 15	-	-	-	-

Simulation of SPECT images

Phantom

The digital four-dimensional extended cardiac-torso (XCAT) phantom (18) was used to provide a realistic anthropomorphic model suitable for SPECT simulations. All simulations were performed with a normal weight male (BMI: 25.8 kg/m^2) phantom without breathing motion. To investigate the influence of lesion size and location on image quality obtained with the different protocols and acquisition times, lesions of 10 and 20 mm in diameter were positioned in each of the eight liver segments (Figure 2). To avoid scatter counts from non-target lesions into the target lesion, sixteen different phantom configurations were generated based on lesion size and position. A total activity of 150 MBq ^{99m}Tc was simulated, which is the standard amount of ^{99m}Tc administered to radioembolisation patients during the pre-treatment procedure (1). A realistic radioembolisation patient was simulated by setting the tumour/non-tumour (T/N) activity concentration ratio to 8 and assuming a lung shunt fraction of 5% (19).

Simulations

A total of 120 projections acquired with a low-energy-high-resolution (LEHR) parallel hole collimator were simulated with the Utrecht Monte Carlo System (UMCS), including scatter and attenuation (20,21). The energy window was set to 140 keV ± 7.5%. Depth-dependent collimator response was modelled with kernels based on a Monte Carlo radiation transport code (MCNPX) model (22) of a Symbia T SPECT/CT system (Siemens Healthcare, Erlangen, Germany) (21,23). Projections were simulated on a matrix of 128 x 128 pixels, with a pixel size of 4.8 x 4.8 mm^2. For each combination of phantom, protocol, scan geometry (single- or dual-head) and total acquisition time (Table 2), 25 projection measurements were created by adding Poisson noise, scaled by the time per projection and the total activity, to the simulated noise-free projections.

UMCS was used to reconstruct the simulated projections into a volume of 128 x 128 x 128 voxels with a voxel size of 4.8 x 4.8 x 4.8 mm^3 using an ordered subset expectation-maximisation (OSEM) algorithm with 10 iterations and 8 subsets, including attenuation and Monte Carlo scatter correction, and depth-dependent resolution recovery (20,21).

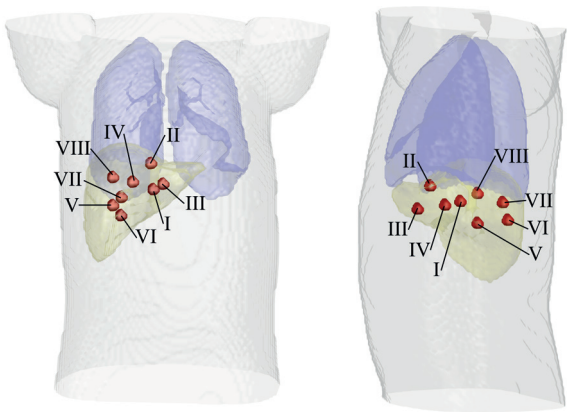

Figure 2: Rendering of the phantom (anterior and right lateral view) used in the simulations, with the lungs in blue and the liver in yellow. The red dots indicate the locations of the lesions in the different lesion segments. Note that in each phantom realisation, only one lesion was positioned in the liver.

Table 2: Overview of varied parameters. Each combination of parameters was simulated, except the non-uniform SPECT II protocol (single-head only) and 30 min acquisition time (dual-head only). This yielded a total number of 496 combinations for which 25 different noise realisations were simulated. Parameter values in **bold** indicate reference values.

Acquisition parameters	Scan geometry	Protocol	Total acquisition time
	Single-head	**Uniform**	1 min
	Dual-head	Half-circle SPECT	2 min
		Non-uniform SPECT I	5 min
		Non-uniform SPECT II	10 min
			30 min
Phantom parameters	**Lesion size**	**Lesion location**	
	10 mm diameter	Eight locations (**VIII**)	**LSF: 5%**
	20 mm diameter		**T/N ratio: 8:1**

To reconstruct projections of non-uniform projection-time protocols, viewing time per angle was incorporated in the reconstruction as follows:

$$f_i^{k+1} = \frac{f_i^k}{\sum_j t_j} \cdot \frac{1}{\sum_j p_{i,j} \cdot n_j} \cdot \sum_j \left[p_{i,j} \cdot \frac{s_j}{\sum_i p_{i,j} \cdot f_i^k \cdot t_j} \right].$$

Here, f_i^k is the k^{th} estimate of the activity distribution at voxel i, s_j is the measured projection at angle j, $P = \{p_{i,j}\}$ is the system matrix, t_j is the duration of the projection-image acquisition at angle j and

$$n_j = \begin{cases} 1, & t_j \neq 0 \\ 0, & t_j = 0 \end{cases}.$$

The factor n_j ensures the normalisation map complies with the number of angles imaged. Since system sensitivity was incorporated in the depth-dependent collimator response of the forward projector, this resulted in quantitative reconstructions with voxel values representing activity concentration in Bq/voxel.

Image quality metrics

To compare the different protocols and acquisition times, image quality was evaluated in terms of contrast-to-noise ratio (CNR). In addition, the following dosimetry related metrics were calculated: the activity recovery coefficient (ARC), the tumour/non-tumour (T/N) ratio and estimated lung shunt fraction (LSF). Accurate determination of these metrics is a first step towards the calculation of absorbed doses in gray. For all metrics, the mean and standard deviation over the 25 simulated noise realisations were reported.

For all metrics except LSF, a lesion VOI and a background VOI are needed. These VOIs were created using the activity map of the XCAT phantom. Lesion VOIs were defined as all lesion voxels of the phantom. The background VOI was defined as all liver voxels of the phantom, excluding the lesion voxels. For each combination of lesion position and size, a specific background VOI was generated. To exclude voxels affected by collimator blurring and partial volume effects, the background VOI was eroded by 1 cm.

For the calculation of the LSF, dedicated liver and lung VOIs were created using the activity map of the XCAT phantom. The liver VOI was equal to all liver voxels of the phantom and the lung VOI was equal to all lung voxels of the phantom. Both VOIs were dilated by 1 cm to include voxels affected by collimator blurring and partial volume effects. Voxels present in both the lung VOI and the liver VOI were attributed to the liver VOI.

To achieve an accurate lesion delineation which can be used to calculate dose distributions in radioembolisation, small accumulations of activity in regions with background activity should be detectable. Visibility of the lesion was therefore quantified with the contrast-to-noise ratio (CNR) as:

$$CNR = \frac{C_{\mathrm{l}} - C_{\mathrm{b}}}{\sigma_{\mathrm{b}}},$$

with C_{l} the mean activity concentration in the lesion VOI, C_{b} the mean activity concentration in the background VOI and σ_{b} the standard deviation of the activity concentration in the background VOI. According to the Rose criterion, a lesion can be reliably distinguished from the background if the CNR is larger than 5 (24).

Quantitative reconstruction accuracy was assessed by calculating the activity recovery coefficient (ARC) as:

$$ARC = \frac{A_{\mathrm{VOI}}}{A_{\mathrm{GT}}} \cdot 100\%,$$

with A_{VOI} the total activity in the reconstructed VOI (liver or lesion) and A_{GT} the ground truth total activity as simulated in the phantom.

When dose planning is based on the partition model, T/N ratio is used in the estimation of the expected tumour and healthy liver dose, given the distribution of ^{99m}Tc-MAA in the liver and the lungs (25). T/N ratio was calculated as:

$$T/N = \frac{A_{\mathrm{l}}}{A_{\mathrm{b}}},$$

with A_{l} the mean activity concentration in the lesion VOI and A_{b} the mean activity concentration in the background VOI. In the partition model, this ratio is subsequently used to calculate the activity to be administered as follows (26):

$$A_{\mathrm{adm}} = \frac{D_{\mathrm{liver}}(T/N \cdot M_{\mathrm{lesion}} + M_{\mathrm{liver}})}{D_{\mathrm{abs}}\left(1 - \frac{LSF}{100}\right)},$$

with A_{adm} the activity [GBq] to be administered, D_{liver} the maximum allowed dose to the liver tissue [Gy], T/N the tumour/non-tumour ratio, M_{lesion} the mass of the lesion [kg], M_{liver} the mass of the liver [kg], D_{abs} the assumed absorbed dose per GBq per kilogram tissue (50 J/GBq) and LSF the lung shunt fraction [%].

Lung shunt fraction (LSF) is defined as the percent of the administered activity shunting to the lungs and is important for estimating the dose on the lungs, which limits the therapeutic activity given to the patient (27). LSF was calculated as:

$$LSF = \frac{A_{\mathrm{lung}}}{A_{\mathrm{lung}} + A_{\mathrm{liver}}} \cdot 100\%,$$

with A_{lung} the total activity in the lung VOI and A_{liver} the total activity in the liver VOI. Note that a different set of VOIs is used in the LSF calculation than in the calculation of the other image quality metrics.

Phantom experiment

To further verify the effect of shortening the total acquisition time on image quality and dosimetry, experimental SPECT/CT acquisitions of an anthropomorphic phantom (Model ECT/TOR/P) were performed. A sphere of 20 mm diameter was positioned inside the liver and was filled with 3 MBq of ^{99m}Tc. The rest of the liver compartment was filled with 140 MBq of ^{99m}Tc, resulting in a T/N ratio of 7.6:1. In addition, the lungs contained 10 MBq of ^{99m}Tc, giving an LSF of 6.7%.

SPECT/CT scans were performed on a Symbia T SPECT/CT system (Siemens Healthcare, Erlangen, Germany) with a LEHR collimator. Scans with a uniform projection-time protocol with a total acquisition times of 1, 2, 5, 10 and 30 minutes, respectively, were acquired. In addition, scans of 0.5 and 2.5 minutes were acquired to simulate uniform projection-time protocol single-head acquisitions of 1 and 5 minutes, respectively. Projections were acquired at 120 angles (60 views) on a matrix of 128 x 128 pixels, a zoom factor of 1 and with the energy window positioned at 140 keV ± 7.5% and a lower scatter window at 118 keV ± 7.5%.

All acquired projection sets were reconstructed with the clinical reconstruction protocol (3DOSEM, 6 iterations, 8 subsets, attenuation correction, dual-window scatter correction, 5.0 mm Gauss filter) and with UMCS, using the same reconstruction parameters as described above (attenuation correction, Monte Carlo scatter correction), to investigate the effect of reconstruction software on image quality and dosimetry metrics. In conformity with the clinical reconstructions, the UMCS reconstructions used 6 iterations and were smoothed with a 5.0 mm Gauss filter.

VOIs were manually delineated on the low dose CT images, after which masks for lesion, background, lungs and liver were generated in the same fashion as for the digital phantom. Subsequently, CNR, ARC, T/N ratio and LSF were calculated for each combination of scan duration and reconstruction method. Because the clinical reconstruction protocol resulted in voxel values representing counts instead of Bq/voxel, the ARC for these reconstructions were calculated relative to the clinical reconstruction of the 30-minutes SPECT scan.

Statistical analysis

The calculated image quality metrics were compared against the corresponding reference value (bold in Table 2) to investigate whether the change of a certain parameter had a significant effect on the evaluation of the pre-treatment scan. For example, the difference in CNR for the uniform protocol (reference) and the HCS protocol was calculated for all of the 3600 combinations of the other parameters. To assess the relevance of the change, Cohen's d was calculated as follows:

$$d = \frac{m_{\text{diff}}}{\sigma_{\text{diff}}},$$

with m_{diff} the mean of the differences and σ_{diff} the standard deviation of the differences (28). Cohen proposed to assess the values as follows: small effect (d < 0.20), medium effect (around 0.50) and large effect (d > 0.80) (28). In this study, we considered values of d < 0.50 unlikely to have a relevant effect on the evaluation of the pre-treatment procedure. Consequently, data were averaged over parameters that did not have a significant effect.

Results

Simulations

Counts in projections

Usage of the HCS protocol resulted in 35% more counts in the projections than with the uniform projection-time protocol (d = 0.72). Lesion size (d = 0.36) and lesion location (d < 0.49 for all locations) did not influence the number of counts in the projections. The NUS I and NUS II protocols resulted in 18% (d = 0.71) and 22% (d = 1.29) more counts than the uniform projection-time protocol, respectively (Figure 3). Similar ratios were found for the other simulated total acquisition times.

Reconstructions

Reconstructed images of the uniform projection-time protocol and the NUS II protocol obtained with a single-head scanner and the phantom with a 20 mm lesion in segment VII are shown in Figure 4. For comparison purposes, a reconstructed image of the simulation of the current clinical protocol (uniform, 30 min, dual-head) is also shown. As expected, visibility of the lesion and overall image quality deteriorated with shorter acquisition times.

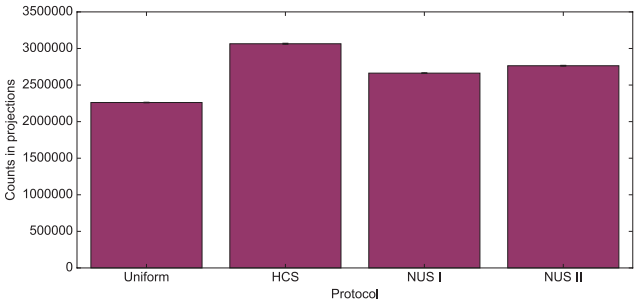

Figure 3: Number of counts in projections obtained with the different protocols for a single-head geometry with a total acquisition time of 10 minutes, averaged over all lesion positions and sizes. Error bars (too small to be visible) indicate standard deviations.

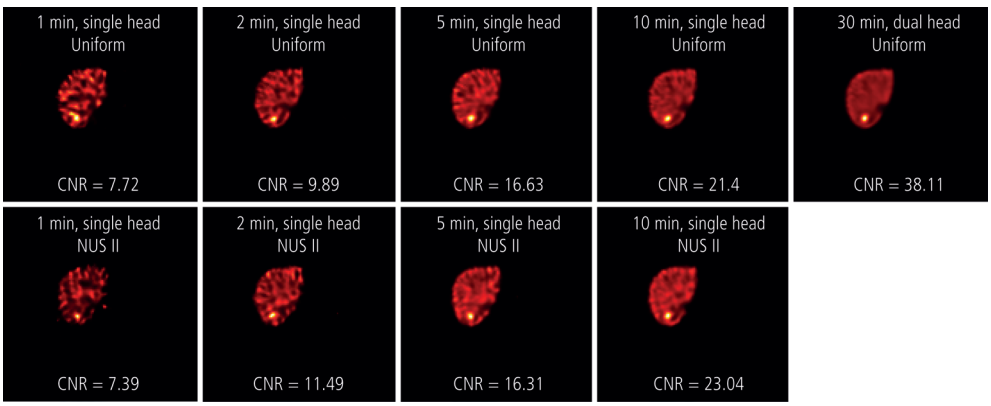

Figure 4: Reconstructed images of the uniform (upper row) and NUS II (lower row) protocol obtained with a single-head scanner and the phantom with a 20 mm lesion in segment VII. For comparison purposes, a reconstructed image of the simulation of the current clinical protocol (uniform, dual-head, 30 min) is also shown.

Contrast-to-noise ratio

Although the use of the non-uniform protocols increased CNR slightly, the effect was considered small (HCS: d = 0.27, m_{diff} = 0.45; NUS I: d = 0.36, m_{diff} = 0.50; NUS II: d = 0.15, m_{diff} = 0.20). CNR decreased significantly with decreasing acquisition times ($2.24 < d < 2.47$) and was lower for the 10 mm lesion than for the 20 mm lesion (d = 2.00, m_{diff} = -10.59) (Figure 5a). The lowest CNR was found consistently in segment I (d = 1.22, m_{diff} = -2.47), whilst segments II and III showed the highest CNR (II: d = 0.64, m_{diff} = 1.06; III: d = 0.74, m_{diff} = 1.23). According to the Rose criterion (CNR > 5), the 20 mm lesion was distinguishable from the background in all liver segments for scans of 1 minute and longer, both with a dual- and a single-head system. The 10 mm lesion reached a CNR larger than 5 in all liver segments with a dual-head scan of 5 minutes and longer, whilst a single-head scan had to take at least 10 minutes.

Since CNR is a combination of contrast and noise, more insight into the effect of non-uniform projection-time protocols can be obtained by looking at these components separately. A more pronounced advantage of the non-uniform projection-time protocols was seen when only the noise in the background VOI (σ_b) was taken into account, showing a substantial reduction in the background noise (HCS: d = 1.28, m_{diff} = -247.36; NUS I: d = 0.86, m_{diff} = -97.21; NUS II: d = 0.59, m_{diff} = -72.82) (Figure 5b). Lesion size and lesion location did not have an effect on the noise level (d < 0.27). Contrast, however, was lower when non-uniform protocols were used compared to the uniform protocol, diminishing the advantage of non-uniform projection-time protocols with respect to CNR.

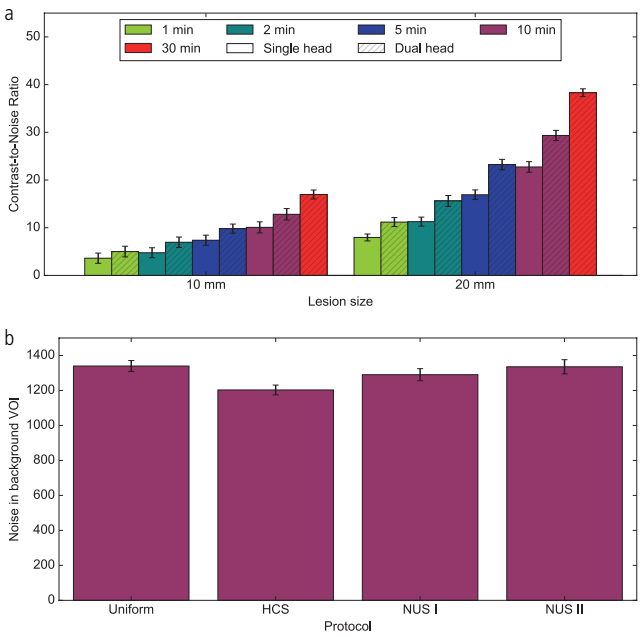

Figure 5: (a) CNR values for different acquisition times for the lesion in segment VIII (reference), averaged over all protocols. (b) Noise levels for the different protocols for a single-head geometry with a total acquisition time of 10 minutes, averaged over all lesion positions and sizes. Error bars indicate standard deviations.

Activity recovery coefficient

Ideally, an ARC of 100% would be obtained, meaning that all activity in the phantom is quantitatively correctly reconstructed. Activity recovery in the background VOI showed a consistent minor overestimation of 2 percentage points (pp) for all lesion sizes, lesion positions, acquisition times and acquisition protocols. Activity recovery in the lesion was lower for the 10 mm lesion than for the 20 mm lesion (d = 3.05, m_{diff} = -24.85 pp) (Figure 6). Shortening acquisition time did not influence mean activity recovery, although it increased the standard deviation (0.00 < d < 0.09). Lowest activity recovery was found for the lesion in segment I (d = 1.18, m_{diff} = -10.56 pp), highest activity recovery was achieved for lesions in segment II or III (II: d = 0.56, m_{diff} = 4.45 pp; III: d = 0.57, m_{diff} = 4.40 pp). Usage of non-uniform projection-time protocols did not improve activity recovery coefficients. On the contrary, the HCS protocol decreased ARC slightly for almost all lesion positions (d = 0.27, m_{diff} = -3.24 pp), while usage of the NUS I or NUS II protocol led to similar ARC values as the uniform projection-time protocol (NUS I: d = 0.01, m_{diff} = 0.05 pp; NUS II: d = 0.00, m_{diff} = -0.00 pp).

T/N ratio

For all lesion sizes, positions and acquisition times, the T/N ratio was lower than in the ground truth (8:1) due to partial volume effects and incomplete activity recovery. The same trends as for activity recovery were seen, with lower T/N ratios for the 10 mm lesion than for the 20 mm lesion in all segments (d = 5.65, m_{diff} = -2.04) and a reduced T/N ratio in segment I compared to segment VIII (d = 1.23, m_{diff} = -0.48) (Figure 7). Similarly, usage of non-uniform projection-time protocols did not improve T/N ratio (HCS: d = 0.46, m_{diff} =-0.12; NUS I: d = 0.01, m_{diff} = 0.00; NUS II: d = 0.02, m_{diff} = -0.01). The T/N ratio decreased slightly with the HCS protocol. This is linked to the lower ARC in the HCS protocol.

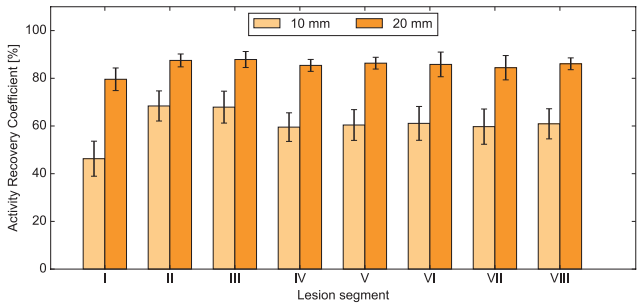

Figure 6: ARC values for the 10 and 20 mm lesion in segment I to VIII, averaged over all protocols and acquisition times. Ideally, a value of 100% would be obtained. Error bars indicate standard deviations.

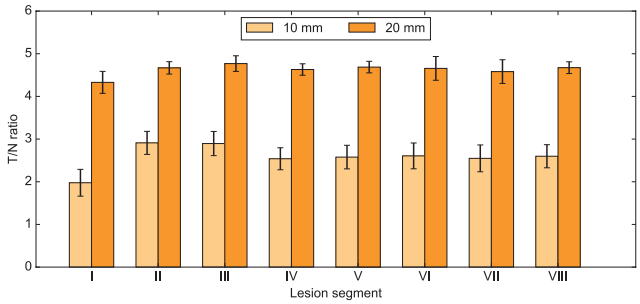

Figure 7: T/N ratios for the 10 and 20 mm lesion in segments I to VIII, averaged over all protocols and acquisition times. Ideally, a T/N ratio of 8 would be obtained. Error bars indicate standard deviations.

Lung shunt fraction

No influence of lesion size or location was seen in the estimated lung shunt fraction (d < 0.08). Shortening acquisition times did have an effect on the LSF estimations (0.51 < d < 1.17), but the mean differences were small and unlikely to affect clinical decisions (m_{diff} < 0.12 pp) (Figure 8a). The HCS protocol resulted in lower LSF estimates (d = 1.21, m_{diff} = -0.11 pp) compared to the uniform projection-time protocol, the other non-uniform projection-time protocols did not influence LSF estimates (NUS I: d = 0.07, m_{diff} = -0.01 pp; NUS II: d = 0.30, m_{diff} = -0.04 pp) (Figure 8b). In all cases, LSF was estimated accurately, with a difference of less than 0.5 pp with the ground truth of 5%.

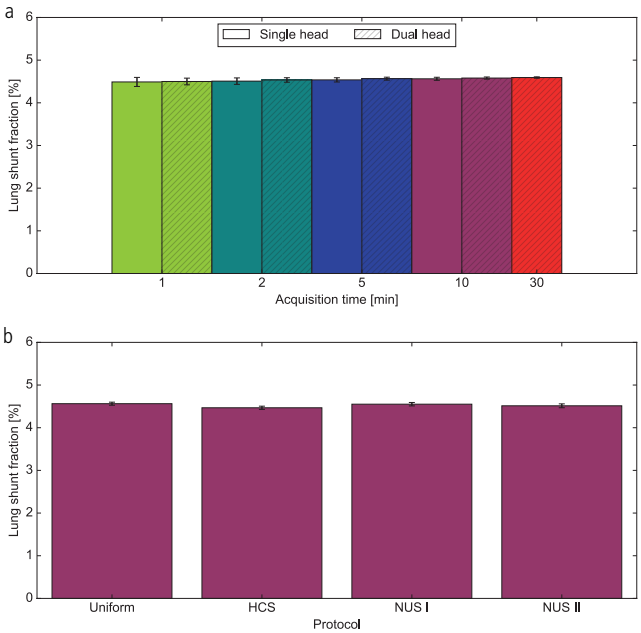

Figure 8: (a) Estimated LSF averaged over all lesion positions and sizes for different acquisition times. (b) Estimated LSF obtained from the different protocols with a single-head scanner and a total acquisition time of 10 minutes, averaged over all lesion positions and sizes. An LSF of 5% was simulated in the phantom. Error bars indicate standard deviations.

Phantom experiment

Image quality measured with the physical phantom showed similar behaviour in relation to acquisition times as our simulations. In general, the results of image reconstructions of the physical phantom were comparable to those of the Monte Carlo simulations.

The clinical reconstruction method resulted in slightly lower CNR values than the Monte Carlo reconstructions (Figure 9a). Activity recovery in the background VOI showed an overestimation of approximately 4 pp for all acquisition times. Activity recovery in the lesion was stable at approximately 56% for all acquisition times (data not shown). In the clinical reconstructions, activity recovery was stable with respect to the reconstruction of the 30 minutes scan in both the background and the lesion. For the Monte Carlo reconstructions, T/N ratios were comparable to the digital phantom (Figure 9b). However, clinical reconstructions resulted in slightly lower T/N ratios than the Monte Carlo reconstructions. LSF was stably estimated at approximately 6%, with a maximum deviation of 1 pp compared with the ground truth of 6.7%, regardless of reconstruction method and acquisition time.

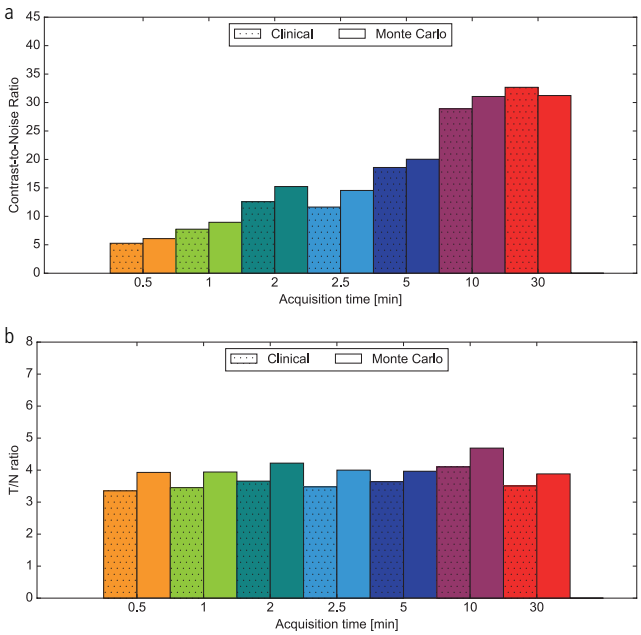

Figure 9: Comparison between clinical and Monte Carlo reconstructions of the phantom experiment: (a) CNR values and (b) T/N ratios. Ideally, a T/N ratio of 7.6 would be obtained.

Discussion

Fast and accurate dosimetry in the interventional suite has the potential of shortening treatment times and improving treatment accuracy. The aim of this study was to investigate the feasibility of acquiring fast liver SPECT scans without compromising the evaluation of the pre-treatment procedure for radioembolisation dosimetry and treatment planning. In addition, the potential benefit of three non-uniform projection-time acquisition protocols was evaluated. The results of the simulations were verified with a phantom experiment.

Fast quantitative liver SPECT images should be of sufficient quality to reliably calculate metrics required for treatment planning in radioembolisation. In clinical practice, T/N ratio and LSF estimation are the most important metrics as they are used in the partition model (25). The results show that acquisition times can be as short as 1 minute for dosimetric quantities based on whole organ VOIs (i.e. ARC, T/N ratio and LSF) when tumour delineations are known from pre-treatment CT or magnetic resonance imaging (MRI), whilst still giving similar results as the current clinical practice. This is in accordance with the findings presented by Vanhove et al (29), where the effect of shortened acquisition time on whole organ dosimetry after administration of Indium-111 was investigated. As expected, shortening acquisition times reduced image quality in terms of CNR. Acquisition times of at least 10 minutes were needed to reliably distinguish the simulated lesions from the background. CNR is, however, of minor importance for assessment of the ^{99m}Tc-MAA activity during radioembolisation.

We did not find any benefit from using non-uniform projection-time acquisition protocols. The HCS protocol was based on clinically used dedicated cardiac scanners, where scanning 180° is common clinical practice. The HCS protocol resulted in 35% more counts than obtained with the uniform protocol. However, those extra counts did not translate directly into better image quality. Although noise levels decreased markedly, CNR values, T/N ratios and activity recovery coefficients did not change significantly. Theoretically, a 180° acquisition should be sufficient for reconstruction when the system matrix is exactly known. However, due to attenuation, and to a lesser extent due to scatter, depth-dependent collimator-detector response and noise, projections from a 180° acquisition hold less information than projections of a 360° acquisition. This results in less accurate reconstructions with the HCS protocol. In addition, reconstructions of projections from a 180° acquisition converge more slowly and to lower activity concentration values than reconstructions of a 360° acquisition. In cardiac imaging, it was shown that a 180° arc was related to inhomogeneities and quantitation errors (30–32). This is in line with our results, showing no significant difference in image quality and dosimetric accuracy in images obtained with the HCS protocol compared with images obtained with the uniform projection-time protocol. The NUS I and II protocols were based on results found in literature (14–17). Similarly as for the HCS protocol, the number of counts increased, but this did not result in better image quality.

Several studies in the literature showed improvement of CNR values upon usage of non-uniform projection-time protocols (14–17). In these studies, the acquisition protocol was optimised to a specific phantom. Although the protocols used in our study were based on these optimal protocols, where more time was spent at angles with a high count rate, our results did not show a substantial increase in CNR values. This could be because the optimised protocols used highly varying acquisition time distributions, while our protocols consisted of at most four different time windows. But more importantly, the largest improvement in image quality was found when quite

simplistic phantoms with heavily asymmetrical activity distributions were used. The more realistic phantom of our study had a less asymmetrical activity distribution, potentially lessening the effect of non-uniform acquisition protocols.

The dependence of image quality and dosimetry metrics on acquisition time was not significantly influenced by the position of the lesions, although the lowest CNR, ARC and T/N ratios were consistently found for lesions in segment I. Segment I, the caudate lobe, is located centrally at the posterior side of the liver. Consequently, counts originating from lesions in this segment traverse more tissue and thus undergo more attenuation. This resulted in a lower CNR, ARC and T/N ratio compared with lesions in other segments.

Image quality is a function of reconstruction parameters and the number of counts in the projections. In this study, the effect of the latter is investigated by shortening acquisition times and comparing single- and dual-head systems. With equal total acquisition times, a single-head system results in half the counts of a dual-head system, lowering image quality. The number of counts in the projections is also influenced by the activity administered to the patient. Equivalent image quality can be obtained in half the time when the activity is doubled. However, patient dose considirations limit increasing administered activity, this scenario is therefore not evaluated in this study.

Computation time of a single reconstruction with UMCS on a single-threaded regular desktop computer is about 30 minutes. This is unacceptably long for inclusion in a single-session procedure. However, the differences found between the clinical reconstructions of the physical phantom and our Monte Carlo-based UMCS reconstructions were small and unlikely to affect clinical decisions. The results of this paper will therefore also be valid for reconstruction methods using window-based scatter correction methods instead of Monte Carlo-based scatter correction as is used in UMCS. Accordingly, the standard reconstruction protocol, which takes only several minutes, is sufficient to reconstruct the ^{99m}Tc-MAA distribution in radioembolisation procedures. Monte Carlo-based scatter correction might, however, be needed when post-treatment scans with other isotopes having more complex emission spectra, such as holmium-166 or yttrium-90, are evaluated.

The number of iterations used in iterative reconstruction is a trade-off between quantification and noise amplification (33). In our simulations, we were primarily interested in quantification, leading to the choice of using 10 iterations. In clinical practice, however, quantification is often less critical than noise amplification; reconstructions are therefore stopped after fewer (e.g. 6) iterations. This number of iterations was also used in our physical phantom experiment to verify the results with standard clinical protocols.

We did not incorporate breathing motion into our analysis in order to solely study the effects of shortening acquisition times and using non-uniform projection-time protocols. It is expected that breathing motion will deteriorate dosimetric accuracy (34). However, the amount of deterioration due to breathing motion is expected to be independent of total acquisition time.

To limit the number of varied parameters in this study, LSF and T/N ratio were fixed. We expect LSF to be stably estimated at short acquisition times (12). Due to the large ROIs used in LSF estimation, the impact of increased noise is negligible when shortening acquisition times. Limited research on the effect of a lower T/N ratio showed that similar behaviour with respect to acquisition time and protocol can be expected.

We further acknowledge the limitation of a simulation study being of restricted realism. In clinical practice, wide variations in lesion size, position and body type will be seen. By simulating two rather small lesions at different positions in the liver, we sought to recapitulate part of the clinical variation in this study. In addition, a simulation study has the benefit of having a ground truth to which results can be compared and the possibility of simulating many acquisition times. In a clinical study, such an extensive search for possible protocols and acquisition times will not be possible.

This study focussed specifically on accelerating nuclear imaging at the interventional suite for liver radioembolisation procedures. Nevertheless, the results are equally valid for shortening acquisition times of scans generally. Specifically, scans for other purposes than radioembolisation using similar metrics derived from large ROIs, thus cancelling the noise increase related to shortening acquisition times, could potentially be executed in shorter times than in current clinical practice.

Conclusion

The effect of shortening acquisition times for fast quantitative liver SPECT on image quality and dosimetric accuracy was investigated, and simulations were verified with a phantom experiment. The results showed that shortening acquisition times decreased CNR, which could be slightly counteracted by using non-uniform projection-time protocols. Dosimetric accuracy was not affected by shortening acquisition times. Usage of a non-uniform projection-time protocol did not improve dosimetric accuracy. Therefore, acquisition times can be safely lowered to 10 minutes with a uniform projection-time protocol for the assessment of the pre-treatment procedure in the interventional suite, solving one of the major issues related to single-session procedures in radioembolisation.

References

1. AJAT Braat, MLJ Smits, MNGJA Braat, AF van den Hoven, JF Prince, HWAM de Jong, et al., ^{90}Y Hepatic Radioembolization: An Update on Current Practice and Recent Developments, J. Nucl. Med., 2015, 56(7):1079–87.
2. A Kennedy, D Coldwell, B Sangro, H Wasan, and R Salem, Radioembolization for the Treatment of Liver Tumors, Am. J. Clin. Oncol., 2012, 35(1):91–9.
3. MLJ Smits, M Elschot, DY Sze, YH Kao, JFW Nijsen, AH Iagaru, et al., Radioembolization Dosimetry: The Road Ahead, Cardiovasc. Intervent. Radiol., 2015, 38(2):261–9.
4. YH Kao, AE Hock Tan, MC Burgmans, FG Irani, LS Khoo, RH Gong Lo, et al., Image-Guided Personalized Predictive Dosimetry by Artery-Specific SPECT/CT Partition Modeling for Safe and Effective ^{90}Y Radioembolization, J. Nucl. Med., 2012, 53(4):559–66.
5. VL Gates, KG Marshall, K Salzig, M Williams, RJ Lewandowski, and R Salem, Outpatient Single-Session Yttrium-90 Glass Microsphere Radioembolization, J. Vasc. Interv. Radiol., 2014, 25(2):266–70.
6. A Gabr, JR Kallini, VL Gates, R Hickey, L Kulik, K Desai, et al., Same-day ^{90}Y radioembolization: implementing a new treatment paradigm, Eur. J. Nucl. Med. Mol. Imaging, 2016, 43(13):2353–9.
7. E Garin, J Edeline, and Y Rolland, High Impact of Preferential Flow on ^{99m}Tc-MAA and ^{90}Y-Loaded Microsphere Uptake Correlation, J. Nucl. Med., 2016, 57(11):1829–30.
8. J Gardiazabal, M Esposito, P Matthies, A Okur, J Vogel, S Kraft, et al., Towards Personalized Interventional SPECT-CT Imaging, In: Lecture Notes in Computer Science (including subseries Lecture Notes in Artificial Intelligence and Lecture Notes in Bioinformatics). 2014, page 504–11.
9. T Engelen, BM Winkel, DD Rietbergen, GH KleinJan, S Vidal-Sicart, RAV Olmos, et al., The next evolution in radioguided surgery: breast cancer related sentinel node localization using a freehand SPECT-mobile gamma camera combination, Am. J. Nucl. Med. Mol. Imaging, 2015, 5(3):233–45.
10. C Beijst, M Elschot, MA Viergever, and HWAM de Jong, Toward Simultaneous Real-Time Fluoroscopic and Nuclear Imaging in the Intervention Room, Radiology, 2016, 278(1):232–8.
11. S van der Velden, C Beijst, MA Viergever, and HWAM de Jong, Simultaneous fluoroscopic and nuclear imaging: impact of collimator choice on nuclear image quality, Med. Phys., 2017, 44(1):249–61.
12. S van der Velden, R Bastiaannet, AJAT Braat, MGEH Lam, MA Viergever, and HWAM de Jong, Estimation of lung shunt fraction from simultaneous fluoroscopic and nuclear images, Phys. Med. Biol., 2017, 62(21):8210–25.
13. M Elschot, JFW Nijsen, MGEH Lam, MLJ Smits, JF Prince, MA Viergever, et al., ^{99m}Tc-MAA overestimates the absorbed dose to the lungs in radioembolization: a quantitative evaluation in patients treated with ^{166}Ho-microspheres, Eur. J. Nucl. Med. Mol. Imaging, 2014, 41(10):1965–75.

14. N Fuin, S Pedemonte, S Arridge, S Ourselin, and BF Hutton, Use of the Fisher Information Matrix to optimize the acquisition protocol for a D-SPECT system, In: 2012 IEEE Nuclear Science Symposium and Medical Imaging Conference Record (NSS/MIC). IEEE; 2012, page 2137–42.
15. LR V Pato, S Vandenberghe, and R Van Holen, Efficient optimization for adaptive SPECT systems based on local shift-invariance, In: 2012 IEEE Nuclear Science Symposium and Medical Imaging Conference Record (NSS/MIC). IEEE; 2012, page 2501–8.
16. L Cai, N Li, and LJ Meng, A prototype adaptive SPECT system with self-optimized angular sampling, In: 2011 IEEE Nuclear Science Symposium Conference Record. IEEE; 2011, page 4402–6.
17. X Zheng, and SD Metzler, Angular viewing time optimization for slit-slat SPECT, In: 2012 IEEE Nuclear Science Symposium and Medical Imaging Conference Record (NSS/MIC). IEEE; 2012. page 3521–4.
18. WP Segars, G Sturgeon, S Mendonca, J Grimes, and BMW Tsui, 4D XCAT phantom for multimodality imaging research, Med. Phys., 2010, 37(9):4902–15.
19. KP Willowson, M Tapner, and DL Bailey, A multicentre comparison of quantitative ^{90}Y PET/CT for dosimetric purposes after radioembolization with resin microspheres, Eur. J. Nucl. Med. Mol. Imaging, 2015, 42(8):1202–22.
20. FJ Beekman, HWAM de Jong, and S van Geloven, Efficient fully 3-D iterative SPECT reconstruction with Monte Carlo-based scatter compensation, IEEE Trans. Med. Imaging, 2002, 21(8):867–77.
21. HWAM de Jong, ETP Slijpen, and FJ Beekman, Acceleration of Monte Carlo SPECT simulation using convolution-based forced detection, IEEE Trans. Nucl. Sci., 2001, 48(1):58–64.
22. JS Hendricks, GW Mckinney, LS Waters, TL Roberts, HW Egdorf, JP Finch, et al., MCNPX Extensions version 2.5.0, Los Alamos National Laboratory, 2005.
23. Siemens Healthineers, Symbia S and T System Specifications, 2010.
24. A Rose, The Sensitivity Performance of the Human Eye on an Absolute Scale, J. Opt. Soc. Am., 1948, 38(2):196.
25. S Ho, WY Lau, TWT Leung, M Chan, YK Ngar, PJ Johnson, et al., Partition model for estimating radiation doses from yttrium-90 microspheres in treating hepatic tumours, Eur. J. Nucl. Med., 1996, 23(8):947–52.
26. Sirtex Medical Limited, SIR-Spheres® microspheres - Training program, North Sydney, NSW, Australia: 2004.
27. Sirtex Medical Limited, SIR-Spheres package insert (CR1507), North Sydney, NSW, Australia: 2012.
28. J Cohen, Statistical Power Analysis for the Behavioral Sciences, Biometrics, 1970, 26(3):588.
29. B He, and EC Frey, Effects of shortened acquisition time on accuracy and precision of quantitative estimates of organ activity, Med. Phys., 2010, 37(4):1807–15.
30. C Vanhove, PR Franken, M Defrise, and A Bossuyt, Comparison of 180° and 360° data acquisition for determination of left ventricular function from gated myocardial perfusion tomography and gated blood pool tomography, Eur. J. Nucl. Med. Mol. Imaging, 2003, 30(11):1498–504.

31. Y Liu, PT Lam, AJ Sinusas, and FJT Wackers, Differential Effect of 180° and 360° Acquisition Orbits on the Accuracy of SPECT Imaging : Quantitative Evaluation in Phantoms, J. Nucl. Med., 2002, 43(8):1115–25.
32. T Misaka, M Hosono, T Kudo, T Ito, T Syomura, M Uemura, et al., Influence of acquisition orbit on phase analysis of gated single photon emission computed tomography myocardial perfusion imaging for assessment of left ventricular mechanical dyssynchrony, Ann. Nucl. Med., 2017, 31(3):235–44.
33. HM Hudson, and RS Larkin, Accelerated image reconstruction using ordered subsets of projection data, IEEE Trans. Med. Imaging, 1994, 13(4):601–9.
34. R Bastiaannet, MA Viergever, and HWAM de Jong, Impact of respiratory motion and acquisition settings on SPECT liver dosimetry for radioembolization, Med. Phys., 2017, 44(10):5270–9.

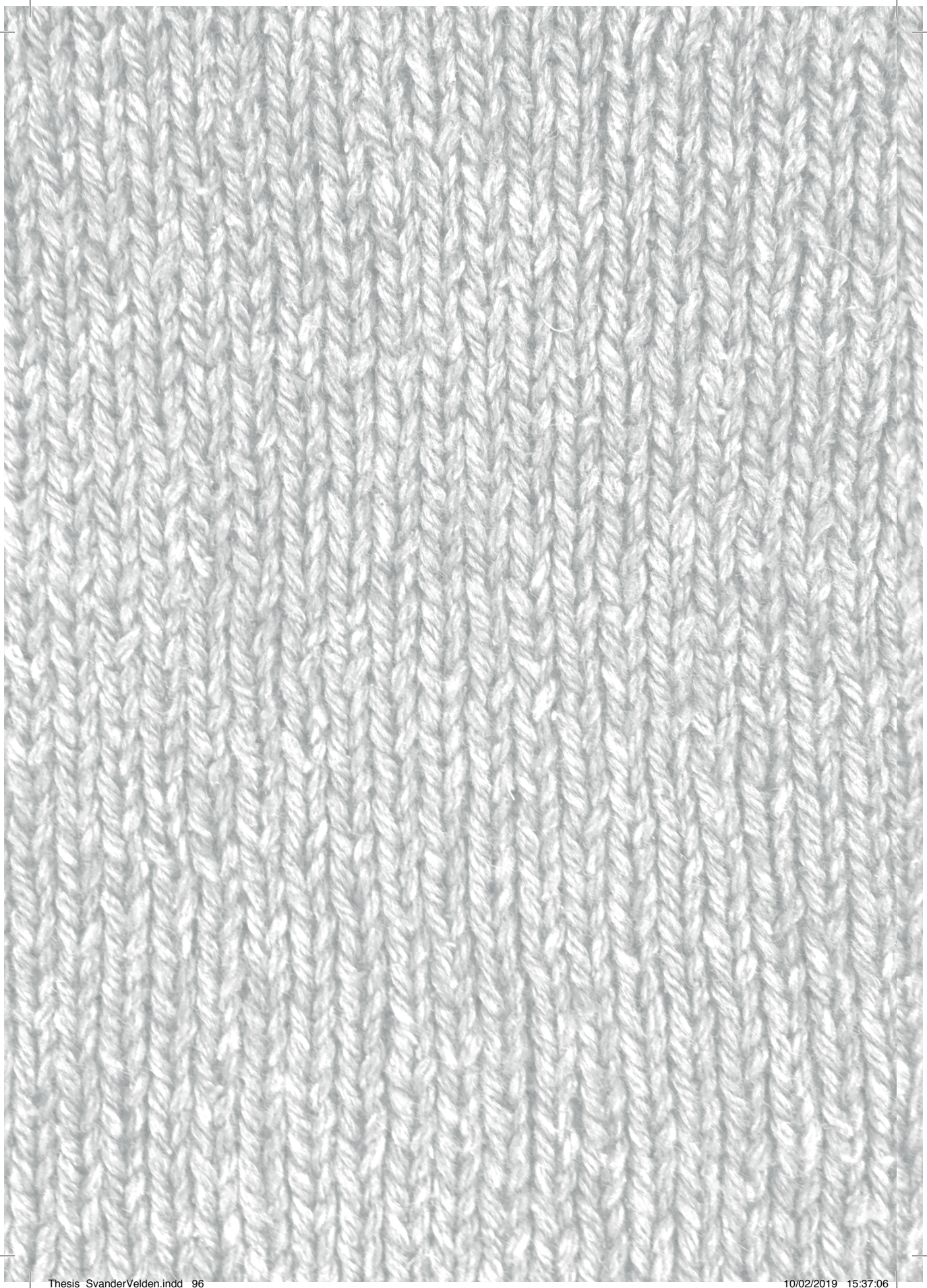

6

A pilot study on hepatobiliary scintigraphy to monitor regional liver function in yttrium-90 radioembolisation

Based on:

S. van der Velden, M.N.G.J.A. Braat, T.A. Labeur, M.V. Scholten, O.M. van Delden, R.J. Bennink, H.W.A.M. de Jong, M.G.E.H. Lam, "A pilot study on hepatobiliary scintigraphy to monitor regional liver function in yttrium-90 radioembolization", *Submitted for publication*

Abstract

Purpose

Radioembolisation is increasingly used as a bridge to resection (i.e. radiation lobectomy). It combines ipsilateral tumour control with the induction of contralateral hypertrophy to facilitate lobar resection. The aim of this pilot study was to investigate the complementary value of hepatobiliary scintigraphy (HBS) before and after radioembolisation in the assessment of the future remnant liver.

Materials and methods

Consecutive patients with liver tumours who underwent HBS before and after yttrium-90 (^{90}Y) radioembolisation were included. Regional (treated/non-treated) and whole liver function and volume were determined on HBS and CT. Changes in regional liver function and volume were correlated with the functional liver absorbed doses, determined on ^{90}Y PET/CT. In addition, the correlation between liver volume and function change was evaluated.

Results

Thirteen patients (10 HCC, 3 mCRC) were included. Liver function of the treated part declined after radioembolisation (HBS-pre: 4.0 %/min/m^2; HBS-post: 1.9 %/min/m^2; p = 0.001), while the function of the non-treated part increased (HBS-pre: 1.4 %/min/m^2; HBS-post: 2.8 %/min/m^2; p = 0.009). Likewise, treated volume decreased (pre-treatment: 1118.7 ml; post-treatment: 870.7 ml); p = 0.003), while the non-treated volume increased (pre-treatment: 412.7 ml; post-treatment: 577.6 ml; p = 0.005). Bland-Altman analysis revealed a large bias (29%) between volume decrease and function decrease in the treated part and wide limits of agreement (-7.7 – 65.6 percentage point (pp)). The bias between volume and function change was smaller (-6.0%) in the non-treated part of the liver, but limits of agreement were still wide (-117.9 – 106.7 pp).

Conclusion

Radioembolisation induces regional changes in liver function that are accurately detected by HBS. Limits of agreement between function and volume changes were wide, showing large individual differences. This implicates that HBS may have a complementary role in the management of patients treated for radiation lobectomy.

Introduction

In radioembolisation, radioactive microspheres (e.g. yttrium-90 (^{90}Y) or holmium-166 (^{166}Ho)) are injected in (branches of) the hepatic artery (1). The microspheres primarily lodge in the tumour, resulting in a high radiation absorbed tumour dose, while part of the microspheres will lodge in the "healthy" functional liver, irradiating functional liver tissue. When only part of the liver is treated, the radiation damage induces a decrease in functional liver volume in the treated part and an increase in functional liver volume in the non-treated part (2). This may have implications for subsequent treatments, including surgical resection of the involved part of the liver.

There has been a growing interest in radioembolisation as a bridge to transplant (3), and more recently as a bridge to resection (4) (i.e. radiation lobectomy). Although considered curative, many patients are excluded from surgery because of inadequate future liver remnant (FLR) volume. Radioembolisation has been found to effectively induce FLR volumetric hypertrophy, while simultaneously providing tumour control. As such, it may have benefits over portal vein embolisation (PVE), the current standard of care in these patients (4).

Currently, management of patients for radiation lobectomy is based on clinical, laboratory and imaging parameters (e.g. volumetry). Liver function is tested using blood markers (e.g. bilirubin, albumin, etc.) and clinically derived scores (e.g. Child-Pugh, MELD, etc.). Although this gives an indication of global liver function, liver function may actually be heterogeneously distributed, especially in patients with known underlying liver disease such as cirrhosis or hilar liver tumours. Hypertrophy of the FLR may therefore be insufficient for subsequent resection. A better understanding of the dose-effect relationship between radioembolisation and FLR hypertrophy, in combination with a more accurate assessment of FLR in terms of functional liver reserve, may lead to better selection, planning, and monitoring of patients who have an indication for radiation lobectomy.

Quantitative total and regional liver function can be measured using hepatobiliary scintigraphy (HBS) with technetium-99m (^{99m}Tc)-mebrofenin (Bridatec, GE Healthcare B.V., Eindhoven, the Netherlands). HBS with ^{99m}Tc-mebrofenin prior to hepatectomy adequately predicts the risk of post-surgical liver failure (5–7). A cut-off value of 2.69 %/min/m^2 (body surface area corrected ^{99m}Tc-mebrofenin uptake rate) in the FLR was reported to accurately identify patients at risk of liver failure, regardless of underlying liver disease, improving the pre-surgical work-up based on liver volumetry alone (6–8).

Two case studies (9,10) reported on the feasibility of HBS to monitor regional liver function changes after radioembolisation. The aim of this pilot study was to investigate the potential complementary value of regional function assessment in the management of radiation lobectomy by analysing the correlation between regional liver function and volume changes.

Materials and methods

Patient selection

All patients treated with radioembolisation (n = 356) between April 2012 and February 2018 were reviewed. All patients who underwent HBS pre- and post-treatment (n = 17) were evaluated. Two patients were excluded from the study, because the post-treatment HBS was acquired more than

four months after treatment (i.e. 7.5 and 17 months). One patient was excluded because of additional liver-directed treatment (i.e. radio frequency ablation) between radioembolisation and post-treatment HBS, and one patient was excluded because of treatment with ^{166}Ho microspheres and not ^{90}Y microspheres. Hence, data of 13 patients were retrospectively analysed. Three of these patients were earlier included in a case series by Braat et al. (9). The medical ethics committee waived the need for informed consent.

Radioembolisation

The regular work-up included 3-phase computed tomography (CT) and/or magnetic resonance imaging (MRI) and clinical/laboratory assessment of liver function. Prior to radioembolisation treatment, all patients underwent a safety procedure. During this procedure, a scout dose of approximately 150 MBq ^{99m}Tc macro-aggregated albumin (^{99m}Tc-MAA) (TechneScan LyoMaa, Mallinckrodt Medical, Petten, the Netherlands) was intra-arterially injected. Immediately after, ^{99m}Tc-MAA planar scintigraphy was obtained, followed by ^{99m}Tc-MAA single photon computed tomography (SPECT)/CT. The lung shunt fraction was determined on planar scintigraphy, SPECT/CT was used to detect extrahepatic depositions.

All patients were treated with ^{90}Y glass microspheres (Theraspheres®, BTG International, London, Great Britain). The administered activity was calculated using the MIRD model (11). The procedure was performed according to international guidelines (12).

Hepatobiliary scintigraphy

After intravenous administration of approximately 200 MBq of ^{99m}Tc-mebrofenin, a dual head gamma camera (Symbia T16, Siemens Healthcare, Erlangen, Germany) was positioned over the patient, including the heart and liver in the field of view. The gamma camera was mounted with a low-energy-high-resolution collimator. The acquisition protocol consisted of three phases (13). First, 36 dynamic anterior and posterior images were acquired with a frame duration of 10 seconds (matrix: 128 x 128, energy window: 140 keV ± 7.5%, zoom: 1.00). Second, a fast SPECT/CT was acquired (matrix: 128 x 128, energy window: 140 keV ± 7.5%, 64 projections, 8 s/projection, zoom: 1.45). A low-dose CT was acquired for attenuation correction and a diagnostic contrast-enhanced CT (CECT) was acquired for anatomical reference. In the last phase, 30 dynamic planar frames were acquired with a frame duration of 60 seconds (matrix: 128 x 128, energy window: 140 keV ± 7.5%, zoom: 1.00) to evaluate biliary excretion. We will refer to HBS acquired prior to treatment as HBS-pre and HBS acquired after treatment as HBS-post.

Yttrium-90 PET/CT

On the same day or the day after radioembolisation, ^{90}Y positron emission tomography (PET)/CT (Siemens Biograph mCT Time-Of-Flight (TOF)) was acquired to assess the activity distribution. Acquisition time was 15 minutes per bed position (30 minutes total) and consecutive bed positions overlapped approximately 43%. A low-dose CT (120 kVp, 40 mAs) was acquired for attenuation correction. PET images were reconstructed using the ordinary Poisson ordered subset expectation-maximisation reconstruction method, including resolution recovery, TOF information, and attenuation, random and scatter correction. Images were reconstructed using 4 iterations and 21 subsets and were smoothed with a 5 mm full width at half maximum Gaussian filter. The reconstructed voxel size was 3.9 x 3.9 x 4.0 mm^3.

Image analysis

Hepatobiliary scintigraphy

HBS was analysed similar to the method described by de Graaf et al. (13). A geometric mean dataset was calculated from the anterior and posterior dynamic projections of the first acquisition phase. Regions of interest around the total image, liver and cardiac blood pool were manually delineated. Subsequently, the ^{99m}Tc-mebrofenin uptake rate (MUR) expressed in %/min was calculated according to the method of Ekman et al. (14). The liver uptake rate was divided by the body surface area (cMUR, expressed in %/min/m^2) to correct for variability in metabolic need.

Regional liver uptake values were determined on SPECT using Simplicit^{90}Y™ software (Mirada Medical Limited, Oxford, Great Britain). The accompanying CECT was used for anatomical reference. When no CECT was obtained during HBS, the low-dose CT scan used for attenuation correction was rigidly registered to a previously acquired CECT scan or MRI (n = 2).

The whole liver and tumours were semi-automatically delineated on CECT. The hilar and extrahepatic bile ducts were excluded from the whole liver volume of interest (VOI). After rigid registration with post-treatment ^{90}Y PET/CT, the liver VOI was manually divided into a treated (excluding tumours) and non-treated part, based on the ^{90}Y distribution. The function of the treated and non-treated part was subsequently calculated as follows (7):

$$\mathrm{cMUR}_i = \frac{c_i}{c_{\mathrm{liver}}} \cdot \mathrm{cMUR}_{\mathrm{liver}},$$

where cMUR_i is the liver uptake rate in VOI i (i.e. treated or non-treated part), c_i the number of counts in VOI i, c_{liver} the number of counts in the whole liver and $\mathrm{cMUR}_{\mathrm{liver}}$ the liver uptake rate calculated from the dynamic planar images. Besides liver uptake rate, volumes [ml] of the different VOIs were also obtained from Simplicit^{90}Y™.

^{90}Y PET/CT

Functional liver parenchyma absorbed dose was calculated using Simplicit^{90}Y™. The ^{90}Y PET/CT was rigidly registered to the CECT used to analyse HBS-pre to allow the use of identical VOIs.

Statistical analysis

Statistical analysis was performed using the Python module Scipy version 0.16.0 (Python Software Foundation, https://www.python.org/). Categorical variables were described as frequencies (percentage) and continuous data was expressed as median (range). Due to the limited sample size, data did not follow a normal distribution. Therefore, differences between groups were tested with the non-parametric Wilcoxon signed-rank test. Correlation between variables was tested using the Spearman correlation coefficient ρ. Correspondence between measurements was analysed using Bland-Altman plots. A p-value of 0.05 or less was considered significant.

Results

Between April 2012 and February 2018, 13 patients (11 male, 2 female) underwent an HBS within four months before and after radioembolisation treatment, thereby fulfilling the inclusion criteria. Patient characteristics can be found in Table 1. Ten patients had hepatocellular carcinoma (HCC) and three patients had metastases from a colorectal carcinoma (mCRC). The treatment intent was

palliative in five patients and eight patients underwent radioembolisation for downstaging and/or induction of hypertrophy to enable hepatectomy. Five patients were successfully resected. The other patients had either progression of disease (n = 2) or insufficient remnant liver function for subsequent surgery (n = 1).

Table 1: Patient characteristics. Categorical variables are described as frequencies (percentage) and continuous data are expressed as median (range).

Characteristic (n=13)			**Value**
Age (y)			68 (50 – 78)
Sex	Male		11 (85%)
	Female		2 (15%)
Primary malignancy	HCC		10 (77%)
	mCRC		3 (23%)
Treatment	Lobar		11 (85%)
		Right	11 (85%)
		Left	0 (0%)
		Superselective	2 (15%)
Administered ^{90}Y activity (GBq)			2.58 (1.17 – 7.11)
Time from ^{90}Y calibration to treatment (days)†			9 (2 – 11)
Estimated number of administered microspheres†			4.81e6 (1.71e6 – 13.8e6)
Absorbed ^{90}Y dose (Gy)	Treated part		102.9 (71.8 – 125.3)
	Functional parenchyma		83.4 (71.6 – 117.0)
	Tumour		174.3 (66.7 – 335.8)
Time from HBS-pre to treatment (days)			26 (10 – 64)
Time from treatment to HBS-post (days)			92 (58 – 111)
Cirrhosis			6 (46%)
Portal hypertension			4 (31%)
Blood marker at baseline (HBS-pre)	Bilirubin (µmol/L)		9 (5 – 31)
	Albumin (g/L)		39.6 (30.2 – 46.1)
	AST (U/L)		52 (22 – 313)
	ALT (U/L)		45 (12 – 113)
	GGT (U/L)		108 (66 – 386)
	ALP (U/L)		142 (62 – 199)
	INR*		1.03 (0.82 – 1.40)
	ALBI score		-2.83 (-3.21 – -1.58)
		Grade 1	10 (77%)
		Grade 2	3 (23%)
		Grade 3	0 (0%)

Table 1 continued.

Characteristic (n=13)			Value
Blood marker at follow-up (HBS-post)	Bilirubin (μmol/L)*		10 (5 – 164)
	Albumin (g/L)		38.7 (20.2 – 45.0)
	AST (U/L)		51 (24 – 403)
	ALT (U/L)		36 (8 – 232)
	GGT (U/L)		204 (66 – 804)
	ALP (U/L)		176 (73 – 347)
	INR*		1.06 (0.84 – 1.74)
	ALBI score*		-2.60 (-3.13 – -0.55)
		Grade 1	6 (50%)
		Grade 2	3 (25%)
		Grade 3	3 (25%)

HCC = hepatocellular carcinoma, mCRC = metastatic colorectal carcinoma, AST = aspartate aminotransferase, ALT = alanine aminotransferase, GGT = gamma-glutamyltransferase, ALP = alkaline phosphatase, INR = international normalised ratio, ALBI = albumin-bilirubin

† n = 8

* n = 12

In general, treatment-induced toxicity within 3 months after treatment was mild. Median follow-up was 7 (1 – 30) months. Three patients died within 6 months after treatment, of whom two died due to radioembolisation induced liver disease (REILD) (9) and one patient died due to rapid tumour progression after radioembolisation treatment.

HBS whole liver function (pre- and post-treatment) was correlated with bilirubin (pre-treatment: Spearman ρ = -0.73, p = 0.004; post-treatment: Spearman ρ = -0.64, p = 0.025), albumin (pre-treatment: Spearman ρ = 0.63, p = 0.021; post-treatment: Spearman ρ = 0.80, p = 0.001), aspartate aminotransferase (AST) (pre-treatment: Spearman ρ = -0.68, p = 0.010; post-treatment: Spearman ρ = -0.84, p < 0.001), and international normalised ratio (INR) (pre-treatment: Spearman ρ = -0.58, p = 0.046; post-treatment: Spearman ρ = -0.51, p = 0.090). When bilirubin and albumin were combined into the ALBI score (15), the correlation was even stronger (pre-treatment: Spearman ρ = -0.75, p = 0.003; post-treatment: Spearman ρ = -0.85, p < 0.001). Whole liver volume did not correlate with bilirubin, albumin, AST, INR or any other blood value at baseline or follow-up.

HBS whole liver and regional (treated/non-treated) liver function and volume at baseline and follow-up of each individual patient can be found in Table 2. Overall, liver function of the treated part declined after radioembolisation (HBS-pre: 4.0 %/min/m^2 (1.4 – 7.2); HBS-post: 1.9 %/min/m^2 (0.4 – 3.8); p = 0.001), while the function of the non-treated part increased (HBS-pre: 1.4 %/min/m^2 (0.2 – 6.4); HBS-post: 2.8 %/min/m^2 (0.1 – 6.5); p = 0.009) (Figures 1, 2a and 3a). The increase in function of the non-treated part did not fully compensate the decline in function of the treated part. This was reflected by the decrease in whole liver function seen in most patients (HBS-pre: 6.3 %/min/m^2 (1.8 – 11.0); HBS-post: 5.1 %/min/m^2 (0.6 – 10.6); p = 0.009). In only one patient, whole liver function increased after treatment, mainly due to a large increase in liver function in the non-treated part (+98.4%), while the function of the treated part only showed a

minor decline (-5.6%). In two patients, liver function declined in the non-treated part of the liver. One had a limited liver function at baseline (whole liver: 1.8 %/min/m^2; non-treated liver: 0.2 %/min/m^2) and died four months after treatment as a result of definite REILD (9). The other patient had massive tumour progression in both the treated and non-treated part of the liver and died five months after treatment.

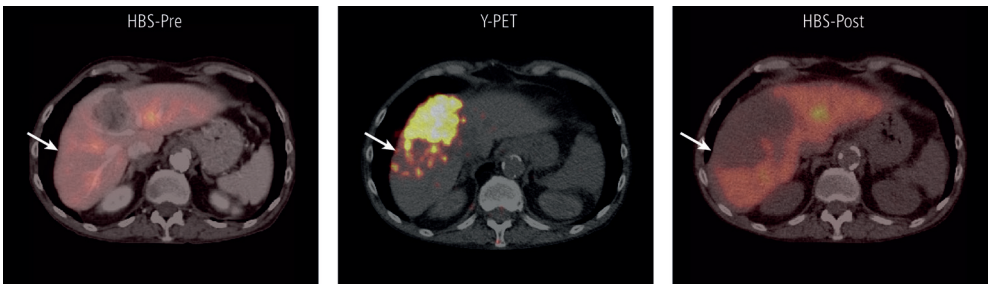

Figure 1: Example of regional liver function decline after ^{90}Y radioembolisation. Part of the functional liver parenchyma received a high absorbed dose of ^{90}Y (103 Gy on the functional liver, 231 Gy on the tumour). This was reflected on HBS-post, where that particular part of the functional liver lost most of its function (HBS-pre: 2.4 %/min/m^2; HBS-post: 0.6 %/min/m^2).

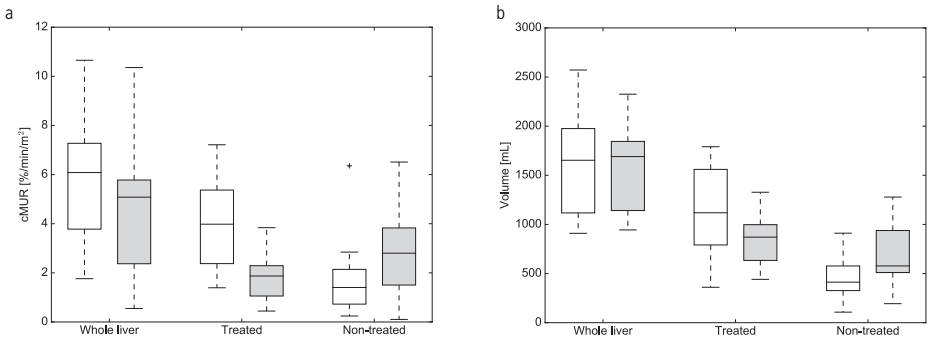

Figure 2: (a) Boxplot of liver function obtained from HBS-pre (white) and HBS-post (gray). Whole liver function declined (HBS-pre: 6.3 %/min/m^2 (1.8 – 11.0); HBS-post: 5.1 %/min/m^2 (0.6 – 10.6); $p = 0.009$). Liver function in the treated part declined (HBS-pre: 4.0 %/min/m^2 (1.4 – 7.2); HBS-post: 1.9 %/min/m^2 (0.4 – 3.8); $p = 0.001$). Liver function in the non-treated part increased (HBS-pre: 1.4 %/min/m^2 (0.2 – 6.4); HBS-post: 2.8 %/min/m^2 (0.1 – 6.5); $p = 0.009$). (b) Boxplot of liver volume pre- (white) and post-treatment (gray). Whole liver volume was stable (pre-treatment: 1683.3 ml (983.5 – 3112.5); post-treatment: 1792.4 ml (1012.4 – 3161.2); $p = 0.600$). Healthy liver volume in the treated part decreased (pre-treatment: 1118.7 ml (360.4 – 1790.8); post-treatment: 870.7 ml (441.0 – 1327.6); $p = 0.003$), while the non-treated volume increased (pre-treatment: 412.7 ml (107.2 – 910.8); post-treatment: 577.6 ml (193.5 – 1278.4); $p = 0.005$).

Table 2: Function and volume before and after radioembolisation for the thirteen included patients. The relative change is indicated between brackets.

Case		Function			Volume		
		Whole liver [%/min/m²]	Treated [%/min/m²]	Non-treated [%/min/m²]	Whole liver [ml]	Treated [ml]	Non-treated [ml]
1	Pre-RE:	2.2	1.4	0.6	1140.1	646.7	368.4
	Post-RE:	1.8 (-19.1%)	0.9 (-35.8%)	0.8 (+24.5%)	1173.4 (+2.9%)	590.3 (-8.7%)	510.3 (+35.5%)
2	Pre-RE:	3.0	2.4	0.6	2385.3	1790.8	577.5
	Post-RE:	2.4 (-20.7%)	1.5 (-34.4%)	0.8 (+29.2%)	1792.4 (-24.9%)	1240.3 (-30.7%)	528.0 (-8.6%)
3	Pre-RE:	1.8	1.5	0.2	1439.6	1152.6	258.5
	Post-RE:	0.6 (-69.2%)	0.4 (-70.7%)	0.1 (-57.1%)	1012.4 (-29.7%)	814.5 (-29.3%)	193.5 (-25.1%)
4	Pre-RE:	8.6	6.7	1.8	1683.3	1240.4	412.7
	Post-RE:	6.0 (-29.8%)	2.2 (-67.5%)	3.8 (+117.4%)	1728.4 (+2.7%)	880.7 (-29.0%)	826.3 (+100.2%)
5	Pre-RE:	5.2	2.4	2.6	1335.7	721.0	563.1
	Post-RE:	2.3 (-56.4%)	0.6 (-73.3%)	1.5 (-41.9%)	2041.2 (+52.8%)	562.9 (-21.9%)	1278.4 (+127.0%)
6	Pre-RE:	4.5	2.4	1.4	3112.5	1118.7	577.2
	Post-RE:	5.7 (+26.2%)	2.2 (-5.6%)	2.8 (+98.4%)	3161.2 (+1.6%)	870.7 (-22.2%)	819.8 (+42.0%)
7	Pre-RE:	6.3	4.0	2.1	2646.7	1746.5	825.0
	Post-RE:	5.1 (-17.9%)	2.3 (-42.5%)	2.8 (+30.8%)	2371.9 (-10.4%)	1327.6 (-24.0%)	997.8 (+20.9%)
8	Pre-RE:	11.0	4.3	6.4	983.5	360.4	549.2
	Post-RE:	10.6 (-3.1%)	3.8 (-10.7%)	6.5 (+2.4%)	1052.8 (+7.0%)	441.0 (+22.4%)	577.6 (+5.2%)
9	Pre-RE:	6.5	3.2	2.8	2212.3	1080.6	910.8
	Post-RE:	5.6 (-8.1%)	1.1 (-67.4%)	4.7 (+65.8%)	2042.2 (-7.7%)	634.7 (-41.3%)	1255.4 (+37.8%)
10	Pre-RE:	8.7	7.2	1.2	1963.6	1560.2	337.9
	Post-RE:	5.1 (-40.8%)	1.5 (-79.5%)	3.6 (+190.9%)	1880.0 (-4.3%)	920.8 (-41.0%)	938.1 (+177.6%)

Table 2 continued.

Case		Function			Volume		
		Whole liver [%/min/m^2]	Treated [%/min/m^2]	Non-treated [%/min/m^2]	Whole liver [ml]	Treated [ml]	Non-treated [ml]
11	Pre-RE:	6.3	5.4	0.8	2015.7	1650.3	326.7
	Post-RE:	4.9 (-23.3%)	2.9 (-45.6%)	1.9 (+130.7%)	1861.1 (-7.7%)	1281.5 (-22.3%)	563.8 (+72.6%)
12	Pre-RE:	7.3	6.5	0.7	1120.3	1009.5	107.2
	Post-RE:	5.7 (-21.3%)	2.7 (-58.1%)	3.0 (+312.8%)	1437.3 (+28.3%)	997.6 (-1.2%)	435.1 (+305.9%)
13	Pre-RE:	6.2	4.1	1.8	1252.5	791.1	326.5
	Post-RE:	6.0 (-4.5%)	1.9 (-54.7%)	3.9 (+118.4%)	1234.4 (-1.4%)	633.7 (-19.9%)	507.7 (+55.5%)

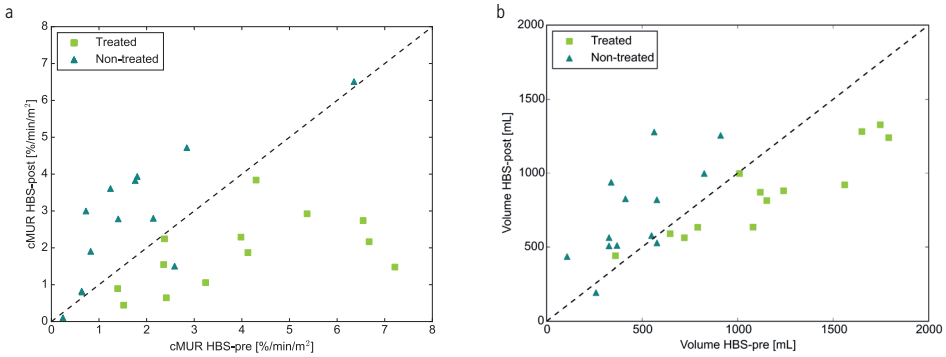

Figure 3: (a) Liver function obtained from the HBS-pre and HBS-post and (b) liver volume pre- and post-treatment for each individual patient. Points above the dashed line indicate function/volume increase, points below the dashed line indicate function/volume decline.

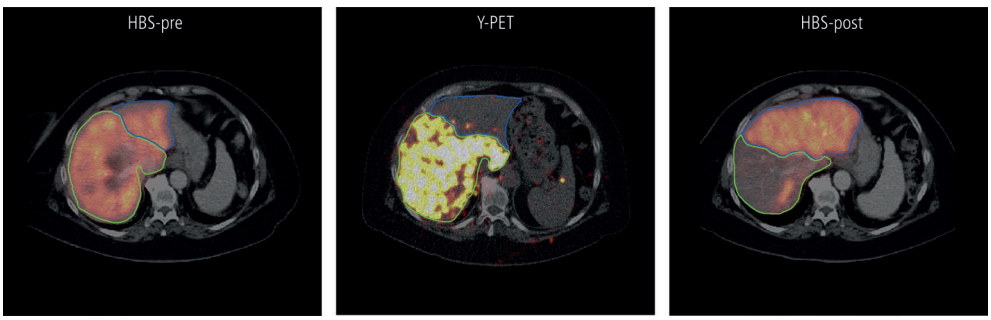

Figure 4: Example of volume decrease in the treated part of the liver (-41%) with compensatory increase in volume of the non-treated part (+178%). The functional liver parenchyma obtained a high absorbed dose of ^{90}Y (105 Gy on functional liver, 145 Gy on the tumour). This particular part of the liver lost most of its function (HBS-pre: 7.2 %/min/m^2; HBS-post: 1.5 %/min/m^2). The non-treated part increased in function (HBS-pre: 1.2 %/min/m^2; HBS-post: 3.6 %/min/m^2).

In most patients (n = 12), treated volume decreased (pre-treatment: 1118.7 ml (360.4 – 1790.8); post-treatment: 870.7 ml (441.0 – 1327.6); p = 0.003), while the non-treated volume increased (pre-treatment: 412.7 ml (107.2 – 910.8); post-treatment: 577.6 ml (193.5 – 1278.4); p = 0.005) (Figures 2b, 3b and 4). Whole liver volume, however, did not change significantly after radioembolisation (pre-treatment: 1683.3 ml (983.5 – 3112.5); post-treatment: 1792.4 ml (1012.4 – 3161.2); p = 0.600). For two patients, both with cirrhotic livers, volume of the non-treated part decreased after radioembolisation. One of these patients also had a decrease in liver function and died of REILD four months after treatment, as described above. The other patient had a slight increase of function in the non-treated part (+29.2%), but died four months after treatment due to hepatic failure (probably REILD, whole liver function post-treatment: 2.4 %/min/m^2) (9).

No correlation was found between the absorbed dose in the treated functional liver tissue and the absolute function change ($cMUR_{post}$ - $CMUR_{pre}$) in the treated functional liver tissue (Spearman ρ = -0.31, p = 0.310), nor was a correlation found between absorbed dose and volume change (Spearman ρ = 0.09, p = 0.768). However, the three patients who received the highest absorbed

dose (average absorbed dose >104.5 Gy) showed a larger function decline (cMUR change <-3.8 %/min/m^2) than the patients receiving a lower absorbed dose (cMUR change >-2.4 %/min/m^2) (p = 0.007). Interestingly, these three patients also showed the largest function increase (cMUR change >2.1 %/min/m^2) in the non-treated part (p = 0.011). No such relationships were observed for absorbed dose versus volume change.

Whole liver volume and whole liver function showed no correlation at baseline (Spearman ρ = -0.07, p = 0.817). Bland-Altman analysis revealed a large bias of 29.0% and wide limits of agreement (-7.68 – 65.60 percentage point (pp)) for relative changes in the treated part (Figure 5a). In the non-treated part, this bias was -6.0% (Figure 5b), but the limits of agreement were still wide (-117.9 – 106.7 pp). In both the treated and non-treated part of the liver, the individual differences were large.

Large individual differences between function and volume changes in the non-treated lobe were found: 10/13 patients had an increase of both function and volume with a median relative difference between percent function and volume increase of 61% (range 2 - 134%), 1/13 patients had a decrease of both with a relative difference of 127%, and 2/13 patients had an increase of one parameter and a decrease of the other. The relative effect in the non-treated lobe was larger for function than for volume in 10/13 patients.

In two patients, the difference between function change and volume change of the non-treated part were not concordant. One patient (patient 5; Table 2) showed a large volume increase in the non-treated part (+127.0%), while function decreased (-41.9%). The other patient (patient 2; Table 2) showed a decrease in volume (-8.6%), but liver function in the non-treated part increased nonetheless (+29.2%).

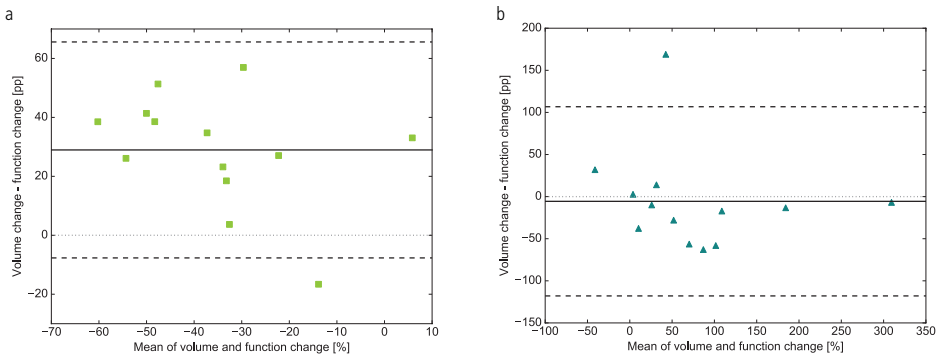

Figure 5: Bland-Altman plot of the relative change in volume versus the relative change in function in (a) the treated part (bias: 29.0%, limits of agreement: -7.68 – 65.60 pp) and (b) the non-treated part (bias: -6.0%, limits of agreement: -117.9 – 106.7 pp). Solid line indicates mean, dashed lines indicate limits of agreement (mean ± 1.96*std).

Discussion

Lobar radioembolisation induces a decrease in function and volume in the treated part and an increase in function and volume in the non-treated part of the liver. The limits of agreement between relative function and volume change were wide, reflecting large individual differences. This may implicate a complementary role for regional function assessment with HBS in the selection and treatment planning of patients undergoing radioembolisation, especially in patients undergoing lobar radioembolisation with the aim to induce contralateral hypertrophy as a bridge to surgery with curative intent (i.e. radiation lobectomy) (2).

The concept of radiation lobectomy has been shown to be a feasible and effective treatment modality as a bridge to surgery in HCC patients, as an alternative to portal vein embolisation (4). With a median interval between ^{90}Y (glass microspheres) radioembolisation and resection of 2.9 months (interquartile range [IQR]: 2-5 months), the median FLR hypertrophy was 23.3% (IQR: 10-48%) after radiation lobectomy. Complete, 50-99%, and <50% pathologic tumour necrosis was identified in 14 (45%), 10 (32%), and 7 (23%) tumours, confirming interval disease control (4). Palard et al. (16) showed a relationship between functional liver absorbed dose and FLR hypertrophy in 73 HCC patients who received lobar radioembolisation using ^{90}Y glass microspheres. Patients who received a functional liver absorbed dose >88 Gy had a 92% chance of an FLR hypertrophy of at least 10% versus 66% for patients who received <88 Gy ($p <$ 0.05). Interestingly, the tumour absorbed dose, tumour size, baseline FLR volume, and Child-Pugh score also influenced FLR hypertrophy, illustrating the multifactorial physiological process of FLR hypertrophy (16).

The physiology of FLR hypertrophy is poorly understood. From the lengthy experience with PVE, however, it is known that embolisation, diverting flow towards the FLR, plays a role. The embolising properties for each radioembolisation product vary considerably, and in the case of ^{90}Y glass microspheres also depends on the interval between calibration and administration (i.e. week 1-2 microspheres). This should be taken into account. The previously mentioned study by Palard et al. (16) was performed with less embolic week 1 microspheres, but it may be expected that dose-effect relationships will be different for the more embolic week 2 ^{90}Y glass microspheres. In our study, a mix of week 1 and week 2 treatments was used for logistic reasons.

In our study, patients receiving the highest average functional liver absorbed dose also showed the largest function decrease in the treated part and the largest function increase in the non-treated part. In contrast, no such pattern was seen in the relationship between absorbed dose and volume change, with large individual differences between function and volume changes. With increasing attention to personalised dosimetry-based treatment planning, further investigations regarding the relation between function change and absorbed dose is required and could have relevant clinical implications.

HBS with SPECT/CT allows for an accurate quantification of regional liver function. This may improve the future work-up of patients who are candidates for radioembolisation, reducing the risk of hepatotoxicity. In a small case-series of three patients, we previously showed that discrepancies between lab values and liver function assessment using HBS may lead to dismal outcomes, that potentially could have been prevented if regional HBS results would have been taken into account (9). The suggested cMUR cut-off value of 2.69 %/min/m^2 for liver surgery (7) may be lower for lobar radioembolisation, since radiation damage is a more gradual process

compared to resection, and liver function may increase up to 12 months after radioembolisation, both in the treated and the non-treated part of the liver (17). Establishing the relationship between functional liver absorbed dose and functional changes is expected to lead to optimisation of treatment planning by taking a pre-specified FLR function into account.

Although the largest series to date, the main limitation of this pilot study is the small cohort size. Due to the retrospective nature, no correlation with outcome measures (i.e. survival or hepatotoxicity) was possible, and a clear dose-effect relationship could not be established. Furthermore, liver function evaluation was only performed at 3 months, while the non-treated volume increases up to 9 months after treatment (2). It would be interesting to assess liver function and volume after a longer period of time following radioembolisation (i.e. follow-up of 9-12 months).

The next step towards the clinical implementation of HBS as a complementary imaging modality in radioembolisation work-up would be a large prospective validation study, in which baseline and follow-up HBS would be compared to outcome measures. In addition, the relation between radiation absorbed dose and function change and the relation between FLR function and toxicity should be investigated to fully understand the potential of using HBS as an additional patient selection criterion, and possibly a parameter for individualised dosimetry-based treatment planning.

Conclusion

Radioembolisation induces regional changes in liver function that are accurately detected by HBS. Limits of agreement between function and volume changes after lobar radioembolisation were wide, showing large individual differences. This implicates that HBS may have a complementary role in the management of patients for radiation lobectomy.

References

1. AJAT Braat, MLJ Smits, MNGJA Braat, AF van den Hoven, JF Prince, HWAM de Jong, et al., ^{90}Y Hepatic Radioembolisation: An Update on Current Practice and Recent Developments, J. Nucl. Med., 2015, 56(7):1079–87.
2. M Vouche, RJ Lewandowski, R Atassi, K Memon, VL Gates, RK Ryu, et al., Radiation lobectomy: Time-dependent analysis of future liver remnant volume in unresectable liver cancer as a bridge to resection, J. Hepatol., 2013, 59(5):1029–36.
3. A Gabr, N Abouchaleh, R Ali, M Vouche, R Atassi, K Memon, et al., Comparative study of post-transplant outcomes in hepatocellular carcinoma patients treated with chemoembolization or radioembolisation, Eur. J. Radiol., 2017, 93(May):100–6.
4. A Gabr, N Abouchaleh, R Ali, T Baker, J Caicedo, N Katariya, et al., Outcomes of Surgical Resection after Radioembolisation for Hepatocellular Carcinoma, J. Vasc. Interv. Radiol., 2018, 29(11):1502–1510.
5. RJ Bennink, S Dinant, D Erdogan, BH Heijnen, IH Straatsburg, AK Van Vliet, et al., Preoperative Assessment of Postoperative Remnant Liver Function Using Hepatobiliary Scintigraphy, J Nucl Med, 2004, 45(6):965–71.
6. S Dinant, W de Graaf, BJ Verwer, RJ Bennink, KP van Lienden, DJ Gouma, et al., Risk Assessment of Posthepatectomy Liver Failure Using Hepatobiliary Scintigraphy and CT Volumetry, J. Nucl. Med., 2007, 48(5):685–92.
7. W de Graaf, KP van Lienden, S Dinant, JJTH Roelofs, ORC Busch, DJ Gouma, et al., Assessment of future remnant liver function using hepatobiliary scintigraphy in patients undergoing major liver resection, J. Gastrointest. Surg., 2010, 14(2):369–78.
8. T Chapelle, B Op De Beeck, I Huyghe, S Francque, A Driessen, G Roeyen, et al., Future remnant liver function estimated by combining liver volumetry on magnetic resonance imaging with total liver function on ^{99m}Tc-mebrofenin hepatobiliary scintigraphy: Can this tool predict post-hepatectomy liver failure?, Hpb, 2016, 18(6):494–503.
9. MNGJA Braat, HW de Jong, BA Seinstra, MV Scholten, MAAJ van den Bosch, and MGEH Lam, Hepatobiliary scintigraphy may improve radioembolisation treatment planning in HCC patients, EJNMMI Res., 2017, 7(1):2.
10. RJ Bennink, KP Cieslak, OM van Delden, KP van Lienden, H-J Klümpen, PL Jansen, et al., Monitoring of Total and Regional Liver Function after SIRT, Front. Oncol., 2014, 4:1–5.
11. SA Gulec, G Mesoloras, and M Stabin, Dosimetric Techniques in ^{90}Y-Microsphere Therapy of Liver Cancer : The MIRD Equations for Dose Calculations, 2016, 47(7):1209–12.
12. F Giammarile, L Bodei, C Chiesa, G Flux, F Forrer, F Kraeber-Bodere, et al., EANM procedure guideline for the treatment of liver cancer and liver metastases with intra-arterial radioactive compounds, Eur. J. Nucl. Med. Mol. Imaging, 2011, 38(7):1393–406.
13. W de Graaf, KP van Lienden, TM van Gulik, and RJ Bennink, ^{99m}Tc-Mebrofenin Hepatobiliary Scintigraphy with SPECT for the Assessment of Hepatic Function and Liver Functional Volume Before Partial Hepatectomy, J. Nucl. Med., 2010, 51(2):229–36.
14. M Ekman, M Fjälling, S Friman, S Carlson, and R Volkmann, Liver uptake function measured by iodida clearance rate in liver transplant patients and healthy volunteers, Nucl. Med. Commun.1996, 17(3):235–42.
15. PJ Johnson, S Berhane, C Kagebayashi, S Satomura, M Teng, HL Reeves, et al., Assessment

of liver function in patients with hepatocellular carcinoma: A new evidence-based approach - The albi grade, J. Clin. Oncol., 2015, 33(6):550–8.

16. X Palard, J Edeline, Y Rolland, S Le Sourd, M Pracht, S Laffont, et al., Dosimetric parameters predicting contralateral liver hypertrophy after unilobar radioembolisation of hepatocellular carcinoma, Eur. J. Nucl. Med. Mol. Imaging, 2018, 45(3):392–401.
17. JM Theysohn, J Ertle, S Müller, JF Schlaak, F Nensa, S Sipilae, et al., Hepatic volume changes after lobar selective internal radiation therapy (SIRT) of hepatocellular carcinoma, Clin. Radiol., 2014, 69(2):172–8.

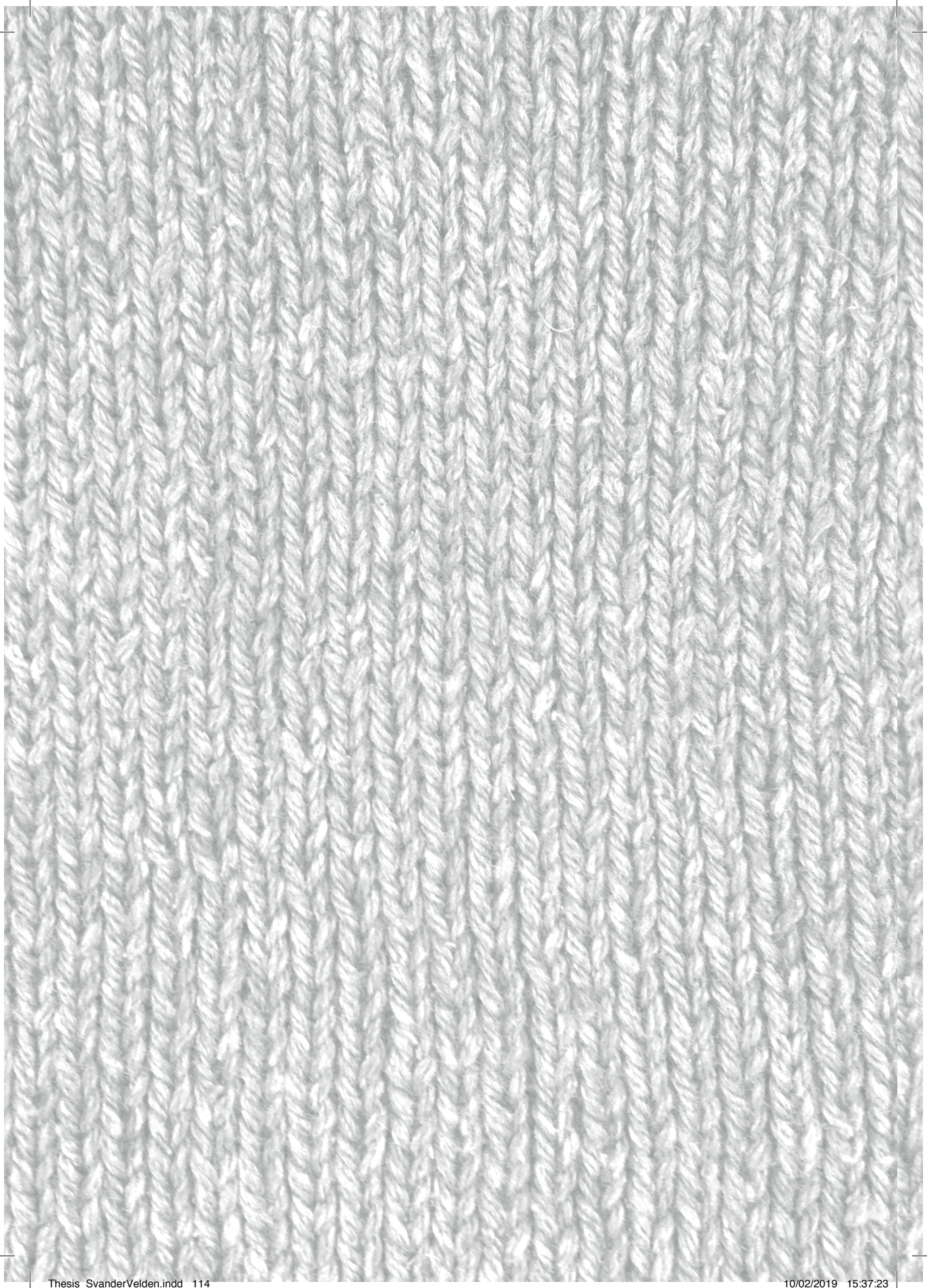

7

Summary and discussion

Summary

The aim of this thesis was to investigate the development and application of a device which can acquire both fluoroscopic and nuclear images in the intervention room for guidance of liver radioembolisation procedures. Radioembolisation with yttrium-90 (^{90}Y) is a liver cancer treatment, in which radioactive microspheres are injected into the liver. The microspheres will lodge in the tumour, hence giving very local radiation damage. Preceding the treatment, a safety procedure using technetium-99m macroaggregated albumin (^{99m}Tc-MAA) is performed to ensure a safe distribution of the microspheres. Availability of nuclear images in the intervention room would be beneficial, allowing both the pre-treatment procedure and the treatment to be performed in a single session. The first part of this thesis described the development of the hardware required for a device that can simultaneously acquire fluoroscopic and nuclear images in the intervention room. The second part of this thesis focussed on the clinical impact of such a device and other nuclear imaging techniques to optimise radioembolisation procedures.

Two designs for a hybrid fluoroscopic and nuclear imaging device were made. In the first design, an x-ray c-arm was combined with four gamma cameras placed adjacent to the x-ray tube. The four gamma camera views were used to reconstruct an intermediate three-dimensional image, which was subsequently converted to a virtual nuclear projection image that overlaps with the x-ray image. This design was proven to be feasible (1), but the intermediate reconstruction step and the added weight to the already heavy x-ray tube were not ideal. Therefore, a dual layer detector, consisting of an x-ray flat panel placed in front of a gamma camera with cone beam collimator focussed at the x-ray focal spot, was designed. This design relies on the x-ray detector absorbing the majority of the x-rays, while being more transparent to the higher energy gamma photons. No intermediate reconstruction step is needed and fluoroscopic and nuclear images are intrinsically registered to each other.

This thesis started with a study concerning the first design of a hybrid imaging device. In **Chapter 2**, the impact of gamma camera collimator choice (parallel hole versus pinhole) on the quality of the virtual nuclear image was investigated by means of a simulation study. It turned out that for small hot spots, contrast was comparable for all simulated collimators. Noise levels were, however, 3 to 8 times higher in pinhole geometries than in parallel hole geometries. This resulted in higher contrast-to-noise ratios for parallel hole geometries. Smaller spheres could thus be detected with parallel hole collimators than with pinhole collimators (17 mm versus 28 mm). In addition, pinhole geometries showed larger image deformations than parallel hole geometries. Spatial resolution varied between 1.25 cm and 4 cm for the 3 mm pinhole and the low-energy-all-purpose collimator, respectively. The simulation method was successfully validated by experiments with the physical prototype. In conclusion, parallel hole collimators showed lower noise and better detectability than pinhole collimators.

In **Chapter 3**, the dual layer detector, as an alternative for the design presented in Chapter 2, was developed and evaluated. A prototype was built and dynamic phantom images were acquired. In addition, spatial resolution and system sensitivity were measured with the prototype. Monte Carlo simulations for an improved system with varying flat panel compositions were performed to assess potential spatial resolution and system sensitivity. Measurements of the physical phantoms showed the ability of the dual layer detector. Experiments with the prototype showed that resolution of the nuclear images was unaffected by the addition of the flat panel.

However, addition of the flat panel lowered system sensitivity by 45% to 60%, owing to the non-optimised transmission of the flat panel. Simulations showed that an attenuation of 27% to 35% of the gamma rays in the flat panel could be achieved by improving the system. The proposed dual layer detector was thus found capable of acquiring real-time intrinsically registered hybrid images. This could aid interventional procedures involving radionuclides, such as radioembolisation.

The efficiency of radioembolisation procedures could be greatly enhanced if results of the ^{99m}Tc-MAA pre-treatment procedure would already be available in the intervention room, enabling single-session procedures thanks to direct intrahepatic dose feedback, assessment of extrahepatic depositions and lung shunt estimation. In addition, measuring regional liver function might have a valuable role in the management of patients treated with radioembolisation. The second part of this thesis concerned the improvement of radioembolisation procedures by interventional hybrid imaging and other nuclear imaging techniques.

Depending on the lung shunt fraction (LSF), treatment may be altered or abandoned. The accuracy of estimating LSF in the intervention room with the device from Chapter 2 was evaluated in **Chapter 4**. In addition, it was compared against current clinical methods. To this end, a male and female XCAT phantom, both with two respiratory profiles, were used to simulate various LSFs resulting from a scout dose of 150 MBq ^{99m}Tc-MAA. In the clinically relevant range of 10% to 20% LSF, hybrid imaging overestimated LSF with approximately 2 to 3 percentage points (pp). After organ overlap correction, LSF was estimated with a more constant error (~1 pp). Errors in planar scintigraphy and mobile gamma camera imaging were more dependent on LSF, body shape and breathing profile (range -3 – +4 pp). From this study, we concluded that LSF can be estimated with a constant minor error with our hybrid imaging device within a few seconds in an interventional setting.

To evaluate the intrahepatic distribution and the presence of any extrahepatic depositions, a SPECT scan is needed. A clinical SPECT scan, however, takes approximately 30 minutes, which is too long for interventional purposes. **Chapter 5** investigated whether a fast SPECT protocol is feasible and if non-uniform projection-time acquisition protocols improve accuracy. SPECT liver images of the 150-MBq ^{99m}Tc-MAA safety procedure were simulated for different phantoms, total acquisition times and acquisition protocols. Simulations showed no substantial change in image quality and dosimetry by usage of a non-uniform time acquisition protocol. Upon shortening acquisition times, CNR dropped, but ARC, T/N ratio and LSF estimates were stable across all simulated acquisition times. Results of the physical phantom were in correspondence with the simulations. In conclusion, both uniform and non-uniform projection-time acquisition liver SPECT protocols yield accurate dosimetric metrics for radioembolisation treatment planning in the interventional suite within 10 minutes, without compromising image quality. Consequently, fast interventional SPECT of the liver in the intervention room is feasible.

Radioembolisation is increasingly used as a bridge to resection (i.e. radiation lobectomy). It combines ipsilateral tumour control with the induction of contralateral hypertrophy to facilitate lobar resection. In **Chapter 6**, the potential complementary value of hepatobiliary scintigraphy (HBS) before and after radioembolisation in the assessment of the future remnant liver was investigated. Thirteen patients who underwent HBS before and after radioembolisation with ^{90}Y glass microspheres were included. Liver function and volume of the whole liver, as well as the treated and non-treated part separately, were determined on HBS. Absorbed dose was determined on ^{90}Y PET/CT. Radioembolisation induced liver function and volume decline in the

treated part and liver function and volume increase in the non-treated part. Limits of agreement between function and volume changes were wide, showing large individual differences. This implicates that HBS may have a complementary role in the management of patients treated with radiation lobectomy.

General discussion

Part I

In the first part of this thesis, two systems capable of acquiring simultaneous real-time nuclear and fluoroscopic images were presented. The first design consisted of a c-arm with multiple gamma cameras at the side of the x-ray tube. This design was proven to be feasible (1) and steps were taken to improve the design by means of a different collimator choice. However, there were some major drawbacks related to this design, primarily the need for an intermediate reconstruction to create a hybrid image. The dual layer design tackled this problem by positioning the gamma camera directly behind the x-ray flat panel detector. This resulted in intrinsically registered hybrid images, without the need for an intermediate reconstruction step. This design was also found to be feasible (Chapter 3) and is currently the design of choice for further investigations and development.

Limitations of the hybrid imaging device

Substantial spill-over of x-rays into the nuclear images was discovered in the first prototype of the hybrid imaging system (1). This problem still exists in our new dual layer design, since the x-ray flat panel does not absorb all the x-rays. A small part will transmit through the x-ray flat panel and will be detected by the gamma camera. It was shown that at low doses (<0.02 nGy per x-ray pulse on the gamma camera), gamma photons were measured at elevated energies due to pile-up effects during the x-ray pulse, but no effects were seen after the x-ray pulse (2). The elevated energies during the x-ray pulse can be avoided by using interleaved measurements. For example, in case of 10 ms x-ray pulses and a 4 Hz frame rate, only 4% of the gamma counts would theoretically be lost, which would be acceptable. At higher doses (0.28 nGy per x-ray pulse on the gamma camera), however, the gamma camera was blinded during the x-ray pulse and non-linear effects (afterglow and PMT limitations) were observed directly after the x-ray pulse (2). Possible solutions for this include modifying the PMT circuitry (2), gating the PMTs (i.e. switch the PMTs off during x-ray pulses), using a high-pass filter to correct for elevated energies, the use of a different detection crystal with less afterglow (e.g. $CeBr_3$ (3)) or the use of solid-state detectors capable of handling high count rates (e.g. CdZnTe (3)). Other options to reduce the effect of x-ray spill-over are based on minimising the amount of x-rays reaching the gamma camera, such as placing the cone beam collimator slightly off-focus or an extra filter between the x-ray flat panel and the gamma camera. If, for example, this filter is made of 0.5 mm Tin (Sn), an 80 kVp x-ray spectrum will be attenuated by 93%, while the 140 keV gamma rays will only be attenuated by 23% (4).

Ideally, a solution should be chosen that minimises the detrimental effects of the x-ray pulses, without limiting the sensitivity for gamma rays. This would exclude the option of an extra filter. The option of an off-focus collimator is also not ideal, since this would result in a (small) registration mismatch between the nuclear and fluoroscopic image. The usage of $CeBr_3$

or CdZnTe seems promising, but both are expensive and not yet available in large crystal areas. Modifying the PMT circuitry, gating the PMTs and using a high-pass filter in combination with a NaI(Tl) scintillation crystal would be therefore the most viable option. In the future, however, prices of $CeBr_3$ or CdZnTe may drop, making them promising candidates for our purpose.

Future perspectives

Although the dual layer detector prototype showed the technical feasibility of acquiring real-time hybrid images, this prototype is not suitable for clinical testing. Therefore, current efforts are focussing on the development of a mobile device, in which the gamma camera is attached to an x-ray c-arm. This would allow usage of the prototype in an interventional setting to proof the added value of hybrid images in the clinic. In addition, such a mobile device will have the possibility to rotate around the patient, acquiring tomographic views. This would allow acquiring a SPECT/CT scan in the intervention room.

The current x-ray flat panel has been modified to improve transmission of gamma rays. However, transmission through the flat panel is still inhomogeneous and not optimised. Future research should be directed towards redesigning the electronics of the flat panel in order to position them at the sides. This would improve the homogeneity of the gamma image and would increase the transmission. In addition, the flat panel housing could be redesigned to be as light and transparent as possible.

The research in this thesis focussed on nuclear image quality. Fluoroscopic image quality, however, should ideally not be hampered by the addition of gamma imaging capabilities. In the current prototype, no anti-scatter grid was used to maximise the gamma photon sensitivity. Clinically, however, an anti-scatter grid is routinely used to improve fluoroscopic image quality. Additional research regarding x-ray scatter rejection is therefore needed. Possible methods for rejection of scatter include anti-scatter grids (either conventional or aligned to the cone beam collimator) (5) or scatter correction algorithms (5,6).

Alternative devices for interventional nuclear imaging

Interventional nuclear imaging can also be achieved using hand-held gamma cameras or probes (7,8). Three-dimensional images can be obtained using freehand SPECT, in which the acquired projections are reconstructed into a three-dimensional volume (9–11). For the purpose of sentinel node procedures (12,13), the SPECT images are fused with ultrasound images for anatomical reference (14,15). In freehand SPECT, however, the quality of the images depends heavily on the experience of the operator acquiring the projections. A controlled trajectory, and hence improved image quality, can be obtained by mounting the gamma probe on a robotic arm (16,17). Such interventional SPECT images can subsequently be fused with intraoperatively acquired CT images for anatomical reference (18). Alternatively, interventional nuclear images can be registered to pre-operative images (19). In all mentioned alternatives, however, nuclear images and anatomical images are not simultaneously acquired. Since registration of images of two different modalities remains challenging due to motion and pre-operative images may not represent the actual situation at the time of the intervention, the quality of these hybrid images may not be optimal.

Part II

Availability of hybrid images in the intervention room may allow evaluation of the ^{99m}Tc-MAA procedure during the intervention. This would be of great advantage, since this would open up the possibility of single-session procedures. Currently, radioembolisation procedures are split into two phases (pre-treatment ^{99m}Tc-MAA and therapy ^{90}Y microsphere administration) separated by one to two weeks, since microspheres are ordered after the pre-treatment procedure. It has been shown that single-session procedures are feasible (20,21), shortening total procedure times. In these studies, however, patients were still transported to and from the nuclear medicine department. When the ^{99m}Tc-MAA distribution could be evaluated in the intervention room, total procedure times could be further reduced. In addition, the catheter could be kept in place, improving the prognostic power of the scout dose (22).

Prognostic power of the pre-treatment procedure

This thesis focussed on using interventional hybrid images for the evaluation of the pre-treatment procedure with ^{99m}Tc-MAA. This scout dose is supposed to mimic the distribution of the ^{90}Y microspheres and is used in treatment planning. The prognostic power of ^{99m}Tc-MAA is, however, debated. In a study by Elschot et al. (23), it was shown that LSF was overestimated by ^{99m}Tc-MAA compared with estimations from a scout dose of ^{166}Ho microspheres. Overestimation with ^{99m}Tc-MAA was reduced by using SPECT instead of planar scintigraphy, but there remained a difference between LSF obtained from a scout dose of ^{99m}Tc-MAA and a scout dose of ^{166}Ho microspheres. This difference was suggested to arise from the difference in size between ^{99m}Tc-MAA particles and ^{166}Ho microspheres. A relatively large fraction of ^{99m}Tc-MAA particles is smaller than 20 μm and thus prone to shunting to the lungs, while ^{166}Ho particles are larger and more stable. ^{90}Y particles are comparable to ^{166}Ho particles with respect to stability and size, hence the found overestimation might also exist for treatment with ^{90}Y microspheres. Recent research, however, has shown that it is feasible to estimate LSF with a scout dose of ^{90}Y (24). In principle, such a scout dose can also be imaged with our dual layer detector. Future research should investigate whether extrahepatic depositions and treatment planning can also be assessed with a ^{90}Y scout dose and if this can be done in a short time, allowing imaging in the intervention room.

Clinical evaluation

The presented research regarding the improvement of radioembolisation procedures with our hybrid imaging device is based on simulation results. A first step towards clinical implementation would be to verify with a clinical trial that the hybrid images are of sufficient quality to assess the injection position, lung shunt fraction, extrahepatic depositions and the intrahepatic distribution. About ten to twenty radioembolisation patients should be included and all will be treated conform the current clinical protocol. As an addition, however, hybrid images will be acquired with the dual layer detector during the pre-treatment procedure. These images can be retrospectively compared with the images obtained at the nuclear medicine department to verify the quality. When the hybrid images are proven to be of sufficient image quality, a second clinical trial can be started to investigate the potential of single-session procedures.

Future perspectives

Besides radioembolisation, other procedures involving radionuclides, such as sentinel node procedures (25), biopsies (26), tumour resections (27) and radiofrequency ablations (19), could potentially benefit from the availability of nuclear images in the intervention room. It should be investigated whether these procedures could benefit from the hybrid images obtained with the current prototype. However, small adaptations to the prototype might be needed to optimise resolution and sensitivity needed in these procedures.

Much research is currently ongoing regarding directed radionuclide therapy, where the radionuclide is bound to a specific peptide or antigen. Most of these radionuclides are intravenously injected, but these therapies might benefit from intra-arterial injection to increase the tumour dose (28,29). It is expected that the amount of therapies with more directed injection positions will increase in the future. Hybrid imaging might be of added value for such therapies as well, since the radionuclide distribution can be imaged directly after administration.

Conclusions

- Parallel hole collimators show lower noise and better detectability than pinhole collimators when used in our first design of a hybrid imaging device.
- A dual layer detector, consisting of an x-ray flat panel detector placed in front of a gamma camera with cone beam collimator focussed at the x-ray focal spot, is capable of acquiring real-time intrinsically registered hybrid images.
- Lung shunt fraction can be estimated with a constant minor error with a hybrid imaging device within a few seconds in an interventional setting.
- Both uniform and non-uniform projection-time acquisition liver SPECT protocols yield accurate dosimetric metrics for radioembolisation treatment planning in the interventional suite within 10 minutes, without compromising image quality.
- Radioembolisation induces regional changes in liver function, but function and volume changes showed large individual differences, implicating that HBS may have a complementary role in the management of patients for radiation lobectomy.

References

1. C Beijst, M Elschot, MA Viergever, and HWAM de Jong, Toward Simultaneous Real-Time Fluoroscopic and Nuclear Imaging in the Intervention Room, Radiology, 2016, 278(1):232–8.
2. WJC Koppert, S van der Velden, JHL Steenbergen, and HWAM de Jong, Impact of intense x-ray pulses on a NaI(Tl)-based gamma camera, Phys. Med. Biol., 2018, 63(6):065006.
3. WJC Koppert, S van der Velden, JHL Steenbergen, and HWAM de Jong, A comparative study on NaI(Tl), $CeBr_3$ and CdZnTe as gamma sensor for real-time (near-)simultaneous nuclear and x-ray imaging, Submitted for publication.
4. Xcom, and NIST, Photon cross sections database [Internet], Retrieved August 2018.
5. R Gupta, M Grasruck, C Suess, SH Bartling, B Schmidt, K Stierstorfer, et al., Ultra-high resolution flat-panel volume CT: Fundamental principles, design architecture, and system characterization, Eur. Radiol., 2006, 16(6):1191–205.
6. R Ning, XY Tang, and D Conover, X-ray scatter correction algorithm for cone beam CT imaging, Med. Phys., 2004, 31(5):1195–202.
7. S Heller, and P Zanzonico, Nuclear probes and intraoperative gamma cameras, Semin. Nucl. Med., 2011, 41(3):166–81.
8. M Tsuchimochi, and K Hayama, Intraoperative gamma cameras for radioguided surgery: Technical characteristics, performance parameters, and clinical applications, Phys. Medica, 2013, 29(2):126–38.
9. C Bluemel, A Schnelzer, A Okur, A Ehlerding, S Paepke, K Scheidhauer, et al., Freehand SPECT for image-guided sentinel lymph node biopsy in breast cancer, Eur. J. Nucl. Med. Mol. Imaging, 2013, 40(11):1656–61.
10. DA Heuveling, S Van Weert, KH Karagozoglu, and R De Bree, Evaluation of the use of freehand SPECT for sentinel node biopsy in early stage oral carcinoma, Oral Oncol., 2015, 51(3):287–90.
11. AL Mihaljevic, A Rieger, B Belloni, R Hein, A Okur, K Scheidhauer, et al., Transferring innovative freehand SPECT to the operating room: First experiences with sentinel lymph node biopsy in malignant melanoma, Eur. J. Surg. Oncol., 2014, 40(1):42–8.
12. C Bluemel, G Safak, A Cramer, A Wöckel, A Gesierich, E Hartmann, et al., Fusion of freehand SPECT and ultrasound: First experience in preoperative localization of sentinel lymph nodes, Eur. J. Nucl. Med. Mol. Imaging, 2016, 43(13):2304–12.
13. R de Bree, B Pouw, DA Heuveling, and JA Castelijns, Fusion of Freehand SPECT and Ultrasound to Perform Ultrasound-Guided Fine-Needle Aspiration Cytology of Sentinel Nodes in Head and Neck Cancer, Am. J. Neuroradiol., 2015, 36(11):2153–8.
14. M Freesmeyer, T Opfermann, and T Winkens, Hybrid Integration of Real-time US and Freehand SPECT: Proof of Concept in Patients with Thyroid Diseases, Radiology, 2014, 271(3):856–61.
15. M Freesmeyer, T Winkens, T Opfermann, P Elsner, I Runnebaum, and A Darr, Real-time ultrasound and freehand-SPECT, Nuklearmedizin, 2014, 53(06):259–64.
16. J Gardiazabal, P Matthies, J Vogel, B Frisch, N Navab, S Ziegler, et al., Flexible mini gamma camera reconstructions of extended sources using step and shoot and list mode, Med. Phys., 2016, 43(12):6418–28.

17. J Vogel, T Lasser, J Gardiazabal, and N Navab, Trajectory optimization for intra-operative nuclear tomographic imaging, Med. Image Anal., 2013, 17(7):723–31.
18. J Gardiazabal, M Esposito, P Matthies, A Okur, J Vogel, S Kraft, et al., Towards Personalized Interventional SPECT-CT Imaging, In: Lecture Notes in Computer Science (including subseries Lecture Notes in Artificial Intelligence and Lecture Notes in Bioinformatics). 2014, 504–11.
19. BJ Wood, JK Locklin, A Viswanathan, J Kruecker, D Haemmerich, J Cebral, et al., Technologies for Guidance of Radiofrequency Ablation in the Multimodality Interventional Suite of the Future, J. Vasc. Interv. Radiol., 2007, 18(1):9–24.
20. A Gabr, JR Kallini, VL Gates, R Hickey, L Kulik, K Desai, et al., Same-day ^{90}Y radioembolization: implementing a new treatment paradigm, Eur. J. Nucl. Med. Mol. Imaging, 2016, 43(13):2353–9.
21. VL Gates, KG Marshall, K Salzig, M Williams, RJ Lewandowski, and R Salem, Outpatient Single-Session Yttrium-90 Glass Microsphere Radioembolization, J. Vasc. Interv. Radiol., 2014, 25(2):266–70.
22. E Garin, J Edeline, and Y Rolland, High Impact of Preferential Flow on ^{99m}Tc-MAA and ^{90}Y-Loaded Microsphere Uptake Correlation, J. Nucl. Med., 2016, 57(11):1829–30.
23. M Elschot, JFW Nijsen, MGEH Lam, MLJ Smits, JF Prince, MA Viergever, et al., ^{99m}Tc-MAA overestimates the absorbed dose to the lungs in radioembolization: a quantitative evaluation in patients treated with ^{166}Ho-microspheres, Eur. J. Nucl. Med. Mol. Imaging, 2014, 41(10):1965–75.
24. B Kunnen, S van der Velden, R Bastiaannet, MGEH Lam, MA Viergever, and HWAM de Jong, Radioembolization lung shunt estimation based on a ^{90}Y pre-treatment procedure: a phantom study, Med. Phys., 2018, 45(10):4744–53.
25. K Kobayashi, P Bhargava, S Raja, F Nasseri, HA Al-Balas, DD Smith, et al., Image-guided biopsy: what the interventional radiologist needs to know about PET/CT, Radiographics, 2012, 32(5):1483–501.
26. S Tatli, VH Gerbaudo, M Mamede, K Tuncali, PB Shyn, and SG Silverman, Abdominal masses sampled at PET/CT-guided percutaneous biopsy: initial experience with registration of prior PET/CT images., Radiology, 2010, 256(1):305–11.
27. S Vidal-Sicart, ME Rioja, P Paredes, MR Keshtgar, and RA Valdés Olmos, Contribution of perioperative imaging to radioguided surgery, Q. J. Nucl. Med. Mol. imaging, 2014, 58(2):140–60.
28. GS Limouris, V Poulantzas, N Trompoukis, I Karfis, S Chondrogiannis, N Triantafyllou, et al., Comparison of ^{111}In-[DTPA^{0}]Octreotide Versus Non Carrier Added ^{177}Lu- [DOTA^{0},Tyr3]-Octreotate Efficacy in Patients With GEP-NET Treated Intra-arterially for Liver Metastases, Clin. Nucl. Med., 2016, 41(3):194–200.
29. GS Limouris, I Karfis, A Chatzioannou, MI Paphiti, M Lyra, K Gennatas, et al., Super-selective hepatic arterial infusions as established technique ("ARETAIEION" Protocol) of [^{177}Lu]DOTA-TATE in inoperable neuroendocrine liver metastases of gastro-entero-pancreatic (GEP) tumors., Q. J. Nucl. Med. Mol. Imaging, 2012, 56(6):551–8.

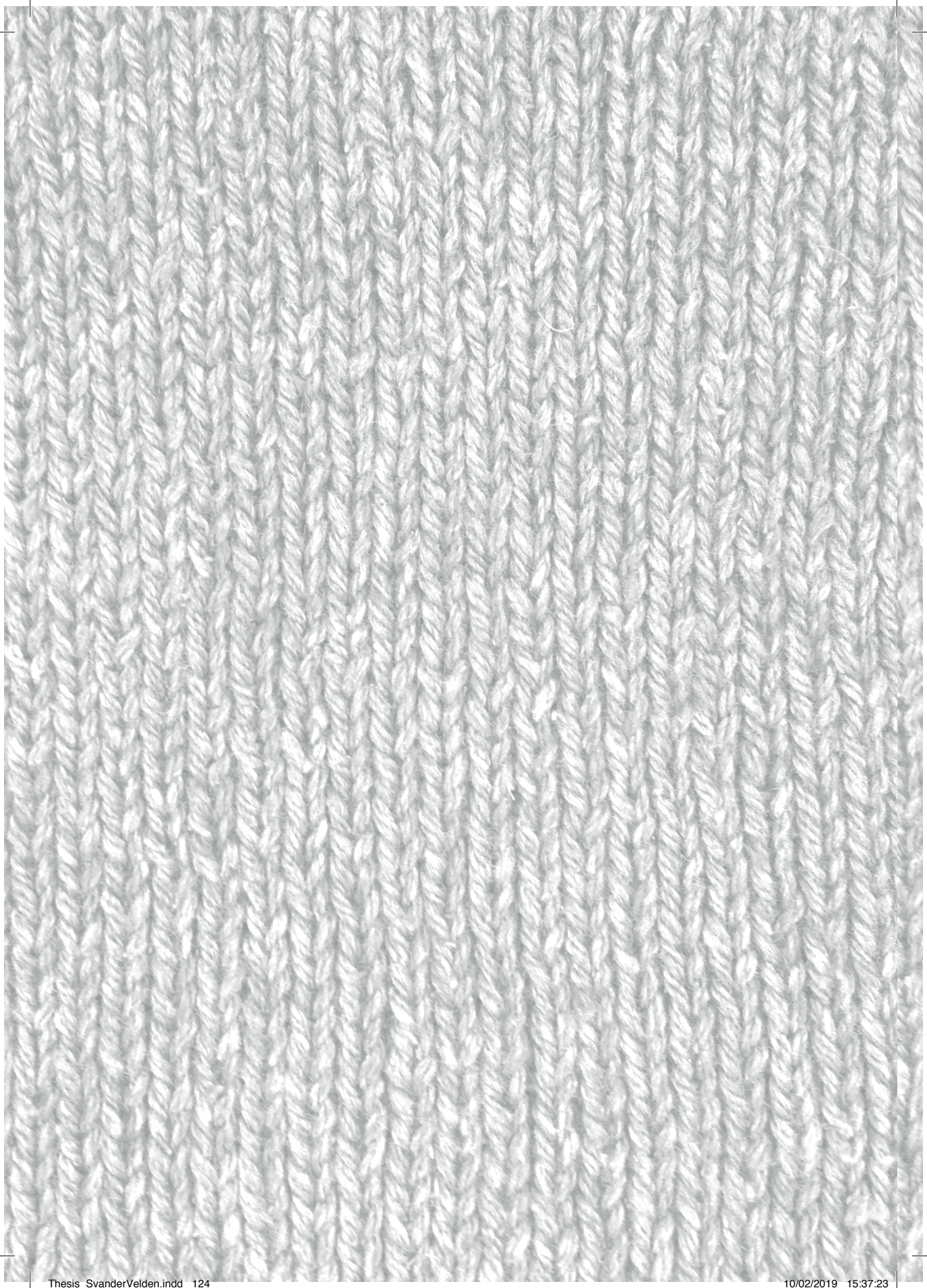

A

Addenda

Nederlandse samenvatting

In dit proefschrift werd de ontwikkeling en toepassing van een nieuwe hybride beeldvormende modaliteit onderzocht. Deze modaliteit kan zowel fluoroscopie- (röntgen)beelden als nucleaire beelden in de interventiekamer opnemen ter geleiding van radio-embolisatieprocedures. Radio-embolisatie met yttrium-90 (^{90}Y) is een behandeling voor leverkanker, waarbij kleine radioactieve bolletjes in de lever worden geïnjecteerd. Deze bolletjes lopen vast in de tumor en zorgen daar zeer lokaal voor schade aan het weefsel. Voordat de bolletjes worden toegediend, vindt er een veiligheidsprocedure met macroaggregaten van albumine gelabeld met technetium-99m (^{99m}Tc-MAA) plaats, waarmee de verwachte verdeling van de therapeutische bolletjes wordt gecontroleerd. Op dit moment is het niet mogelijk om nucleaire beelden in de interventiekamer te maken, waardoor de verdeling van ^{99m}Tc-MAA pas bekend is als er een scan van de patiënt is gemaakt op de afdeling nucleaire geneeskunde. Het zou voordelig zijn om nucleaire beelden beschikbaar te hebben tijdens de interventie, zodat de veiligheidsprocedure en de toediening van de bolletjes in één sessie kunnen plaatsvinden. Het eerste deel van dit proefschrift beschrijft de ontwikkeling van de benodigde hardware om gelijktijdig fluoroscopie- en nucleaire beelden op te nemen in de interventiekamer. Het tweede deel van dit proefschrift focust op de klinische implicaties van zo'n modaliteit en andere nucleaire beeldvorming ter verbetering van radio-embolisatieprocedures.

Er zijn twee verschillende ontwerpen voor een hybride beeldvormende modaliteit gemaakt. In het eerste ontwerp werd een röntgen c-arm gecombineerd met vier gamma camera's rondom de röntgenbuis. De vier gamma-camerabeelden werden gereconstrueerd in een tussentijdse driedimensionale reconstructie, die vervolgens werd omgezet in een nucleair projectiebeeld dat overlapt met het röntgenbeeld. Dit ontwerp was haalbaar, maar de tussentijdse reconstructie en het extra gewicht aan de al zware röntgenbuis waren niet ideaal. Daarom werd een "dual layer" detector ontworpen. Deze detector bestaat uit een platte röntgendetector met daarachter een gamma camera met een gefocusseerde collimator (focus op het brandpunt van de röntgenbuis). Het idee achter dit ontwerp is dat de röntgendetector het merendeel van de röntgenstraling absorbeert, terwijl de hoogenergetische gammafotonen relatief ongehinderd door de röntgendetector heen kunnen. Een tussentijdse reconstructie is niet nodig en de nucleaire beelden zijn intrinsiek geregistreerd met de fluoroscopiebeelden.

In **Hoofdstuk 2** werd het eerste ontwerp voor een hybride beeldvormende modaliteit verder onderzocht. Door middel van een simulatiestudie werd bekeken wat de invloed is van verschillende collimatoren (parallel hole versus pinhole) op de nucleaire beeldkwaliteit. De resultaten lieten zien dat een vergelijkbaar contrast werd verkregen met de verschillende collimatoren. Het ruisniveau was echter 3 tot 8 keer hoger wanneer pinholes werden gebruikt. Dit resulteerde in hogere contrast-ruisverhoudingen voor parellel hole geometrieën. Kleinere bollen konden worden gedetecteerd met parallel hole collimatoren dan met pinhole collimatoren (17 mm versus 28 mm). Bovendien werd het beeld meer vervormd wanneer pinhole collimatoren werden gebruikt dan wanneer parallel hole collimatoren werden gebruikt. De spatiële resolutie varieerde tussen de 1.25 cm met een 3 mm pinhole en 4 cm met de low-energy-all-purpose collimator. De simulatiemethode werd met succes gevalideerd door de experimenten met het fysieke prototype. Concluderend werd een beeld met minder ruis en betere detecteerbaarheid verkregen met parallel hole collimatoren dan met pinhole collimatoren.

In **Hoofdstuk 3** werd een dual layer detector, als alternatief voor het ontwerp uit Hoofdstuk 2, ontworpen en geëvalueerd. Er werd een prototype gebouwd waarmee beelden van dynamische fantomen werden opgenomen. Daarnaast werden de spatiële resolutie en de systeemsensitiviteit gemeten met het prototype. Monte Carlo simulaties van een verbeterd systeem met verschillende röntgendetectorcomposities werden gedaan om potentiële spatiële resolutie en systeemsensitiviteit te onderzoeken. Experimenten met fysieke fantomen lieten de mogelijkheden van het systeem zien. Experimenten met het prototype lieten daarnaast zien dat de spatiële resolutie niet werd aangetast door de toevoeging van de röntgendetector. Dit zorgde echter wel voor een verlaging in sensitiviteit van 45% tot 60%. Simulaties toonden dat een verzwakking van 27% tot 35% haalbaar is met een verbeterd systeem. Het voorgestelde ontwerp van een dual layer detector bleek dus in staat om simultaan intrinsiek geregistreerde hybride beelden op te nemen. Dit zou nuttig kunnen zijn voor interventionele procedures met radionucliden, zoals radio-embolisatie.

De efficiëntie van radio-embolisatieprocedures zou verhoogd kunnen worden wanneer de resultaten van de ^{99m}Tc-MAA veiligheidsprocedure al bekend zouden zijn in de interventiekamer. Dit zou het mogelijk maken om gehele behandeling in één sessie te verrichten, doordat de arts direct de verdeling van bolletjes in de lever kan zien, er gekeken kan worden of er activiteit buiten de lever terecht komt en of er activiteit naar de longen gaat. Daarnaast zou het meten van regionale leverfunctie met een nucleaire scan kunnen leiden tot een beter management van patiënten die worden behandeld met radio-embolisatie. Het tweede deel van dit proefschrift ging over de verbetering van radio-embolisatie door hybride interventionele beeldvorming en andere nucleaire beeldvorming.

De behandeling kan worden aangepast of afgebroken, afhankelijk van de hoeveelheid activiteit die naar de longen gaat (lung shunt fraction (LSF)). De nauwkeurigheid van het schatten van de LSF in de interventiekamer met de modaliteit uit Hoofdstuk 2 werd geëvalueerd in **Hoofdstuk 4**. Daarnaast werd een vergelijking met de huidige klinische standaard gemaakt. Verschillende LSFs, resulterend van de veiligheidsprocedure met 150 MBq ^{99m}Tc-MAA, werden gesimuleerd met behulp van een mannelijk en vrouwelijk digitaal XCAT fantoom, beide met twee ademhalingsprofielen. Hybride beeldvorming overschatte LSF met ongeveer 2 tot 3 procentpunt (pp) in het klinische relevante gebied van 10-20% LSF. LSF werd met een constantere fout (~1 pp) geschat na correctie voor overlappende organen. De fout was meer afhankelijk van LSF, geslacht en ademhalingsprofiel (-3 pp tot +4 pp) wanneer de LSF werd geschat van plenaire scintigrafie beelden of van mobiele gamma-camerabeelden. Uit deze studie hebben we geconcludeerd dat LSF binnen een paar seconden met een kleine, constante fout kan worden geschat met onze hybride modaliteit in de interventiekamer.

Een SPECT-scan is nodig om de verdeling van ^{99m}Tc-MAA in de lever te bekijken en om te controleren of er zich geen activiteit buiten de lever bevindt. Een klinische SPECT-scan duurt echter 30 minuten; dit is te lang voor tijdens een interventie. In **Hoofdstuk 5** werd onderzocht of een snelle SPECT-scan haalbaar is en of de nauwkeurigheid verbeterd kan worden met een protocol met niet-uniforme acquisitietijden. SPECT-beelden van de lever na toediening van 150 MBq ^{99m}Tc-MAA werden gesimuleerd van verschillende fantomen, acquisitietijden en acquisitieprotocollen. Uit de simulaties bleek dat er geen groot verschil was in de beeldkwaliteit en dosimetrie tussen beelden van niet-uniforme tijd protocollen en uniforme tijd protocollen. De contrast-ruisverhouding werd lager bij kortere acquisitietijden, maar kwantificatie van activiteit, tumor/niet-tumor ratio

en LSF-schattingen waren constant bij alle gesimuleerde acquisitietijden. De resultaten van het gemeten fantoom kwamen overeen met de simulaties. Er werd geconcludeerd dat zowel met uniforme als niet-uniforme protocollen voldoende beeldkwaliteit binnen 10 minuten kan worden verkregen om dosimetrie voor radio-embolisatie te doen. Een snelle SPECT-scan van de lever in de interventiekamer is dus haalbaar.

Radio-embolisatie wordt steeds vaker gebruikt als middel om resectie mogelijk te maken (radiatie lobectomy). Hierbij wordt controle van de tumor gecombineerd met het induceren van volumetoename in het contralaterale deel van de lever om zo resectie mogelijk te maken. In **Hoofdstuk 6** werd de potentiële toegevoegde waarde van het meten van regionale leverfunctie (hepatobiliaire scintigrafie (HBS)) voor en na radio-embolisatie voor de beoordeling van de toekomstige resterende lever onderzocht. Dertien patiënten die een HBS voor en na radioembolisatie met ^{90}Y glas microsferen hebben ondergaan, werden geïncludeerd. Functie en volume van de gehele lever, alsmede van het behandelde en niet-behandelde deel apart, werden bepaald op de HBS. De geabsorbeerde dosis werd op de ^{90}Y PET-CT bepaald. Radio-embolisatie zorgde voor een afname in functie en volume in het behandelde deel, terwijl functie en volume toenamen in het niet-behandelde deel. Er werden grote individuele verschillen gevonden tussen functie- en volumeveranderingen. Dit impliceert dat HBS een toegevoegde waarde heeft in het management van patiënten die behandeld worden met radiatie lobectomy.

Conclusies

- Met parallel hole collimatoren kunnen beelden met minder ruis en een betere detecteerbaarheid worden verkregen dan met pinhole collimatoren in het eerste ontwerp van onze hybride modaliteit.
- Een dual layer detector, bestaande uit een platte röntgendetector met direct daarachter een gamma camera met gefocusseerde collimator kan worden gebruikt om simultaan intrinsiek geregistreerde hybride beelden op te nemen.
- LSF kan binnen enkele seconden met een constante kleine fout worden geschat met het eerste ontwerp van een hybride modaliteit in de interventiekamer.
- Zowel met uniforme als niet-uniforme protocollen kan voldoende beeldkwaliteit binnen 10 minuten worden verkregen voor radio-embolisatie dosimetrie.
- Radio-embolisatie leidt tot regionale veranderingen in leverfunctie, maar functie- en volumeveranderingen laten grote individuele verschillen zien. Dit impliceert een toegevoegde waarde van HBS in het management van patiënten die behandeld worden met radiatie lobectomy.

List of publications

Journal papers

S. van der Velden*, B. Kunnen*, W.J.C. Koppert, J.H.L Steenbergen, M.M.A. Dietze, C. Beijst, M.A. Viergever, M.G.E.H. Lam, H.W.A.M. de Jong, "A dual layer detector for simultaneous fluoroscopic and nuclear imaging – Proof of concept", Radiology, 2019 (* authors contributed equally)

S. van der Velden, M.M.A. Dietze, M.A. Viergever, H.W.A.M. de Jong, "Fast technetium-99m liver SPECT for evaluation of the pre-treatment procedure for radioembolisation dosimetry", Medical Physics, 2019, nr. 1, vol. 46, pp. 345-355

M.M.A. Dietze, **S. van der Velden**, M.G.E.H. Lam, M.A. Viergever, H.W.A.M. de Jong, "Fast quantitative reconstruction with focussing collimators for liver SPECT", EJNMMI Physics, 2018, nr. 1, vol. 5, pp. 28-43

B. Kunnen, **S. van der Velden**, R. Bastiaannet, M.G.E.H. Lam, M.A. Viergever, H.W.A.M. de Jong, "Radioembolization lung shunt estimation based on a ^{90}Y pre-treatment procedure: a phantom study", Medical Physics, 2018, nr. 10, vol. 45, pp. 4744-4753

W.J.C. Koppert, **S. van der Velden**, J.H.L. Steenbergen, H.W.A.M. de Jong, "Impact of intense x-ray pulses on a NaI(Tl)-based gamma camera", Physics in Medicine & Biology, 2018, nr. 6, vol. 63, pp. 065006

S. van der Velden, R. Bastiaannet, A.J.A.T. Braat, M.G.E.H. Lam, M.A. Viergever, H.W.A.M. de Jong, "Estimation of lung shunt fraction from simultaneous fluoroscopic and nuclear images", Physics in Medicine & Biology, 2017, nr. 21, vol. 62, pp. 8210-8225

S. van der Velden, C. Beijst, M.A. Viergever, H.W.A.M. de Jong, "Simultaneous fluoroscopic and nuclear imaging: Impact of collimator choice on nuclear image quality", Medical Physics, 2017, nr. 1, vol. 44, pp. 249-261

C. Beijst, M. Elschot, **S. van der Velden**, H.W.A.M. de Jong, "Multimodality calibration for simultaneous fluoroscopic and nuclear imaging", EJNMMI Physics, 2016, nr. 1, vol. 3, pp. 20-34

S. van der Velden, C. Mönninghoff, I. Wanke, M. Jokisch, C. Weimar, R. Lopes Simoes, A.M. van Cappellen van Walsum, C. Slump, "Automatic determination of white matter hyperintensity properties in relation to the development of Alzheimer's disease", Computer-Aided Diagnosis (International Society for Optics and Photonics), 2016, vol. 9785, pp. 97852D

Submitted for publication

S. van der Velden, M.N.G.J.A. Braat, T.A. Labeur, M.V. Scholten, O.M. van Delden, R.J. Bennink, H.W.A.M. de Jong, M.G.E.H. Lam, "A pilot study on hepatobiliary scintigraphy to monitor regional liver function in yttrium-90 radioembolization", *Submitted for publication*

Dankwoord

Het dankwoord, het deel van ieder proefschrift dat waarschijnlijk het meest gelezen wordt, maar waar het minste tijd aan wordt besteed. En dat is eigenlijk niet terecht, want zonder de steun en het vertrouwen van velen was dit proefschrift er niet geweest. Ook al is de rest van mijn proefschrift zeker de moeite waard om te lezen, ik kan begrijpen dat voor niet-ingewijden in het vakgebied het dankwoord wat lichter verteerbare kost is. Om een idee te krijgen van wie er zoal heeft bijgedragen aan dit proefschrift, zou ik je daarom willen aanraden om het dankwoord in zijn geheel te lezen en niet alleen op zoek te gaan naar je eigen naam. Tenzij je natuurlijk hiervoor het gehele proefschrift hebt gelezen, dan is het toegestaan om het dankwoord te scannen en alleen het stukje over jezelf te lezen. Voor de rest, veel leesplezier!

Allereerst wil ik mijn promotoren prof. dr. ir. Hugo de Jong en prof. dr. ir. Max Viergever bedanken. Hugo, ik heb je wetenschappelijke input altijd zeer gewaardeerd. Jouw out-of-the-boxdenken levert soms verrassende inzichten op. Bedankt voor de leuke Ardennen-weekendjes en de BBQs in Zeist. Max, ondanks je drukke agenda heb ik nooit het gevoel gehad dat je geen tijd had om mijn papers te lezen. Jouw commentaar was zeer verhelderend.

Ook wil ik mijn waardering uitspreken voor de beoordelingscommissie. Bedankt prof. dr. ir. J.J.W. Lagendijk, prof. dr. H.M. Verkooijen, prof. dr. W.P.T.M. Mali, prof. dr. R.J. Bennink en dr. H. Wieczorek.

Ik begon mijn promotie in een mannenbolwerk, met Casper, Edwin en Jaap op de kamer en Robert verderop in de gang. Jullie zorgden ervoor dat ik snel kon beginnen en ik kon met al mijn vragen bij jullie terecht. Casper, jij was mijn lichtend voorbeeld. Jouw pragmatische aanpak was heerlijk: usb-kabeltje in het systeemplafond, spuitje technetium eraan en meten maar. Robert, jij hebt me enorm geholpen om op gang te komen, zowel inhoudelijk als met alle administratieve rompslomp. Edwin, jouw rust straalde af op de hele kamer. Jaap, jouw creativiteit en kennis zorgden voor interessante en verhelderende discussies. Later in mijn promotie kwamen Wilco, Leo, Remco, Britt, Martijn, Fasco, Woutjan, Pascal en Frank de groep versterken. Wilco, ook al hadden we in het begin wat moeite om elkaar te begrijpen, al snel bleek dat je een aanwinst was voor de groep. Jouw oog voor detail én voor business-cases staat garant voor enerverende gesprekken bij de koffieautomaat. Leo, wanneer gaan we weer boodschappen doen met de panda? Remco, sorry voor alle keren dat ik je liet schrikken. Het is gewoon te gemakkelijk en leuk om het niet te doen. Britt, mijn medevrouw in de groep! Ik heb enorm genoten van onze samenwerking. Het was een eer om de administratie van het vullen van je fantomen te mogen doen. Martijn, zo hard als je rent, ga je ook door je promotie heen. Fasco, wat had ik zonder jouw beheer van de theevoorraad gemoeten? Woutjan, boven is het véél gezelliger dan beneden. Pascal en Frank, jullie moeten het nu waar gaan maken. Die c-boog staat er over een jaar, gemeten vanaf het moment dat je dit leest.

Beste klinisch fysici (i.o.), Arnold, Rob, Bastiaan en Bas, bedankt voor alle gezellige lunches, stukjes taart en natuurlijk ook de nodige hulp hier en daar. Arnold, jij bent niet alleen thuis, maar ook hier de pappa van de groep. Rob, naast een gedegen kennis van de werking én de bugs van UMCS, heb jij ruime ervaring met het intekenen van wc's. Mocht ik ooit twijfelen over de beste plaats voor mijn wc, dan weet ik je te vinden. Bastiaan, jouw aangeboren Twentse nuchterheid en aangeleerde Brabantse gezelligheid is een gouden combinatie. Naast onze voorliefde voor lijstjes, delen wij ook een voorliefde voor afritsbroeken. Bas, jij zorgt ervoor dat de hoeveelheid zuidelijk

bloed in de groep op peil blijft.

Ik wil graag alle laboranten van de afdeling radiologie en nucleaire geneeskunde bedanken. Laboranten van de nucleaire geneeskunde, jullie stonden altijd klaar om mij te helpen met het scannen van fantomen. Ook hoefde ik maar binnen te komen, of ik kreeg al een cobaltpennetje mee. Zonder jullie ondersteuning was het zeker niet gelukt om dit proefschrift te schrijven. Ook bedankt voor alle lekkere stukjes taart die jullie in de koffiekamer lieten staan. Dat was altijd weer een heerlijk toetje na de lunch. Laboranten van de radiologie, bedankt dat we keer op keer de DRX mochten lenen. Na een tijdje was binnen komen lopen genoeg om "ja, neem maar mee" te horen. Ook wil ik het technisch kluster, en in het bijzonder Kees, bedanken voor alle technische hulp en het werkend houden van mijn computer. Kees, je mag hem nu eindelijk afvoeren en vervangen voor een nieuwe.

Heren van het lab, Gerard, Remmert en John, bedankt. Gerard en Remmert, ik heb veel geleerd van jullie over chemicaliën en het omgaan met radioactiviteit. Bedankt voor alle interessante discussies over de toekomst van het RNA lab en radionuclidentherapie. John, bedankt voor het klaarmaken van de talloze spuitjes en epjes met technetium. Fijn dat je, ondanks de vaak laatste moment bestellingen, altijd tijd vrij maakte om wat technetium voor me op te trekken.

Manon en Marnix, dank je wel voor de fijne samenwerking tijdens de HIDA-studie. Manon, jouw hulp bij het intekenen van alle levers en tumoren was van onmisbare waarde voor het project. Marnix, jij had altijd tijd om mijn resultaten te bediscusseren en van klinische context te voorzien.

Zeer gewaardeerde-ISI collega's, ik weet dat jullie nu allemaal in deze paragraaf gaan kijken of je persoonlijk wordt genoemd, maar ik geloof er niets van dat jullie allemaal mijn proefschrift van voor naar achter hebben doorgelezen. Ik bedank jullie allemaal voor de leuke Ardennen-weekenden, Sinterklaasvieringen en andere feestjes en partijen. Jelmer, ik zal aan je denken als ik mijn adventurepants weer aan heb. Bas, jij blijft mijn neefje. Hui Shan en Mike, we zijn samen begonnen aan het avontuur van promoveren en dat schept een band. Het was altijd gezellig op jullie kamer, met heerlijke koekjes! Mariëlle, jij zult nu toch als eerste docent van het jaar worden. Julia, met jou samen boulderen bracht de hoognodige ontspanning. Onder jouw aanmoedigingen klim ik naar ongekende hoogtes.

Dames van het scretariaat, Marjan, Jacqueline en Renée, bedankt voor alle ondersteuning tijdens mijn promotie.

Beste (oud-)SHOTers, bedankt voor de leuke reisjes, concerten en andere (muzikale) activiteiten. Mathijs, Marinke en Jord, ik ben blij dat we elkaar ook na onze gezamelijke SHOT-tijd zijn blijven zien. Mathijs en Marinke, bedankt voor de gezellige middagen en avonden. Ik waardeer het dat ik altijd mijn verhaal bij jullie kwijt kan, in leuke en minder leuke tijden. Jord, jouw gastvrijheid en vriendelijkheid maken je tot een zeer gewaardeerde vriend. Je bent altijd welkom voor een kopje thee als je weer in Utrecht bent.

Koen, Thomas, Vasco, Bas, Jethro en Sarah, bedankt voor alle leuke spelletjesmiddagen en kerstdiners. Koen (bio-Koen voor mijn ouders), jouw gedrevenheid voor een betere wereld verdient de hoofdprijs. Als je nou de volgende keer bij een spelletje íetsjes minder lang nadenkt, ben je de perfecte man. Thomas, we waren op de middelbare school niet de beste vrienden, maar ik ben blij dat ik mijn mening heb bijgesteld. Jij staat altijd voor iedereen klaar. Vasco, ondanks dat ik nooit op je verjaardag kan komen, ben ik blij dat we regelmatig contact blijven houden. Bas, jij maakt ondanks je succesvolle carrière toch altijd weer tijd vrij om je oude middelbare

schoolvrienden met een bezoekje te vereren. Jouw droge humor zorgt ervoor dat we altijd wat te lachen hebben. Jethro, bedankt voor de heerlijke (kerst)diners. Sarah, jouw enthousiasme toen ik je vroeg mijn paranimf te zijn, was onvergetelijk. Ook al spreken we elkaar misschien niet zo vaak als we zouden willen, het voelt altijd weer als vanouds.

Timen, Corine en Marjolein, de weekendjes weg, escaperooms en geocaches waren geweldig. Ik ben blij dat we na al die jaren toch nog aan geoman ontsnapt zijn! Timen, bedankt dat je mij door Giethoorn en omstreken hebt gekanood (dat spel je schijnbaar echt zo). Zonder jou had ik nog steeds ergens in een sloot naast de kanoverhuur vastgezeten. Marjolein, zonder jouw survivalskills hadden we zeker honger geleden op onze hikes. Bedankt voor het beheren van de proviand. Corine, onze eerste indruk van elkaar was niet de beste. Gelukkig kwam dat snel goed en werd je mijn beste vriendin. Onze vakantie naar IJsland was geweldig, ook al hebben we geen papagaaiduiker gezien, was ons avondeten niet erg hoogstaand (die doperwtjes waren best te doen) en waren we te gierig om uit eten te gaan op de laatste avond (de friettent is ook uit eten, toch?). Jij staat altijd voor mij klaar en ik ben blij dat je mijn paranimf bent.

Lieve familie, jullie hebben mij altijd gesteund in alles wat ik doe. Marleen, jouw grote-zussen-wijzeraad helpt me altijd om de juiste beslissing te nemen. Nicole, bedankt voor de ontspanning tijdens onze bezoekjes aan de handwerkbeurs, mét poffertjes achteraf. Selma en Dorith, jullie weten me op elk moment op te vrolijken. Lieve oma, ik ben je ontzettend dankbaar voor alle leuke logeerpartijen vroeger en de leuke, openhartige telefoongesprekken. Pappa, ik ben nu eindelijk 'afgestudeerd' en begin straks aan mijn eerste échte baan. Mamma, precies begrijpen wat ik doe (iets met straling) blijkt niet nodig om mijn steun en toeverlaat te zijn. Ik kan altijd bij jou terecht en je staat altijd voor me klaar.

Tot slot, lieve Japser, met jou aan mijn zijde kan ik de wereld aan. Jouw rust helpt mij om onverwachte gebeurtenissen het hoofd te bieden. Jij weet soms eerder dan ik dat ik ergens mee zit. Ik ben blij dat je me de vrijheid geeft die ik soms zo hard nodig heb en ik kijk uit naar een toekomst samen met jou.

Curriculum Vitae

Sandra van der Velden was born on the 11th of June 1989 in Nuenen, Gerwen en Nederwetten. She went to secondary school at the Lorentz Casimir Lyceum in Eindhoven, where she graduated in 2007. That summer, she went for six months to Thoeng (Chiang Rai, Thailand) with American Field Services (AFS) to do voluntary work in the local hospital. In 2008, she started her bachelor studies in Technical Medicine at the University of Twente in Enschede. She passed her bachelor exam (cum laude) in 2011 and continued with a master degree in Biomedical Engineering (track clinical physics) at the same university. In 2013, she went to Western University in London (Ontario, Canada) for her internship at the Robarts Research Institute. The research for her master thesis was conducted at the Robotics and Mechatronics group at the University of Twente. In 2014, she obtained her Master's degree (cum laude) from the University of Twente. She then started working as a PhD student at the University Medical Center Utrecht. This results of this work are described in this thesis.

In january 2019, she started working as a clinical scientist at the Antoni van Leeuwenhoek hospital in the EPID dosimetry group of the radiotherapy department.